

AD-A285 361



Dist: A

(B)

## INTATION PAGE

Form Approved

OMB No. 0704-0188

Noted to average 1 hour per response, including the time for reviewing instructions, searching existing data sources, reviewing the collection of information, Send comments regarding this burden estimate or any other aspect of this burden, to Washington Headquarters Services, Directorate for Information Operations and Reports, (215 Jefferson Avenue, Washington, DC 20503-4302, and to the Office of Management and Budget, Paperwork Reduction Project (0704-0188), Washington, DC 20503.

1. AGENCY USE ONLY (Leave blank)		2. REPORT DATE 20 September 1994		3. REPORT TYPE AND DATES COVERED Final: 1 Aug 92 to 31 Jul 94	
4. TITLE AND SUBTITLE Physcial-Chemical Studies on Rodlike Polymer Compositons				5. FUNDING NUMBERS Grant No. F49620-92-J-0281 62102F 2419-00	
6. AUTHOR(S) G. C. Berry					
7. PERFORMING ORGANIZATION NAME(S) AND ADDRESS(ES) Carnegie Mellon University Office of Research Contracts 5000 Forbes Avenue Pittsburgh, PA 15213-3890					
8. PERFORMING ORGANIZATION REPORT NUMBER  AFOSR-TR- 94 0634				9. SPONSORING/MONITORING AGENCY NAME(S) AND ADDRESS(ES) AFOSR/NL 110 Duncan Avenue Suite B115 Bolling AFB DC 20322-001	
10. SPONSORING/MONITORING AGENCY REPORT NUMBER				11. SUPPLEMENTARY NOTES Dr. Lee 105P 94-31830 	
12a. DISTRIBUTION/AVAILABILITY STATEMENT  Approved for public release; distribution unlimited.				12b. DISTRIBUTION CODE  A	
13. ABSTRACT (Maximum 200 words) Third harmonic generation (THG) is used to study the third-order nonlinear optical properties of nematic and isotropic solutions of poly(phenylene benzobisthiazole), PBZT, and related small molecule model compounds. Maker fringe patterns (MFP) for isotropic preparations are analyzed in terms of postulated surface layers comprising regions in which the rodlike chains tend to have their axes parallel to the plane of the surface, creating a negatively birefringent uniaxial nematic layer. The THG with the nematic solution exhibits intensity with polarization components unexpected for uniaxial nematic symmetry, along with other unexpected features in the MFP. This behavior is attributed to the effects of surface layers, postulated to exhibit biaxial nematic symmetry, in which the uniaxial nematic symmetry is broken in regions on the scale of a wavelength. Features of the texture of the nematic phase of PBZT solutions are discussed. The nature of twist-loop defects in the texture is described, along with certain defects in the form of an ellipsoid of revolution, postulated to result from a molecular weight fractionation in the heterodisperse polymer. Light scattering studies on dilute solutions of a poly(n-dodecyl thiophene) are given to elucidate supramolecular structure that leads to a thermochromic effect. The supramolecular structure may play a role in the molecular organization in the solid state, with influence on electronic and nonlinear optical behavior.					
14. SUBJECT TERMS nonlinear optics, third harmonic generation, nematic, rodlike poly(1,4-phenylene-2,6-benzobisthiazole), poly(n-dodecyl thiophene)				15. NUMBER OF PAGES 63	
16. PRICE CODE					
17. SECURITY CLASSIFICATION OF REPORT u	18. SECURITY CLASSIFICATION OF THIS PAGE u	19. SECURITY CLASSIFICATION OF ABSTRACT u	20. LIMITATION OF ABSTRACT u		

# TABLE OF CONTENTS

Abstract	i
Table Captions	ii
Figure Captions	ii
A. INTRODUCTION	1
B. PERSONNEL	1
C. PUBLICATIONS	2
D. TECHNICAL REPORT	3
1. The Effects of Surface Layers on the Nonlinear Optical Properties of Solutions of a Nematogenic Polymer	3
1.1 Introduction	3
1.2 Experimental	3
1.2.1 Materials	3
1.2.2 Nonlinear Optical Measurements	4
1.3 Results	6
1.3.1 Linear Optical Behavior	6
1.3.2 NLO Studies on Isotropic Solutions of PBZT and Model Compounds	7
1.3.3 NLO Studies on Monodomain Nematic Solutions of PBZT	8
1.4 Data Analysis	9
1.4.1 Isotropic Solutions of PBZT and Model Compounds	9
1.4.2 Monodomain Nematic Solutions of PBZT	10
1.5 Discussion	11
1.5.1 Isotropic Solution of PBZT and Model Compounds	11
1.5.2 Monodomain Nematic Solutions of PBZT	12
1.6 Conclusion	15
2. Studies on the Texture of Nematic Solutions of a Rodlike Polymer	18
2.1 Introduction	18
2.2 Order in Monodomains of PBZT Nematic Solutions	18
2.3 Point Defects in Otherwise Aligned Nematic Solutions of PBZT	19
2.4 The Defect Structure During the Evolution of a Monodomain	20
2.5 Conclusions	24
3. Association of a Poly(n-alkyl thiophene) in Dilute Solution	25
3.1 Introduction	25
3.2 Experimental	25
3.2.1 Methods	25
3.2.2 Data Analysis	26
3.3 Results	28
3.4 Discussion	30
3.5 Conclusion	31
4. References	32
Figures	

DTR QUALITY INSPECTED 2

Distribution/	
Availability Codes	
Dist	Avail and/or Special
A-1	

## TABLE CAPTIONS

Table 1 Typical Values of the Coherence Length Nematic Solutions of PBZT

Table 2 Third-Order Susceptibilities for PBZT and Model Compounds

## FIGURE CAPTIONS

Figure 1. Structural formulae for molecules used in NLO measurements.

Figure 2. The extraordinary ( $n_E$ ) and ordinary ( $n_O$ ) refractive indices versus wavelength for a nematic solution of PBZT ( $\phi = 0.055$ ). The short and long dashed vertical lines show the fundamental and the THG wavelengths for fundamental wavelengths of 1.907 and 1.542  $\mu\text{m}$ , respectively.

Figure 3. The reduced coherence length  $L_c(\vartheta)/L_c(0)$  versus the rotation angle  $\vartheta$  for a nematic solution of PBZT in MSA ( $\phi = 0.055$ ; see Table 1). Curves 1 and 3 give  $[L_c(\vartheta)/L_c(0)]_{\text{III;h}}$  and  $[L_c(\vartheta)/L_c(0)]_{\text{VH;h}}$ , respectively, and curve 2 represents  $[L_c(\vartheta)/L_c(0)]_{\text{IV;v}}$  for the remainder of the geometrical arrangements discussed in the text (e.g.,  $[L_c(\vartheta)/L_c(0)]_{\text{HV;v}}$ , etc.); small distinctions among these for larger  $\vartheta$  are not shown in the interests of clarity.

Figure 4. Upper: Absorbance versus wavelength for methane sulfonic acid solutions of PBZT ( $\phi = 0.021$ ) in the near infra-red spectral region, for 350  $\mu\text{m}$  pathlength; the arrows show the wavelengths  $\lambda_\omega$  for fundamental intensities discussed in the text.

Lower: Absorbance versus wavelength for methane sulfonic acid solutions of PBZT ( $\phi = 0.021$ ), 1; BZT-36 ( $\phi = 0.0054$ ), 2; and BZT-18 ( $\phi = 0.004$ ), 3; and the normalized fluorescence emission  $I(\lambda)/I_{\text{max}}$  versus wavelength for methane sulfonic acid solutions of PBZT ( $\phi = 0.021$ ), the circles give the data, with a smooth curve to aid the reader. All for 350  $\mu\text{m}$  pathlength; the arrows show the wavelengths  $\lambda_{3\omega}$  for THG intensities discussed in the text.

Figure 5. The third-harmonic response for an isotropic solution of PBZT ( $\phi = 0.021$ ):  $R_{\text{VV}}^{(3\omega)}(0, L)$  versus the translation in a wedge-shaped cell (0.95 deg) for  $\lambda_\omega$  equal to 1.542  $\mu\text{m}$ , (a), and 1.907  $\mu\text{m}$ , (b).

Figure 6. The third-harmonic response for an isotropic solution of PBZT ( $\phi = 0.021$ ):  $R_{\text{VV}}^{(3\omega)}(\vartheta, L)$  versus  $\vartheta$  in a rotating-slab cell ( $L = 350 \mu\text{m}$ ) for  $\lambda_\omega$  equal to 1.542  $\mu\text{m}$ , (a), and 1.907  $\mu\text{m}$ , (b). The solid lines were calculated as discussed in the text, using arbitrary  $L/L_c(0)$  to obtain a fit.

- Figure 7 The third-harmonic response  $R_{VV}^{(3\omega)}(0,L)$  versus the translation in a wedge-shaped cell (0.5 deg) for solutions of (a) BZT-18 ( $\phi = 0.004$ ) and (b) BZT-36 ( $\phi = 0.0054$ ,  $\lambda_\omega = 1.542 \mu\text{m}$ ).
- Figure 8. The third-harmonic response  $R_{\rho\mu\nu}^{(3\omega)}(\vartheta,L)$  for a nematic solution of PBZT in a rotating-slab cell for the indicated orientations of the polarizations of the fundamental ( $\mu$ ) and THG waves ( $\rho$ ), and the director ( $\nu$ ) ( $\phi = 0.055$ ,  $L = 350 \mu\text{m}$ ,  $\lambda_\omega = 1.542 \mu\text{m}$ ).
- Figure 9. Relative third-harmonic generation response  $R_{\Omega\nu;\nu}^{(3\omega)}(\vartheta, L)$  for a nematic solution of PBZT in methane sulfonic acid as a function of the angle  $\Omega$  between the director and the analyzer, for several values of  $\vartheta$  ( $\phi = 0.055$ ,  $L = 350 \mu\text{m}$ ,  $\lambda_\omega = 1.542 \mu\text{m}$ ).
- Figure 10. Relative third-harmonic generation responses  $R_{U\Theta;\nu}^{(3\omega)}(0,L)$  and  $R_{\Theta\Theta;\nu}^{(3\omega)}(0,L)$  for a nematic solution of PBZT in methane sulfonic acid as a function of the angle  $\Theta$  between the polarization of the incident wave and the vertical direction ( $\phi = 0.055$ ,  $L = 350 \mu\text{m}$ ,  $\lambda_\omega = 1.542 \mu\text{m}$ ). The upper and lower panels give  $R_{U\Theta;\nu}^{(3\omega)}(0,L)$  and  $R_{\Theta\Theta;\nu}^{(3\omega)}(0,L)$ , respectively, with no analyzer  $R_{U\Theta;\nu}^{(3\omega)}(0,L)$ , and with the analyzer parallel to the polarization of the incident waves for  $R_{\Theta\Theta;\nu}^{(3\omega)}(0,L)$ .
- Figure 11 Comparison of observed MFP with calculations for an isotropic solution of PBZT (see Fig. 6 caption) using Eqn. 8 for a trilayer system and surface layers of  $36 \mu\text{m}$  ( $L = 350 \mu\text{m}$ ), see the text, for  $\lambda_\omega$  equal to  $1.542 \mu\text{m}$ , (a), and  $1.907 \mu\text{m}$ , (b).
- Figure 12 Comparison of observed MFP with calculations for a nematic solution of PBZT (see Fig. 9 caption) using Eqn. 8 for a trilayer system and surface layers of  $36 \mu\text{m}$ , see the text ( $\lambda_\omega = 1.542 \mu\text{m}$ ,  $L = 350 \mu\text{m}$ ): upper,  $R_{VV;\nu}^{(3\omega)}(\vartheta,L)$ ; middle,  $R_{HV;\nu}^{(3\omega)}(\vartheta,L)$ ; lower,  $R_{VV;h}^{(3\omega)}(\vartheta,L)$ .
- Figure 13 Optical effects observed on changing the temperature of a monodomain nematic solution of a rodlike polymer (PBZT in methane sulfonic acid;  $\phi = 0.049$ ,  $L_w = 140 \text{ nm}$ ).  
Upper: The transmission between crossed and parallel polars ( $\lambda = 632.8 \text{ nm}$ ).  
Lower: The ratio of the fluorescence emission intensities  $I_{\parallel}$  and  $I_{\perp}$ , for light polarized parallel and perpendicular to the director, respectively (Incident light absorbed within  $\approx 1 \mu\text{m}$ ). The open and filled circles give data for increasing and decreasing temperature, respectively.
- Figure 14 Schematic diagram of a bipolar defect structure observed during heating a nematic solution of PBZT below the clearing temperature.
- Figure 15 Fluorescence emission during annealing of a sample to form a monodomain after extrusion into a tube with a rectangular channel ( $400\mu\text{m} \times 8\text{mm}$ );  $\phi = 0.043$ ,  $L_w = 120 \text{ nm}$ . The ratio of the fluorescence emission intensities  $I_{\parallel}$  and  $I_{\perp}$ , for light polarized parallel and perpendicular to the director, respectively (Incident light absorbed within  $\approx 1 \mu\text{m}$ ). The squares and circles give data for filling rates of  $0.032$  and  $2.4 \text{ mm}^3/\text{s}$ , respectively.

- Figure 16** Optical effects observed on changing the temperature of a monodomain nematic solution of a rodlike polymer (PBZT in methane sulfonic acid;  $\phi = 0.033$ ,  $L_w = 155$  nm).  
Squares: The temperature dependence of the ratio  $I_{\parallel}/I_{\perp}$  of the fluorescence emission intensities  $I_{\parallel}$  and  $I_{\perp}$  for light polarized parallel and perpendicular to the director, respectively (Incident light absorbed within  $\approx 1$   $\mu$ m).  
Circles: The temperature dependence of the invariant of the fluorescence emission intensities.
- Figure 17** Schematic diagrams of the appearance of twist-loop defects in orthoscopic microscopy. The nematic director is horizontal in all cases, and the orientation of the polarizer P for the incident light is indicated by the arrows and/or the angles; the orientation of the analyzer A of the transmitted light is parallel or perpendicular to P in the upper and lower panels, respectively. The black and shaded loops appear dark and bright, respectively, with the image for P at  $\pi/4$  to the director being a loop alternating between dark and bright regions.
- Figure 18** Example of the relaxation of a complex loop defect(s). Schematic representations of photomicrographs prepared between crossed polarizer and analyzer on the left, and schematic diagrams of the loop(s) on the right; cell thickness 300  $\mu$ m,  $\phi = 0.063$ ,  $L_w = 135$  nm.  
a. The upper portion of a small loop, and a portion of a large loop that crosses over itself four times in the field of view (the loop continues at the upper left and lower right); a third loop appears to be in contact with the large loop (47.5 hr after filling).  
b. A remnant of the small loop, a small loop that has separated from the large loop, and the evolution of the large loop (71.5 hr after filling).  
c. Continued evolution of the large loop, with the two smaller loops having vanished (122.5 hr after filling).  
d. Continued evolution of the large loop (243.5 hr after filling).
- Figure 19** The average diameter of loops during collapse as a function of the time  $t_0 - t$  measured from the time  $t_0$  that the loop disappears. The data are for three samples:  $\phi = 0.050$ ,  $L_w = 155$  nm, open symbols (different loops designated by different symbols);  $\phi = 0.058$ ,  $L_w = 155$  nm, filled circles;  $\phi = 0.063$ ,  $L_w = 135$  nm, filled squares. The lines have unit slope.
- Figure 20** The effect of temperature on the absorbance of a dilute solution of poly(*n*-dodecylthiophene) in chloroform;  $c = 3.0$  g/L. The temperature is indicated on the figure; the cell was 0.2 cm thick.
- Figure 21** Static light scattering on dilute solutions of poly(*n*-dodecylthiophene) in chloroform; upper and lower panels are for the depolarized (Hv) and polarized scattering (Vv), respectively. The concentrations are indicated (g/L); the unfilled and filled symbols are for histories A and B, respectively.
- Figure 22** The first cumulant from dynamic light scattering on dilute solutions of poly(*n*-dodecylthiophene) in chloroform.  
Upper: Polarized (Vv) scattering for a solution with  $c = 1.97$  g/L, history E;

Lower: Depolarized (Hv) scattering for a solution with  $c = 3.0$  g/L, history A.

- Figure 23 Static polarized (Vv) light scattering on dilute solutions of poly(*n*-dodecylthiophene) in chloroform. The concentrations are indicated (g/L); the unfilled and filled symbols are for histories A and C, respectively, and the shaded symbols are for history E.
- Figure 24 Static polarized (Vv) light scattering on dilute solutions of poly(*n*-dodecylthiophene) in chloroform;  $c = 3.0$  g/L. The concentrations are indicated (g/L); the unfilled circles and squares are for histories C and D, respectively, with the times at  $T_{q2} = -16.5^\circ\text{C}$  indicated (min), and the shaded symbols are for history F.
- Figure 25 Static depolarized (Hv) light scattering on dilute solutions of poly(*n*-dodecylthiophene) in chloroform;  $c = 3.0$  g/L. The concentrations are indicated (g/L); the unfilled circles and squares are for histories C and D, respectively, with the times at  $T_{q2} = -16.5^\circ\text{C}$  indicated (min), and the shaded symbols are for history F.
- Figure 26 Bilogarithmic plots of the change of two parameters with time for a dilute solution of poly(*n*-dodecylthiophene) in chloroform for history D, with  $T_{q2} = -16.5^\circ\text{C}$ ;  $c = 3.0$  g/L.  
 Upper: A function of the transmission  $T(t)$  ( $\lambda = 647.5$  nm);  
 Lower: The depolarized scattering at  $45^\circ$  scattering angle.
- Figure 27 Bilogarithmic plots of the change of several parameters with time for a dilute solution of poly(*n*-dodecylthiophene) in chloroform for history D, with  $T_{q2} = -16.5^\circ\text{C}$ ;  $c = 3.0$  g/L.  
 Upper: The apparent radius of gyration, the filled and unfilled symbols are for the polarized (Vv) and depolarized (Hv) scattering, respectively;  
 Middle: The apparent molecular weight from the polarized (Vv) scattering;  
 Lower: The ratios  $(R_{G,V}^2)_{LS}/(M_V)_{LS} \approx R_{G,LS}^2/M_w$  from the polarized (Vv) scattering (unfilled), and  $[R_{H,V}(0,c)/c]^0/[R_{V,V}(0,c)]^0$  of the reduced intensities at zero scattering angle of the depolarized (Hv) and polarized (Vv) scattering.

## A. INTRODUCTION

The following is the Final Report on Project F49620-92-J-0281 for the period 1 August 1992 to 31 July 1994. The study comprises three sections. The first is on an analysis of the nonlinear optical, NLO, properties of a nematic polymer solution and certain related model compounds. The second is on the nature of director field distortions in a nematic solutions of the same polymer. The third is on the characterization of the supramolecular structure in a certain poly(alkyl thiophene). In the first study, the NLO properties are analyzed to reveal optically distinct surface layers in both isotropic and nematic solutions of the rodlike poly(1,4-phenylene-2,6-benzobisthiazole), PBZT. The NLO response in third harmonic generation of PBZT is compared with that for model compounds. In the second study, the director field in nematic solutions is studied in more detail, including the kinetics of spontaneous alignment driven by aligned surfacelayers. The third study was motivated by the observation of reversible thermochromism in poly(alkyl thiophenes) and their solutions, and seeks to characterize any supramolecular structure associated with that behavior, especially with regard to potential effects on electronic and optical properties of solution processed materials.

In the following, project personnel and research collaborators are identified in part B, a list of publications appearing in the report period is presented in part C, and the technical report comprises part D.

## B. PERSONNEL

In addition to partial support (1 mo. per year) for the Principal Investigator, support for two Ph.D. graduate students was received:

Ms Beibei Diao

Ms Shunqiong Yue

Both students are expected to complete the defense of their Ph.D. dissertation research by October 1994; both have arranged employment in industrial laboratories in the U.S.

Collaborations during the work included:

Dr. Gary D. Patterson, Carnegie Mellon University

Dr. Hedi Mattoussi, University of Florida

Dr. Mohan Srinivasarao, AT&T Bell Laboratories

Dr. Richard D. McCullough, Carnegie Mellon University

Mr. Bruce A. Reinhardt, Wright Laboratories

The collaborations with the first three named included discussions and the preparation of manuscripts under joint authorship, without financial support from this project. Samples used in this work were received from the final two named.

## C. PUBLICATIONS

Work under (partial) support from the Air Force Office of Scientific research indicated by •:

- 145. Refractive Indices Dispersion and Order of Lyotropic Liquid Crystal Polymers, H. Matoussi, M. Srinivassarao, P. G. Kaatz and G. C. Berry, *Macromolecules*, **25**, 2860 (1992).
- 146. Magnetic Field Induced Instability In An Aligned Nematic Solution of a Rodlike Polymer, M. Srinivassarao and G. C. Berry, *Mol. Cryst. Liq. Cryst.*, **223**, 99 (1992).
- 147. Birefringence and Dispersion of Uniaxial Media, H. Matoussi, M. Srinivassarao, P. G. Kaatz and G. C. Berry, *Mol. Cryst. Liq. Cryst.*, **223**, 69 (1992).
- 148. Anisotropic Third-Order Susceptibility of a Nematic Solution of a Rodlike Polymer (PBT), H. Matoussi and G. C. Berry, *Mol. Cryst. Liq. Cryst.*, **223**, 41 (1992).
- 149. Condensation and Commentary of "A Solution for the Initital-Decay-Rate Puzzle in Dynamic Light Scattering of Polymer Solutions" by Y. Shiwa, et al, G. C. Berry, *Chemtracts-Macromolecular Chem.* **3**, 237 (1992).
- 150. Rheological Properties of Blends of Rodlike Chains with Flexible or Semiflexible Chains, G. C. Berry, *Trends in Polymer Science*, **1**, 309 (1993).
- 151. Static and Dynamic Light Scattering on Aligned Solutions of a Rodlike Polymer, N. Desvignes, K. A. Suresh, G. C. Berry, *J. Appl. Polym. Sci.: Polym. Symp.*, **52**, 33-43 (1993).
- 152. Third-Order Susceptibilities of Nematic and Isotropic Solutions of a Rodlike Polymer (PBT), H. Matoussi and G. C. Berry, in *Proceed Second Pacific Polymer Conference*, Ed. Y. Imanishi, Springer-Valig, (1993).
- 153. Condensation and Commentary of "Roll-Cell Instabilities in Shearing Flows in Nematic Polymers" by R. G. Larson, et al, G. C. Berry, *Chemtracts-Macromolecular Chem.* **4**, 1 (1994).
- 154. Condensation and Commentary of "Shear Rheology and Shear-Induced Textures of a Thermotropic Copolyesteramide" by T. DeNève, P. Navard and M. Kléman, G. C. Berry, M. Srinivasarao, *Chemtracts-Macromolecular Chem.* **4**, 84 (1994).
- 155. Static and Dynamic Light Scattering on Moderately Concentrated Solutions: Isotropic Solutions of Flexible and Rodlike Chains and Nematic Solutions of Rodlike Chains, G. C. Berry, *Adv. Polymer Sci.* **114**, 233-290 (1994).
- 156. Studies on the Texture of Nematic Solutions of a Rodlike Polymer and the Distortion of the Director Field in External Fields, B. Diao, K. Matsuoka, G. C. Berry, in *Seminar Lectures in the 2nd International Discussion Meeting on Relaxations in Complex Systems*, Ed. by E. Riande, National Council of Scientific Research of Spain, (1994), p. 000.
- 157. Studies of the Director Field in Shear Flow for Nematic solutions of a Rodlike Polymer, K. Matsuoka, G. C. Berry, *Nihon Reorogiji Dakkaishi* (in Japanese), **22**, 0000 (1994).
- 158. Light Scattering Studies on Dilute Solutions of Semiflexible Polyelectrolytes, *Intl. J. Polym Analysis and Characterization*, submitted.
- 159. The Effects of Surface Layers on the Nonlinear Optical Properties of Solutions of a Nematogenic Polymer, H. Matoussi, G. C. Berry and G. D. Patterson, to be submitted.



## D. TECHNICAL REPORT

### 1. The Effects of Surface Layers on the Nonlinear Optical Properties of Solutions of a Nematogenic Polymer

#### 1.1 Introduction

Nonlinear optical (NLO) measurements of third harmonic generation (THG) will be reported for both isotropic and well-aligned (monodomain) nematic solutions of the rod-like poly(1,4-phenylene-2,6-benzobisthiazole), PBZT. Studies on the monodomain were undertaken to elucidate features of nonlinear optical susceptibility tensor  $\chi^{(3)}(-3\omega; \omega, \omega, \omega)$ . Although the THG Maker fringe patterns (MFP) observed for the isotropic solutions are found to be normal, the MFP obtained for the monodomain nematic solutions exhibit unexpected features (see below), and depend on the relative configuration of the nematic mean field direction (optic axis  $\mathbf{n}$ ) with respect to the polarization of the fundamental and third harmonic rays. Unexpectedly, it is found that THG on monodomain nematic solutions gives elliptically polarized light for incident radiation polarized along the optic axis of the uniaxial nematic solution. By contrast, linear propagation under the same conditions gave linearly polarized exit waves. These surprising results prompted studies in three directions:

- A more complete description of the THG from both isotropic and aligned nematic solutions of PBZT;
- Study of the THG from model compounds related to PBZT;
- A more complete characterization of the molecular alignment in aligned nematic solutions of PBZT.

In the first area, the THG signal has been determined for isotropic solutions in both wedge-shaped and parallel slab cells, and the THG of monodomain nematic solutions has been studied as a function of the angle  $\Omega$  between the director  $\hat{\mathbf{n}}$  and the polarization direction of the polarizer P, both without and with an analyzer A aligned parallel to P. In the naive expectation, for  $\Omega = 0$ , the THG would give the same signal  $I_{3\omega}$  with or without the analyzer for perpendicularly incident light for a solute with rodlike symmetry. In the second area, the THG has been obtained for certain model compounds of PBZT, for a comparison with the magnitude of  $\chi^{(3)}$  obtained with PBZT solutions. In the third area, optical studies have been extended to assess the alignment of the nematic solutions studied, including comparison of calculated MFP with the experimental data.

In the experimental section, we describe the materials used, the technique for the THG measurements, the method of analysis, and the measurements of the refractive indices relevant to the THG data analysis. The results are given in the next section, followed by a discussion of the data in comparison with data on either conventional nematic liquid crystals or polymeric thin films.

#### 1.2 Experimental

**1.2.1 Materials** The PBZT, molecular weight  $M_w = 34,000$ , was provided by SRI International as a solution in polyphosphoric acid (weight fraction  $\approx 0.05$  polymer). The material was diluted in methanesulfonic acid, MSA, precipitated in methanol and dried in vacuum for several hours. The resulting product was then dissolved in distilled MSA using procedures discussed elsewhere.<sup>1-3</sup> Solutions of PBZT become nematic when the

volume fraction of the solute  $\phi$  exceeds a critical value  $\phi_{NI}$ , where the concentration  $\phi_{NI}$  for the onset of the nematic liquid crystal phase depends on the chain length and the temperature<sup>4,5</sup>;  $\phi_{NI} = 0.03$  at room temperature for the PBZT used.<sup>1-3</sup> A monodomain of the nematic solutions was obtained using a procedure described elsewhere.<sup>1-3,6,7</sup> Extrusion into a rectangular channel comprising the optical cell results in a thin aligned nematic layer near the cell surfaces. Exposure of the freshly filled sample to an external magnetic field (5–7 T) for several hours produces a monodomain alignment. The monodomain is stable for an indefinite duration. All the measurements on the PBZT nematic monodomains were taken at room temperature.

The structures of two model compounds related to the PBZT repeat unit are shown in Fig. 1. These compounds were provided as dry powders through the courtesy of B. A. Reinhardt, Wright Laboratory, Wright-Patterson Air Force Base, OH. Compound BZT-18 has two  $-\text{O}-(\text{CH}_2)_9-\text{CH}_3$  groups (18 methylenes in total) on a central phenylene, whereas the BZT-36 has two such groups on each of two terminal phenyls (36 methylenes in total). These materials were also dissolved in MSA, but only very dilute solutions were used owing to strong absorption of light by the solutes at 514 nm wavelength (see below), e.g.,  $\phi = 0.004$  for BZT-18 and  $\phi = 0.0054$  for BZT-36. The dissolution was found to be slower for BZT-18 than for BZT-36; heating at about 100°C for 30 min was found to accelerate the dissolution and provided a homogeneous sample.

**1.2.2 Nonlinear Optical Measurements** Third harmonic generation measurements were made using an apparatus described elsewhere.<sup>6</sup> Briefly, a plane-polarized beam generated by a pulsed Nd:YAG laser (1064 nm wavelength operating in the TEM<sub>00</sub> mode) was either used directly or to pump a Raman shifter to obtain the Stokes components (1542 or 1907 nm wavelengths); dispersing prisms were used to select the desired wavelength from the Raman shifter. The incident beam was split into two beams, one directed to the sample and the other to a reference material. The beam incident on the sample was weakly focused using a 50 cm focal length lens, and the orientation of its plane of polarization was controlled using a Fresnel Rhomb. Band pass filters were placed after the sample and the reference to eliminate the fundamental radiation, and interference filters to select the harmonic frequency (here,  $3\omega$ ) were placed before the photomultiplier tubes used to determine the photon count of the output beams. Data were obtained as pulse outputs (10 and 5 Hz repetition rate for 1064 and 1542 nm, respectively), and the ratio of the output from the sample and reference photomultipliers was stored electronically for later use.

The sample cells were either plane parallel or wedge-shaped cells with fused silica glass walls, provided by Hellma Cells Inc. The cell walls were specified to  $\lambda/4$  surface flatness, and were transparent from near UV to near IR. The sample thickness  $L$  of 350  $\mu\text{m}$  for the flat cell provided by the manufacturer was verified by measurement of the absorbance of standardized solutions. For the wedge-shaped cell,  $L(l) = L_0 + l \tan \eta$  with translation  $l$  along the cell length, where the wedge angle  $\eta$  was either 0.5 or 0.95 degrees for the two cells used,  $L_0$  was 200  $\mu\text{m}$  (for  $l = 0$ ), and  $l$  could be varied from 0 to 3.5 cm. The use of wedge-shaped cell eliminates effects on the periodicity of the MFP from contributions to the THG from the cell walls.

The reduced intensity  $R_{\sigma\mu\nu}^{(3\omega)}(\vartheta, L)$  of a Maker Fringe Pattern (MFP) of a uniaxial optically anisotropic medium depends on the angle of incidence  $\vartheta$  and the cell thickness  $L$ , and the polarizations of the THG and fundamental waves and the orientation of the optic axis anisotropic medium, represented by the indices  $\sigma$ ,  $\mu$ , and  $\nu$ , respectively:

$$R_{\sigma\mu;v}^{(3\omega)}(\vartheta, L) = \frac{[I_{\sigma\mu;v}^{(3\omega)}(\vartheta, L)]_{\text{SAMP}}}{[I_{\sigma\mu;v}^{(3\omega)}(\vartheta_R, L)]_{\text{REFR}}} \quad (1)$$

where SAMP and REFR stand for the sample and reference, respectively;  $\vartheta_R$  is fixed ( $\vartheta_R \approx 0$ ),  $\vartheta$  is varied by rotation of a parallel slab (fixed  $L$ ), and  $L$  is varied by translation of a wedge-shaped sample (fixed  $\vartheta$ , essentially equal to zero).<sup>8,9</sup> In the following, the subscripts  $\sigma$  and  $\mu$  will be denoted V or H if the components of the polarizations of the relevant waves are vertical or horizontal in the laboratory frame, respectively, or U for the THG wave if no analyzer is used. The subscript  $v$  will be denoted v or h if the optical axis of the uniaxial sample is vertical or horizontal in the laboratory plane, respectively. Additional subscripts used in special cases are defined below. A flat plate of fused silica ( $L = 1.00$  mm) was used as the working reference, and either a flat plate ( $L = 3.00$  mm) or a wedge-shaped BK7 optical glass ( $L_0 = 2.00$  mm,  $\eta = 2$  degrees) was used as the standard to compute absolute values of the nonlinear susceptibility.

In general, the MFP exhibit damped oscillations symmetric about  $\vartheta = 0$  for the rotating parallel slab cell, and oscillations that may or may not have a decreasing amplitude with increasing  $L$  for a wedge-shaped cell. A general expression for  $R_{\sigma\mu;v}^{(3\omega)}(\vartheta, L)$  for a slab or a wedge-shaped, homogeneous NLO material is given by:<sup>8,9-11</sup>

$$R_{\sigma\mu;v}^{(3\omega)}(\vartheta, L) = K_R \left( \frac{[W_{\sigma\mu;v}(\vartheta, L)]_{\text{SAMP}}}{[W(\vartheta_R, L)]_{\text{REFR}}} \right)^2 \quad (2)$$

$$W(\vartheta, L) = \frac{|\chi_{\text{EFF}}^{(3)}|}{|n_{3\omega}^2 - n_\omega^2|} w(\vartheta, L) \quad (3)$$

where the effective (or average) component  $|\chi_{\text{EFF}}^{(3)}|$  of  $\chi^{(3)}(-3\omega; \omega, \omega, \omega)$ , depends on the polarization of the THG and fundamental waves and the orientation of the optically anisotropic material (see below),  $n_\omega$  and  $n_{3\omega}$  are the refractive indices at the incident and the THG frequencies, respectively, and  $K_R$  is the ratio between the incident beam directed to the sample and that directed to the reference. The function  $w(\vartheta, L)$  accounts for the interference effects between two waves, both propagating with frequency  $3\omega$ , but one with velocity  $c/n_{3\omega}$  and the other with velocity  $c/n_\omega$  giving rise to the MFP. For the case with weak (or no) absorption, characterized by absorbances  $\alpha_\omega$  and  $\alpha_{3\omega}$  for the incident and THG waves, respectively,  $w(\vartheta, L)$  may be expressed as:<sup>8-11</sup>

$$4w(\vartheta, L)^2 = [\sigma(\vartheta, L, \eta) \sin \psi_B(\vartheta, L)]^2 + [\delta(\vartheta, L, \eta) \cos \psi_B(\vartheta, L)]^2 \quad (4a)$$

$$\psi(\vartheta, L) = \pi L / 2L_C(\vartheta) \quad (4b)$$

where  $L_C(\vartheta)$  is the coherence length,  $\sigma = [T^{(3\omega)}]^2 + 2T^{(3\omega)}T^{(\omega)}F + [T^{(\omega)}]^2$  and  $\delta = [T^{(3\omega)}]^2 - 2T^{(3\omega)}T^{(\omega)}F + [T^{(\omega)}]^2$ , with  $T^{(3\omega)}$  and  $T^{(\omega)}$  certain transmission factors, and  $F(\beta)$  is a focus function; and  $F(\beta) = 2J_1(\beta)/\beta \approx \exp\{-(\beta/2)^2\}$ ,  $\beta = \pi w_0 \tan \eta / 2L_C(\vartheta) \cos \vartheta$ , with  $w_0$  the beam waist and  $J_1$  is a first-order Bessel function; the approximation is valid for small  $\beta$ . and  $F(\beta)$  is unity for a slab cell. With  $\alpha = \mu L / \cos \vartheta$ , where  $\mu$  is the extinction coefficient,  $T^{(3\omega)} = Q^{(3\omega)} \exp(-\alpha_{3\omega}/2)$  and  $T^{(\omega)} = Q^{(\omega)} \exp(-\alpha_\omega)$ , where the Fresnel factors  $Q^{(3\omega)}$  and  $Q^{(\omega)}$  decrease slowly with increasing  $\vartheta$ .<sup>8,11</sup>

The coherence length  $L_C(\vartheta)$  may be expressed as<sup>8-11</sup>

$$L_C(\vartheta) = \lambda_\omega / 6 | n_{3\omega} \cos(\vartheta'_{3\omega}) - n_\omega \cos(\vartheta'_\omega) | \quad (5)$$

where  $L_C(0) = \lambda_\omega / 6 | n_{3\omega} - n_\omega |$ , with  $\lambda_\omega$  the fundamental wavelength; the primes denote propagation angles measured in the sample, related to angles in air through Snell's law, using the appropriate refractive index, see below. The effect of weak focusing of the incident beam is neglected as too small to be important under the conditions used.<sup>8</sup> In practice, the parameter  $K_R$  is evaluated by determination of  $R_{\sigma\mu;v}^{(3\omega)}(0)$  for the response to a standard with known  $|\chi_{EFF}^{(3)}|$ ,  $n_{3\omega}$ ,  $n_\omega$ , and thickness  $L$ . It should be noted that  $R_{\sigma\mu;v}^{(3\omega)}(0,L)$  may take on any value from zero to its maximum value  $R_{\sigma\mu;v}^{(3\omega)MAX}$  for  $\psi = 0$ , as  $w(\vartheta,L)$  is not usually zero at  $\vartheta = 0$ . However, if Eqns. 2-4 apply,  $\sin \psi$  may be taken as unity for the successive maxima in the fringe pattern, providing a method to estimate  $|\chi_{EFF}^{(3)}| / | n_{3\omega}^2 - n_\omega^2 |$  from data on  $R_{\sigma\mu;v}^{(3\omega)}(\vartheta,L)$ . With the wedge-shaped cell, since  $\vartheta \approx 0$  and  $L_C(\vartheta) \approx L_C(0)$ , the separation  $\Delta'_M$  between the minima in the MFP is given by  $(\Delta'_M/2) \tan \eta = L_C(0) = \lambda_\omega / 6 | n_{3\omega} - n_\omega |$ , providing a means to determine  $| n_{3\omega} - n_\omega |$ . Given this value, the parameter  $| n_{3\omega}^2 - n_\omega^2 |$  needed to compute  $|\chi_{EFF}^{(3)}|$  from  $R_{\sigma\mu;v}^{(3\omega)}(\vartheta,L)$  may be computed given either  $n_{3\omega}$  or  $n_\omega$  e.g.,  $| n_{3\omega}^2 - n_\omega^2 | \approx 2n_{3\omega} | n_{3\omega} - n_\omega |$ .

### 1.3 Results

**1.3.1 Linear Optical Behavior** The linear optical behavior is important in several respects in the analysis of the nonlinear data: the refractive index must be evaluated as a function of the wavelength, and must be known for both the extraordinary and ordinary waves for nematic samples; the absorption and fluorescence must be known for all optical conditions of interest. In addition, the linear optical properties serve to characterize the alignment in the nematic sample.

Data on the refractive index as a function of frequency (wavelength) given in reference 7 for a monodomain preparation of PBZT ( $\varphi = 0.055$ ) are reproduced in Fig. 2 for convenience. Values of the extraordinary and ordinary refractive indices  $n_E$  and  $n_O$  were determined by conoscopic microscopy.<sup>7</sup> The data on each may be fit by the Cauchy relation:

$$\frac{n^2 - 1}{n^2 + 2} = \frac{K\lambda_m^{-2}}{\lambda_m^{-2} + \lambda^{-2}} \quad (6)$$

where  $K$  and  $\lambda_m^{-2}$  are constants ( $K\lambda_m^{-2}$  is presumed to be an oscillator strength for an absorption peaked at  $\lambda_m^{-2}$  in the simplest model). The data give  $\lambda_m = 260$  nm and  $K = 0.27$  for the extraordinary ray, and  $\lambda_m = 225$  nm and  $K = 0.25$  ordinary ray.

The data on  $n_E$  and  $n_O$  may be used to calculate the refractive index  $n_e(\vartheta')$  for a wave propagating at angle  $\vartheta'$  in the material with respect to the optic axis;  $\vartheta'$  and the corresponding external angle  $\vartheta$  in air are related through the use of Snell's law:<sup>12</sup>

$$n_e(\vartheta') = \left\{ \left( \frac{\cos(\vartheta')}{n_E} \right)^2 + \left( \frac{\sin(\vartheta')}{n_O} \right)^2 \right\}^{-1/2} \quad (7)$$

The use of orthoscopic microscopy showed the nematic preparations used here to be free of defects, and conoscopic microscopy showed that they were well aligned. The samples were also characterized by a fluorescence method described elsewhere<sup>3</sup> that probes the

alignment within  $\approx 1 \mu\text{m}$  of the surface, to show that the surface layers were well aligned in the direction of the bulk alignment.

The data in Fig. 2 may be used to determine the coherence length  $L_c(\vartheta)_{\sigma_{\text{H}},\text{v}}$  needed to compute the third-order susceptibility from THG data for the nematic sample studied here if a simple nematic symmetry is assumed; see below for an elaboration of this consideration. Values for the systems of interest are given in Table 1 and Fig. 3. It may be observed that the  $L_c(0)_{\sigma_{\text{H}},\text{v}}$  vary among the experimental arrangements of interests, but that the ratios  $[L_c(\vartheta)/L_c(0)]_{\sigma_{\text{H}},\text{v}}$  are essentially the same for most arrangement, differing significantly only for  $[L_c(\vartheta)/L_c(0)]_{\text{HH},\text{h}}$  and  $[L_c(\vartheta)/L_c(0)]_{\text{VH},\text{h}}$ . The latter demonstrate smaller and larger variations with  $\vartheta$ , respectively, than do the remaining ratios; the affect of these differences on the MFP is discussed below. It may be noted that for a hypothetical isotropic solution with refractive index given by  $(n_E + 2n_O)/3$ ,  $L_c(0) \approx 2.18 \mu\text{m}$  is intermediate to the values given in Table 1, and  $L_c(\vartheta)/L_c(0)$  is close to curve 2.

The THG experiments involve a fundamental wave with infrared wavelength, and a third harmonic wave in the visible region. The absorbance of the solutions studied is essentially that of the solvent for wavelengths in excess of 1500 nm. A slowly increasing absorbance is found for MSA (and the solutions studied here) for wavelengths in the range 1700 to 2200 nm, see Fig. 4. Thus, the solutions of interest are (essentially) transparent for input radiation at 1542 nm, but are weakly absorbent at 1907 nm (absorbance equal to 0.28 for 350  $\mu\text{m}$  path length). The latter is sufficient, however, to have a noticeable influence on the Maker fringe pattern, i.e., through the parameter  $\alpha_\omega$  in Eqn. 4, see below. By contrast, with input radiation at 1064 nm, the THG light is strongly absorbed, with resultant fluorescence, see below.

Pure (undiluted) PBZT is characterized by an absorption band centered around 436 nm that extends to the near green, and is transparent for radiation in the near IR spectrum. However, owing to protonation in the strong protic acid MSA, the absorption properties are different for PBZT in MSA solutions. The absorbance for aligned nematic solutions of PBZT exhibits dichroism, with the absorbance larger for light polarized along the director. Absorption spectra for solutions of PBZT ( $\varphi = 0.021$ ), BZT-18 ( $\varphi = 0.0054$ ), and BZT-36 ( $\varphi = 0.004$ ) in 350  $\mu\text{m}$  path length cells are shown in Fig. 4. The absorbance for the solutions of the model compounds is more pronounced than that for PBZT solutions in the visible. The solution of BZT-18 has a more pronounced absorption than those for either BZT-36 and PBZT, becoming essentially "opaque" at 514 nm.

Absorption in the visible produces fluorescence emission with solutions of PBZT, potentially complicating interpretation of the observations reported above. Thus, with 1064 nm wavelength incident radiation, the 355 nm THG light is strongly absorbed, and produces a strong fluorescence emission, peaked near 520 nm and tailing off to 650 nm, see Fig. 4. By contrast, with 1542 nm wavelength incident light, no fluorescence emission is observed from 540 to 650 nm, indicating the absence of fluorescence emission that could complicate the measurements for a THG wavelength of 514 nm.

**1.3.2 NLO Studies on Isotropic Solutions of PBZT and Model Compounds** The response  $R_{\text{VV}}^{(3\omega)}(\vartheta, L)$  is shown in Figs. 5 and 6 for an isotropic solution of PBZT ( $\varphi = 0.021$ ) for data obtained in a wedge-shaped cell ( $\eta = 0.95$ ) and a rotating slab for incident wavelengths of 1542 and 1907 nm (the subscript v is suppressed for an isotropic sample). In all cases,  $R_{\text{HV}}^{(3\omega)}(\vartheta, L) \approx R_{\text{VH}}^{(3\omega)}(\vartheta, L) \approx 0$ . The effects of the absorption of the incident light at 1907 nm are evident in the decreasing amplitude of the periodic response with increasing  $L$ , but the response for 1542 nm incident light shows no such behavior even though the PBZT isotropic solution used has similar absorption coefficients at 1907 and 514 nm (the

wavelength of the THG from 1542 nm incident light). This is in accord with the behavior expected with Eqn. 4. These measurements illustrate that the effects of the absorption are readily revealed and accounted for in experiments using either wedge-shaped or rotating slab cells. It may be noted that the effect of the absorption is greater on the amplitude of the intensity of the MFP than on the minimum intensity in both cases. The minimum-to-minimum separation  $\Delta'_{\text{M}}$  of the fringes gives  $|n_{3\omega} - n_{\omega}|$  equal to 0.0435 and 0.0225 for  $\lambda_{\omega}$  equal to 1.542 and 1.907  $\mu\text{m}$ , respectively. The appearance of nonzero minima is attributed to beam width effects (i.e., factor  $F(\beta)$  in Eqn. 4).

As shown in Fig. 7, the MFP obtained with the dilute solutions of the model compounds are substantially affected by absorption at the THG wavelength. The solution with BZT-18 has a high absorbance at 514 nm, and produces a strongly attenuated, though still detectable, MFP.

**1.3.3 NLO Studies on Monodomain Nematic Solutions of PBZT** As mentioned in the Introduction, prior studies on a monodomain nematic solution of PBZT showed that THG produced with incident light plane polarized along the nematic director was elliptically polarized. Correspondingly, the Maker fringe patterns obtained from rotation of a flat plate sample varied with the polarization directions of the incident and THG light with respect to the director of the nematic, and did not always exhibit minima that dropped to zero. Examples of the MFP obtained for  $R_{\text{VV};\text{v}}^{(3\omega)}$ ,  $R_{\text{HV};\text{v}}^{(3\omega)}$ ,  $R_{\text{VV};\text{h}}^{(3\omega)}$  and  $R_{\text{VH};\text{h}}^{(3\omega)}$  using a rotating-slab cell are shown in Fig. 8. Attempts to obtain data with a wedge-shaped cell were not successful, resulting in only unresolved fringe patterns, despite the normal appearance of the conoscopic interference figures, see the Discussion.

The data in Fig. 9 were obtained for  $R_{\Omega\text{V};\text{v}}^{(3\omega)}(\vartheta, L)$  for several values of the rotation angle  $\vartheta$  (0, 10, 20, 40, and 50 degrees), where  $\Omega$  is the rotation of the analyzer with respect to the vertical direction (the optic axis), i.e., at fixed  $\vartheta$  and  $L$ ;  $R_{\Omega\text{V};\text{v}}^{(3\omega)}$  varies from  $R_{\text{VV};\text{v}}^{(3\omega)}$  to  $R_{\text{HV};\text{v}}^{(3\omega)}$  as  $|\Omega|$  varies from 0 to 90 degrees. In this case,  $n_{\omega} = n_{\omega;\text{E}}$  but  $n_{3\omega}$  varies from  $n_{3\omega;\text{E}}$  to  $n_{3\omega;\text{O}}$  as  $|\Omega|$  varies from 0 to 90 degrees, respectively, with neither  $n_{3\omega;\text{E}}$  nor  $n_{3\omega;\text{O}}$  dependent on  $\vartheta$ . Data as a function of  $\vartheta$  at fixed  $\Omega$  would generate MFP families parametric in  $\Omega$ ; e.g., the patterns given above for  $R_{\text{VV};\text{v}}^{(3\omega)}$  and  $R_{\text{HV};\text{v}}^{(3\omega)}$  correspond to  $\Omega$  equal to 0 and 90, respectively, and the angles  $\Omega_{\text{max}}$  and  $\Omega_{\text{min}} \approx \Omega_{\text{max}} \pm \pi/2$  for the maximum and minima in  $R_{\Omega\text{V};\text{v}}^{(3\omega)}(\vartheta, L)$  vary with  $\vartheta$ . The function  $R_{\Omega\text{V};\text{v}}^{(3\omega)}(\vartheta, L) - R_{\Omega_{\text{max}}\text{V};\text{v}}^{(3\omega)}(\vartheta, L)$  versus  $\Omega - \Omega_{\text{max}}$  is essentially independent of  $\vartheta$  for  $|\Omega - \Omega_{\text{max}}| < \pi/4$ , but deviations appear as  $\Omega$  approaches  $\Omega_{\text{min}}$ , reflecting the variation in  $R_{\Omega_{\text{max}}\text{V};\text{v}}^{(3\omega)}(\vartheta, L) - R_{\Omega_{\text{min}}\text{V};\text{v}}^{(3\omega)}(\vartheta, L)$  with  $\vartheta$  (e.g., see Fig. 9).

The data in Fig. 10 show  $R_{\text{U}\Theta;\text{v}}^{(3\omega)}(0, L)$  and  $R_{\Theta\Theta;\text{v}}^{(3\omega)}(0, L)$ , where  $\Theta$  is the rotation of the polarization of the incident wave with respect to the vertical direction (the optic axis); the intensity of THG wave was determined without an analyzer for  $R_{\text{U}\Theta;\text{v}}^{(3\omega)}(0, L)$ , and with the analyzer parallel to the polarization of the incident wave for  $R_{\Theta\Theta;\text{v}}^{(3\omega)}(0, L)$ . The data shown were obtained with  $L = 350 \mu\text{m}$  for a sample with  $\phi = 0.055$ ; similar results were obtained for a sample with  $L = 200 \mu\text{m}$  for a sample with  $\phi = 0.045$ . In this case, it is assumed that the fundamental propagates as waves polarized along and orthogonal to the optic axis of the nematic, each generating elliptically polarized THG waves in principal. Both  $R_{\text{U}\Theta;\text{v}}^{(3\omega)}(0, L)$  and  $R_{\Theta\Theta;\text{v}}^{(3\omega)}(0, L)$  are symmetric about  $\Theta = 0$ , with maxima for  $\Theta \neq 0$ , and minima for  $\Theta \approx 90$  degrees. The values of  $|\Theta|_{\text{max}}$  for the maxima differ slightly for the data on  $R_{\text{U}\Theta;\text{v}}^{(3\omega)}(0, L)$  and  $R_{\Theta\Theta;\text{v}}^{(3\omega)}(0, L)$ , with  $|\Theta|_{\text{max}}$  about 40 and 50 degrees for  $R_{\text{U}\Theta;\text{v}}^{(3\omega)}(0, L)$  and  $R_{\Theta\Theta;\text{v}}^{(3\omega)}(0, L)$ , respectively.

## 1.4 Data Analysis

**1.4.1 Isotropic Solutions of PBZT and Model Compounds** With the isotropic solutions, the measured susceptibility  $|\chi_{\text{EFF}}^{(3)}| = \chi_{\text{ISO}}^{(3)}$  is related to the components  $\chi_{\text{EFF}}^{(3)}$  of the tensor  $\chi^{(3)}(-3\omega, \omega, \omega, \omega)$  by the expression  $\chi_{\text{ISO}}^{(3)} = \Sigma \chi_{\text{EFF}}^{(3)} / 5$ .<sup>13</sup> Calculation of  $|\chi_{\text{EFF}}^{(3)}| = \chi_{\text{ISO}}^{(3)}$  from the MFP requires a value of  $|n_{3\omega}^2 - n_{\omega}^2| = |n_{3\omega} - n_{\omega}|(n_{3\omega} + n_{\omega}) \approx 2n_{3\omega}|n_{3\omega} - n_{\omega}|$ . Since  $|n_{3\omega} - n_{\omega}|$  may be determined from the minima separation  $\Delta \ell_M$  of the MFP from the wedge-shaped cell, calculation of  $|\chi_{\text{EFF}}^{(3)}|$  from the data requires in addition a value of  $n_{3\omega}$  (or  $n_{\omega}$ ). Data on the extraordinary and ordinary refractive indices  $n_E$  and  $n_O$ , respectively, were given in a previous study over the range  $1.1 \leq \phi \leq 2.2$ .<sup>7</sup> The refractive index  $n_{\text{ISO}}$  for the isotropic solution may be calculated as  $n_{\text{ISO}} = \{n_E + 2n_O\}/3$  at each frequency in that concentration range, but the technique used in that study does not apply to the isotropic samples, and no measurements were reported for  $\phi = 0.021$ . A linear dependence of  $n_{\text{ISO}}$  on  $\phi$  is assumed to estimate  $n_{3\omega}$  for that composition. This estimate agrees with that obtained by the use of the published refractive index increment  $\partial n / \partial c = 0.26$  mL/g ( $\lambda = 633$  nm) for solutions of PBZT in MSA.<sup>7</sup> Use of these data and the results for  $R_{\text{VV}}^{(3\omega)}(\vartheta, L)$  shown in Fig. 6 (with an appropriate value for  $K_R$ ) gives  $\chi_{\text{ISO}}^{(3)} / \varphi \approx 2 \times 10^{-11}$  (see Table 2) and  $1.5 \times 10^{-11}$  e.s.u. at  $\lambda_{\omega} = 1542$  and  $1907$  nm, respectively, for the isotropic solution of PBZT studied. Further, the correspondence of the results in the wedge-shaped and flat cells confirms the previous conclusion that the contributions to the THG from the walls with flat cells may be neglected for these materials in the concentration range studied.

The estimates of  $n_{3\omega}$  and  $n_{\omega}$  permit calculation of MFP for comparison with the observed data. In these calculations, it is found that  $L_c(\vartheta)/L_c(0)$  is essentially independent of the values of  $n_{3\omega}$  and  $n_{\omega}$  used within a reasonable range of these variables, making the calculated MFP nearly identical for a given ratio  $L/L_c(0) = (6/\lambda_{\omega})|n_{3\omega} - n_{\omega}|L$  for the range of  $L_c(\vartheta)/L_c(0)$  of interest here, whatever the individual values of  $L$ ,  $n_{3\omega}$  and  $n_{\omega}$  greatly simplifying the calculations to determine  $L/L_c(0)$  from the MFP with the slab-shaped cell. For  $L \gg L_c(0)$ , as is the case here, MFP calculated with  $L/2L_c(0)$  differing by an integer tend to have a similar shape (over a reasonable range in  $n_{3\omega}$  or  $n_{\omega}$ ), with the peaks for  $\vartheta > 0$  in the MFP appearing at slightly smaller  $\vartheta$  with increasing  $L$ . The data on  $\Delta \ell_M$  from the wedge-shaped cell give  $|n_{3\omega} - n_{\omega}|$ , and an independent estimate for  $L_c(0) = \lambda_{\omega}/6|n_{3\omega} - n_{\omega}|$ . The MFP shown in Fig. 6 were calculated treating  $L/L_c(0)$  as an adjustable parameter; an experimentally determined absorbance of 0.28 was used for the fundamental wavelength for the MFP at  $1.907 \mu\text{m}$ . Experimental results for  $L_c(0)$  determined with the wedge and slab-shaped cells are as follows ( $\phi = 0.021$ ):

$\lambda_{\omega}/\mu\text{m}$	$L_c(0)/\mu\text{m}$ Wedge cell	$L_c(0)/\mu\text{m}$ Slab cell
1.542	5.91	7.17
1.907	14.13	11.42

Alternatively, with the sample thickness would have to be arbitrarily modified to  $288 \mu\text{m}$  and  $433 \mu\text{m}$  for incident light of  $1.542$  and  $1.907 \mu\text{m}$ , respectively. The unexpected deviation of between estimates of  $L_c(0)$  determined using the wedge and slab cells is examined in the Discussion.

As discussed above, the MFP obtained with the dilute solutions of the model compounds are substantially affected by absorption at the THG wavelength. The solution with BZT-18 has a high absorbance at  $514$  nm, and produces a strongly attenuated,

though still detectable, MFP. The MFP for the solution of BZT-36 reveals the effects of the absorption at  $3\omega$ , but provides data that may be analyzed for  $\chi^{(3)}$ , after taking account of the effects of the absorption using Eqn. 4. The estimate  $\chi_{\text{ISO}}^{(3)}/\phi \cong 10^{-11}$  e.s.u. obtained (see Table 2) is subject to uncertainty ( $\approx \pm 20\%$ ), given the assumptions made in the data analysis for the MFP, and may represent a resonance enhanced response.

**1.4.2 Monodomain Nematic Solutions of PBZT** The strongly birefringent character of nematic solutions of PBZT complicates the interpretation of the THG behavior for the monodomain nematic solutions. For such materials,  $|\chi_{\text{EFF}}^{(3)}|_{\sigma\mu;\nu}$  is related to the components of  $\chi^{(3)}(-3\omega;\omega,\omega,\omega)$  selected by the polarizations  $e_\mu$  and  $e_\sigma$  of the fundamental and THG waves, respectively, relative to the orientation of the optic axis:<sup>13</sup>

$$|\chi_{\text{EFF}}^{(3)}|_{\sigma\mu;\nu} = \left| \sum_{i,j} \chi_{ijj}^{(3)}(-3\omega;\omega,\omega,\omega)(e_\sigma)_i (e_\mu)_j \right|_\nu \quad (7)$$

For example, for  $R_{VV;\nu}^{(3\omega)}$ ,  $R_{VV;\nu}^{(3\omega)}$  (or  $R_{III;\nu}^{(3\omega)}$ ) and  $R_{HV;\nu}^{(3\omega)}$  the effective third-order susceptibilities  $(\chi \backslash O^{(3)})_{\text{EFF}}^{(3)}$  are equated to the components  $\chi_{xxxx}^{(3)}$ ,  $\chi_{xyyy}^{(3)}$  and  $\chi_{xyxx}^{(3)}$  of  $\chi^{(3)}$ , respectively, in a Cartesian coordinate system with  $x$  along the director  $\hat{n}$ . The situation is more complex for  $R_{VH;\nu}^{(3\omega)}$  and  $R_{HH;\nu}^{(3\omega)}$ . For example,  $(\chi_{\text{EFF}}^{(3)})_{III;\nu}$  and  $(\chi_{\text{EFF}}^{(3)})_{VH;\nu}$  correspond to  $\chi_{xyyy}^{(3)}$  as  $\vartheta$  increases to 90 degrees for a material with uniaxial nematic symmetry, but  $(\chi_{\text{EFF}}^{(3)})_{HH;\nu}$  and  $(\chi_{\text{EFF}}^{(3)})_{VH;\nu}$  correspond to  $\chi_{xxxx}^{(3)}$  and  $\chi_{xyxx}^{(3)}$ , respectively, for  $\vartheta = 0$ .

Although the fringe spacing observed for the various arrangements change qualitatively as expected for the appropriate coherence lengths, in no case could the data be fitted even approximately by Eqn.s. 2–4 using the measured refractive indices and sample thickness. The deviation was too large to attribute to any reasonable uncertainty in these parameters, see below. Further, the MFP for  $R_{VV;\nu}^{(3\omega)}$  exhibits strongly nonzero minima, a feature unexpected for a homogeneous sample in the absence of absorption, surface defects, beam divergence or nonparallelism of the input and output faces (the last three of these are rejected on the basis of the zero minima obtained with the MFP on the isotropic samples; absorption effects are discussed below). The MFP with  $R_{VV;\nu}^{(3\omega)}$  for nematic solutions of PBZT is similar in appearance to the MFP for  $R \backslash O^{(3\omega)}_{VV}$  for isotropic samples (e.g.,  $R_{VV;\nu}^{(3\omega)} = 0$  at the minima, and  $R_{VV;\nu}^{(3\omega)}$  decreasing slightly with increasing  $|\vartheta|$  at the maxima). Nevertheless, careful examination reveals secondary structure on the principle fringe pattern, not present with the MFP for the isotropic sample. As expected,  $R_{VH;\nu}^{(3\omega)}$  and  $R_{HV;\nu}^{(3\omega)}$  are equal for  $\vartheta = 0$ , differing for larger  $\vartheta$  qualitatively in as expected for the appropriate coherence lengths. Data on  $R_{VH;\nu}^{(3\omega)}$  and  $R_{HV;\nu}^{(3\omega)}$  were both essentially null for nematic solutions of PBZT.

With nematic symmetry,  $\chi_{xyxx}^{(3)}$  is expected to be zero (in the Cartesian coordinates used here),<sup>13</sup> whereas an appreciable intensity is observed for both  $R_{HV;\nu}^{(3\omega)}$  and  $R_{VH;\nu}^{(3\omega)}$  for the PBZT sample, with MFP that do not exhibit zero intensity minima, see Fig. 9. By contrast, as expected for nematic symmetry, for which  $\chi_{xyyy}^{(3)}$  is zero, both  $R_{VH;\nu}^{(3\omega)}$  and  $R_{HV;\nu}^{(3\omega)}$  were negligible. These features are discussed in the following section, but it is convenient to remark here that the behavior is not caused in a simple way by the effects of the observed absorbance of the sample at either  $\omega$  or  $3\omega$ . The data in Figs. 6 and 7 on an isotropic solution ( $\phi = 0.021$ ) show that absorption is not a factor with  $\lambda_\omega = 1542$  nm, and estimates based on experimental absorbances at  $\lambda_\omega$  and  $\lambda_{3\omega}$  indicate that absorbance effects should also be negligible for the nematic solution studied ( $\phi = 0.055$ ). Furthermore,



as may be seen, for example, in Fig. 6, the effects of absorbance on the MFP with a rotating slab give distinctly different effects than those found for the MFP of the nematic sample. Thus, an effect other than that absorption must be implicated in the observed form of the MFP for the nematic sample.

The MFP may be calculated if nematic symmetry is assumed, so that the state of polarizations of the nonlinear waves may be taken to be those defined by the polarizer and analyzer. In general, the coherence length depends on the polarizations of the waves and orientation of  $\vec{n}$ , and as discussed above,  $L_c(\vartheta)_{\sigma\mu;\nu}$  must be computed with the appropriate refractive indices (taking care to compute the angle  $\vartheta'$  of propagation in the solution from  $\vartheta$  and the use of Snell's law, e.g., see Table 1 and Fig. 3). The variation of  $L_c(0)_{\sigma\mu;\nu}$  and  $L_c(\vartheta)_{\sigma\mu;\nu}/L_c(0)_{\sigma\mu;\nu}$  among the conditions used is reflected in the wide variation of the MFP obtained. For example, although  $R_{\text{HV};\nu}^{(3\omega)}(\vartheta, L)$  and  $R_{\text{VH};h}^{(3\omega)}(\vartheta, L)$  given in Fig. 8 share the same  $L_c(0)$ , making  $R_{\text{HV};\nu}^{(3\omega)}(0, L) = R_{\text{VH};h}^{(3\omega)}(0, L)$ , the dependence of  $[L_c(\vartheta)/L_c(0)]_{\text{VH};h}$  on  $\vartheta$  is much larger than that of  $[L_c(\vartheta)/L_c(0)]_{\text{HV};\nu}$ , resulting in very different MFP, see Fig. 8. Similarly, the peak-to-peak separation of the fringes decreases with increasing  $L/L_c(0)_{\sigma\mu;\nu}$ , as expected. Despite these qualitatively reasonable features, attempts to compute MFP show that far fewer fringes are observed than expected for the physical thickness  $L$  and the  $|n_{3\omega} - n_\omega|$  measured for the material (see Fig. 2 for the latter). Further, different  $L$  would be required for the various geometries if calculated from the observed  $|n_{3\omega} - n_\omega|$  and the value of  $L/L_c(0)_{\sigma\mu;\nu}$  required to match the periodicities of the calculated and observed MFP; in addition, the calculated MFP exhibits zero minima, in contrast to the observed behavior. For example, using the measured sample thicknesses of 350  $\mu\text{m}$ , values of  $L_c(0)$  of 2.46, 8.19 and 33.07  $\mu\text{m}$  were required to emulate the fringe spacing for  $R_{\text{VV};\nu}^{(3\omega)}$ ,  $R_{\text{VV};h}^{(3\omega)}$  and  $R_{\text{HV};\nu}^{(3\omega)}$ , respectively, in comparison with the values given in Table 1 calculated from the measured refractive indices. Alternatively, use of the calculated coherence lengths would require arbitrary adjustments of the sample thickness to 218, 118 and 58  $\mu\text{m}$  for  $R_{\text{VV};\nu}^{(3\omega)}$ ,  $R_{\text{VV};h}^{(3\omega)}$  and  $R_{\text{HV};\nu}^{(3\omega)}$ . This aspect of the data is revisited in the Discussion.

Given the ambiguities in the interpretation of the MFP for the nematic sample, there is no certain means to estimate or interpret  $|\chi_{\text{EFF};\sigma\mu;\nu}^{(3)}|$  from the data. In order to proceed, at least on a qualitative basis, estimates of  $|\chi_{\text{EFF};\sigma\mu;\nu}^{(3)}|/\varphi$  given in Table 2 were calculated using appropriate values of  $n_\omega$  and  $n_{3\omega}$ , on the assumption that  $w(\vartheta, L)$  is essentially unity at the first maximum for  $\vartheta \neq 0$ ; these, see Table 1.

It may be seen that  $R_{\Omega\text{V};\nu}^{(3\omega)}(\vartheta, L)$  never decreases to zero for any value of  $\Omega$ , showing that the THG light is either elliptically polarized, or a mixture of differently polarized rays (a plane polarized ray mixed with either an unpolarized or an elliptically polarized ray)<sup>2</sup>. This is not expected for a material with nematic symmetry, and as discussed below, is associated with the behavior described in the preceding paragraph.

## 1.5 Discussion

### 1.5.1 Isotropic Solution of PBZT and Model Compounds

Three features of the behavior observed with the isotropic solution of PBZT and its model compounds are noteworthy: (1) The coherence lengths  $L_c(0)$  observed with the wedge and slab-shaped cells did not agree, (2) the estimate of  $\chi_{\text{IS}^{(3\omega)}}^{(3)}/\varphi$  obtained for the polymer and model compound BZT-36 were similar, and (3) both  $R_{\text{HV}}^{(3\omega)}(\vartheta, L)$  and  $R_{\text{VH}}^{(3\omega)}(\vartheta, L)$  were nil. The model compounds were structurally designed to enhance their NLO response over that obtained with the unmodified model of the repeat unit of PBZT<sup>14</sup>, at the cost of increased absorption. It is noteworthy that the THG generation with the polymer is similarly enhanced over that for the repeat unit, without the large increase in the absorption. Evidently, the electronic states involved in the NLO behavior for the polymer extend over several repeat units of the chain.

The orientational averages simplify  $\chi^{(3)}(-3\omega; \omega, \omega, \omega)$  for an isotropic material,<sup>13</sup> leading, for example, to the expectation that  $R_{\text{IV}}^{(3\omega)}$  (or  $R_{\text{VII}}^{(3\omega)}$ ) should be nil, and that  $R_{\text{VV}}^{(3\omega)}$  and  $R_{\text{HH}}^{(3\omega)}$  should be equivalent, as observed. The failure to obtain equivalent values of  $L_c(0)$  in experiments with the wedge and slab-shaped cells is attributed to surface layers that differ in optical properties from the solution in the bulk of the cell. A possible source for this behavior could be a tendency for the rodlike PBZT chains to align near the surface with their axes parallel to the surface, but otherwise not (globally) ordered. A tendency for this to propagate some distance from the surface would produce a negatively birefringent uniaxial layer, with the unique axis perpendicular to the surface. The presence of such thin surface layers would not affect the MFP obtained from a wedge-shaped cell, but could affect that obtained with on rotation of a slab. Thus, the interference function becomes (for focus factor  $F$  equal to unity)<sup>11</sup>

$$4W^2 = \{\rho_B \sigma_B \sin \psi_B\}^2 + 2\rho_B \rho_S \sigma_B [\sigma_{S1} + \sigma_{S2}] \sin \psi_S \sin \psi_B \cos(\psi_S + \psi_B) \\ + \{\sigma_{S1}^2 + \sigma_{S2}^2 + 2\sigma_{S1}\sigma_{S2}\cos[2(\psi_S + \psi_B)]\} \{\rho_S \sin \psi_S\}^2 \\ + \{\rho_B \delta_B \cos \psi_B\}^2 + 2\rho_B \rho_S \delta_B [\delta_{S1} + \delta_{S2}] \cos \psi_S \cos \psi_B \cos(\psi_S + \psi_B) \\ + \{\delta_{S1}^2 + \delta_{S2}^2 + 2\delta_{S1}\delta_{S2}\cos[2(\psi_S + \psi_B)]\} \{\rho_S \cos \psi_S\}^2 \quad (8)$$

where  $\rho_k = (|\chi_{\text{EFF}}^{(3)}| / |n_{3\omega}^2 - n_\omega^2|)_k$ ,  $\sigma_k = (T^{(3\omega)} + T^{(\omega)})_k$  and  $\delta_k = (T^{(3\omega)} - T^{(\omega)})_k$  (the expression for a bilayer is obtained if, e.g.,  $\sigma_{S2} = \delta_{S2} = 0$ , and Eqn. 3-4 is recovered if  $\rho_S = 0$ ). The subscripts s1 and s2 refer to the two surface layers, assumed to have common lengths and optical properties, with the possible exception of their transmission factors. If all transmission factors are equal to a function  $T(\vartheta)$ , Eqn (9) simplifies to<sup>10</sup>

$$W^2 = T(\vartheta)^2 \{[\rho_B \sin \psi_B]^2 + 4\rho_B \rho_S \sin \psi_S \sin \psi_B \cos(\psi_S + \psi_B) + [2\rho_S \cos(\psi_S + \psi_B) \sin \psi_S]^2\} \\ = T(\vartheta)^2 \{[\rho_B \sin \psi_B + 2\rho_S \cos(\psi_S + \psi_B) \sin \psi_S]^2\} \quad (9a)$$

$$W = T(\vartheta) \{\rho_B \sin \psi_B + \pi \rho_S [L/L_c(0)]_S \cos(\psi_B)\} \quad (9b)$$

where Eqn (9b) applies for thin layers ( $L_S \ll [L_c(0)]_S$ ). With Eqn (9), the MFP displays zero minima, but with a periodicity that depends on the coherence lengths  $[L_c(0)]_S$  and  $[L_c(0)]_B$ , as well as the coefficients  $\rho_B$  and  $\rho_S$ , similar to the MFP observed for the isotropic PBZT solution with 1.542  $\mu\text{m}$  wavelength incident light. Nevertheless, calculations show that the observed MFP for this case would require an unreasonably small  $|n_{3\omega} - n_\omega|$  for the bulk, suggesting that the assumption of equal transmission factors may be inaccurate. Equation (8) produces MFP with nonzero minima if the transmission factors are unequal, as through the effects of absorption, similar to the MFP for the isotropic PBZT solution with 1.907  $\mu\text{m}$  wavelength incident light. Although the use of Eqn (8) introduces additional flexibility in fitting data, it is at the cost of additional parameters, some of which may be unknown. The requirement that the surface layers be the same at the two incident wavelengths, and the use of the observed linear refractive indices and absorbance to describe the bulk constrains the parameters that will provide a reasonable fit to the MFP. An illustrative fit to the MFP on the isotropic sample using Eqn. 8 is given in Fig. 11. The fits requires surface layers with  $L_S \approx 35 \mu\text{m}$  and  $\rho_B \approx 3\rho_S$ , and modest absorption for the THG light in the surface layers for, along with the experimental absorption for the incident light. The proposed surface layers appear to be a depletion layers, less concentrated than the bulk. This could obtain if the rodlike chains tend to have their axes parallel to

the surface plane in the surface, thus promoting a decreased concentration if the surface layers are to remain isotropic. The fluorescence emission from a surface layer of  $\approx 1 \mu\text{m}$  thickness and  $\approx 100 \mu\text{m}$  diameter is not polarized, indicating no order in the plane on those dimensions. The THG experiment may be one of the few experiments suited to reveal the existence of the layer, and something of its nature.

**1.5.2 Monodomain Nematic Solutions of PBZT** The possibility of adsorbed surface layers possessing optical properties different from that of the bulk solution presents a number of complications in the analysis of the MFP from the nematic preparations. A residual aligned surface layer observed by fluorescence emission anisotropy for nematic solutions of PBZT heated above their clearing temperature is discussed elsewhere in this report, reinforcing the postulate of a unique surface layer in the nematic solutions. Along with the general pattern of their periodicity, the disparate features of the MFP for the nematic solution that require explanation include (i) the nonzero minima observed in  $R_{VV;v}^{(3\omega)}(\vartheta, L)$ , (ii) the appearance of  $R_{HV;v}^{(3\omega)}(\vartheta, L)$  and  $R_{VH;h}^{(3\omega)}(\vartheta, L)$ , which are both expected to be nil for a material with uniaxial nematic symmetry, (iii) the complex appearance of  $R_{VV;h}^{(3\omega)}(\vartheta, L)$  and (iv) the failure to obtain satisfactory MFP with the nematic solution using the wedge-shaped cell.

The macroscopic first-order (linear) and third-order (nonlinear) susceptibilities  $\chi^{(1)}(-\omega; \omega)$  and  $\chi^{(3)}(-3\omega; \omega, \omega, \omega)$ , respectively, are related to the elementary molecular (repeat-unit) hyperpolarizability tensors  $\gamma^{(1)}(-\omega; \omega)$  and  $\gamma^{(3)}(-3\omega; \omega, \omega, \omega)$  through summations over all of the elementary units, including their orientation:<sup>10,13</sup>

$$\chi^{(1)}(-\omega; \omega) = \epsilon_0^{-1} \sum_{\beta} N_{\beta} \langle \gamma^{(1)}(-\omega; \omega) \rangle_{\beta} f_{\beta}(\omega)^2 \quad (10)$$

$$\chi^{(3)}(-3\omega; \omega, \omega, \omega) = (6\epsilon_0)^{-1} \sum_{\beta} N_{\beta} \langle \gamma^{(3)}(-3\omega; \omega, \omega, \omega) \rangle_{\beta} f_{\beta}(3\omega) f_{\beta}(\omega)^3 \quad (11)$$

where the brackets  $\langle \dots \rangle$  indicate an orientational average,  $N_{\beta}$  is the number of moieties with  $\langle \gamma^{(1)}(-\omega; \omega) \rangle_{\beta}$  or  $\langle \gamma^{(3)}(-3\omega; \omega, \omega, \omega) \rangle_{\beta}$  (assuming these are additive),  $\epsilon_0$  is the free-space permittivity, and it is assumed that the local-field tensors may be represented by a scalar  $f(\omega)$ . It is likely that the symmetry axis of  $\gamma^{(1)}(-\omega; \omega)$  is not that of the macroscopic nematic, and may exhibit biaxial rather than uniaxial symmetry. For example, with PBZT the absorption and emission vectors may be off the long axis of the repeat unit, directed closer to the axis between the two sulfur atoms, see Fig. 1. Nevertheless, when averaged over all moieties and allowed orientations, the macroscopic symmetry for  $\chi^{(1)}$  is uniaxial nematic for nematic solutions of PBZT, i.e., the only nonzero components being  $\chi_{xx}^{(1)}$  and  $\chi_{yy}^{(1)} = \chi_{zz}^{(1)}$  in the laboratory-frame Cartesian coordinates defined above. For example, the symmetric appearance of the conoscopic interference fringes suggests that deviations from the anticipated symmetry are small throughout the sample, as characterized by the refractive index. Further, the fluorescence emission from the surface suggests that any deviation from the anticipated uniaxial nematic symmetry in the layers within  $\approx 1 \mu\text{m}$  from the surface is small or absent over areas with diameter of  $\approx 100 \mu\text{m}$ .

Despite the apparent uniaxial nematic symmetry indicated by  $\chi^{(1)}$ , the observed nonzero intensities for  $R_{\text{HV};v}^{(3\omega)}(\vartheta, L)$  and  $R_{\text{VH};h}^{(3\omega)}(\vartheta, L)$  are attributed to a distribution of orientations in the sample differing from that for uniaxial nematic symmetry. It seems likely that the principal axes defining  $\gamma^{(3)}$  in the molecular-frame will differ from those established for  $\chi^{(3)}$  in the laboratory-frame. Thus, the symmetry of the tensor  $\gamma^{(3)}$  is implicated in the observed behavior. Departures from the aligned nematic structure that would complicate the interpretation of  $\chi^{(3)}$  might come about, for example, by alignments at the surface that differ from that in the bulk of the nematic, or for a tendency for a biaxial rather than a uniaxial nematic symmetry. The layers proposed for the isotropic solutions would be transformed to ordered (possibly biaxial nematic) layers for the nematic solutions. The properties of any such surface layers would have to exhibit overall symmetry along the symmetry axis of the macroscopic nematic in order to be consistent with the behavior observed for  $\chi^{(1)}$ . However, the behavior observed for  $R_{\text{UO};v}^{(3\omega)}(0, L)$  and  $R_{\text{OO};v}^{(3\omega)}(0, L)$  and the nonzero  $R_{\text{HV};v}^{(3\omega)}(\vartheta, L)$  and  $R_{\text{VH};h}^{(3\omega)}(\vartheta, L)$  would require additional features for any surface layers.

As shown in Fig. 12, the observed MFP for  $R_{\text{VV};v}^{(3\omega)}(\vartheta, L)$ ,  $R_{\text{HV};v}^{(3\omega)}(\vartheta, L)$  and  $R_{\text{VV};h}^{(3\omega)}(\vartheta, L)$  may be fitted qualitatively using Eqn. 8 with reasonable optical parameters and a common layer thickness  $L_s \approx 66 \mu\text{m}$  (no fit is attempted to  $R_{\text{VH};h}^{(3\omega)}(\vartheta, L)$  as the required values of  $n_E(\vartheta)$  vary with  $\varphi$ , see Table 1). In these fits, the nonzero minima observed with  $R_{\text{VV};v}^{(3\omega)}(\vartheta, L)$  are attributed to relatively strong absorption in the surface layers, so that most of the THG light is contributed by the bulk sample, with  $\rho_B \approx 0.4\rho_S$ . The complex line shape observed with  $R_{\text{VV};h}^{(3\omega)}(\vartheta, L)$  arises from a mixing of a weak THG intensity from the bulk with a much stronger contribution from the surface ( $\rho_B \approx 0.01\rho_S$ ), with weak absorption owing to the dichroic nature of the nematic phase of PBZT. Although improved fits might be obtained by refinement of the optical parameters used, there is not much motivation to do so without independent verification of the proposed surface layers and measurement of their optical properties. It suffices to assert that the observed MFP may be reasonably explained by the existence of surface layers in which the uniaxial symmetry of the bulk is broken, leading to contributions that give nonzero intensity in  $R_{\text{HV};v}^{(3\omega)}(\vartheta, L)$  (and  $R_{\text{VH};h}^{(3\omega)}(\vartheta, L)$ ), absorption of the fundamental and the THG light (mostly in the surface layers) that leads to the nonzero minima in  $R_{\text{VV};v}^{(3\omega)}(\vartheta, L)$ , and mixing of the THG contributions to the MFP leading to the complex appearance of  $R_{\text{VV};h}^{(3\omega)}(\vartheta, L)$ . Further, the postulated layer structure could reasonably be expected to compromise the formation of MFP using a wedge-shaped cell, even though the linear optical behavior manifested in the conoscopic interference figures appears to be normal.

Deviations from an overall uniaxial nematic symmetry could exist over lengths of the order of a wavelength, without impact on the fluorescence emission anisotropy averaged over a scale of  $\approx 100 \mu\text{m}$ . Such deviations might involve a tendency for the repeat units to align with the sulfur-sulfur axis on near-by units parallel, for example. Conformational computations for PBZT show that the chain tends to take a ribbon-like conformer, with a restricted range about zero angle of the rotational angle around the single bonds connecting the aromatic ring structures, and with a tendency for parallel sulfur-sulfur axes on near-by repeat units. This tendency could be enhanced for molecules near a surface. The persistence of this organization over a distance of the order of a wavelength for molecules near the surface in any biaxial nematic layer could break the nematic symmetry in  $|\chi_{\text{EFF}}^{(3)}|_S$ , and result in the behavior observed for  $R_{\text{UO};v}^{(3\omega)}(0, L)$  and  $R_{\text{OO};v}^{(3\omega)}(0, L)$  and the nonzero values of  $R_{\text{HV};v}^{(3\omega)}(\vartheta, L)$  and  $R_{\text{VH};h}^{(3\omega)}(\vartheta, L)$ , and the unexplained features in  $R_{\text{VV};v}^{(3\omega)}(\vartheta, L)$  and  $R_{\text{VV};h}^{(3\omega)}(\vartheta, L)$ . Thus, the THG generated in the surface layers would be polarized away from the extraordinary or ordinary axes of the nematic.

## 1.6 Conclusion

Study of the nonlinear optical properties of isotropic and nematic solutions of PBZT was initially motivated to elucidate the molecular origin of THG behavior making use of the molecular alignment of the nematic state. The conclusion that THG is complicated by the effects of surface layers for both isotropic and nematic solutions was not anticipated, but represents an interesting and novel result. It is possible that similar surface layers obtain in unrecognized form with solutions many semiflexible polymers, especially those that are nematogenic. Study of the nonlinear optical behavior may afford one of the few techniques to identify such layers, and to characterize their properties in part.

**Table 1**  
**Typical Values of the Coherence Length**  
**Nematic Solutions of PBZT<sup>a</sup>**

$R_{\rho\mu;\nu}^{(3\omega)}$	Component of $\chi_{ijij}^{(3)}$ <sup>b</sup>	(φ = 0.055)		$L_c(0)$ μm
		$n_\omega$	$n_{3\omega}$	
$R_{VH;\nu}^{(3\omega)}$	$\chi_{xyxy}^{(3)}$	$n_{\omega;O}$	$n_{3\omega;E}$	1.20
$R_{HV;h}^{(3\omega)}$	$\chi_{xyxy}^{(3)}$	$n_{\omega;O}$	$n_{3\omega;e}$	1.20
$R_{VV;\nu}^{(3\omega)}$	$\chi_{xxxx}^{(3)}$	$n_{\omega;E}$	$n_{3\omega;E}$	1.53
$R_{HH;h}^{(3\omega)}$	$\chi_{xxxx}^{(3)}$	$n_{\omega;e}$	$n_{3\omega;e}$	1.53
$R_{HH;\nu}^{(3\omega)}$	$\chi_{yyyy}^{(3)}$	$n_{\omega;O}$	$n_{3\omega;O}$	2.76
$R_{VV;h}^{(3\omega)}$	$\chi_{yyyy}^{(3)}$	$n_{\omega;O}$	$n_{3\omega;O}$	2.76
$R_{HV;\nu}^{(3\omega)}$	$\chi_{yxxx}^{(3)}$	$n_{\omega;E}$	$n_{3\omega;O}$	5.48
$R_{VH;h}^{(3\omega)}$	$\chi_{vxxx}^{(3)}$	$n_{\omega;e}$	$n_{3\omega;O}$	5.48

a The assumptions made in the calculations given here are discussed in the text; see Eq. 7 for  $n_e$  definition.

For this solution,  $n_{\omega;O} = 1.4340$ ;  $n_{\omega;E} = 1.4801$   
 $n_{3\omega;O} = 1.5270$ ;  $n_{3\omega;E} = 1.6480$   
 $\lambda_\omega = 1542$  nm

b The components of  $\chi_{ijij}^{(3)}$  are expressed in a Cartesian coordinate system with x along the optic axis and y in the sample plane; components are for  $\vartheta = 0$ .

**Table 2**  
**Third-Order Susceptibilities**  
**for PBZT and Model Compounds**  
 $(\lambda_{\omega} = 1542 \text{ nm})$

Sample	$\phi$	$R_{\rho\mu;\nu}^{(3\omega)}$	Component of $\chi_{ijkl}^{(3)}$ <sup>a</sup>	$10^{11}  \chi_{\text{EFF}}^{(3)}  / \phi$ (e.s.u.)
<b>ISOTROPIC SAMPLES</b>				
PBZT	0.021	$R_{VV}^{(3\omega)}; R_{III}^{(3\omega)}$	$\chi_{\text{ISO}}^{(3)}$	2.0
BZT-18	0.004	$R_{VV}^{(3\omega)}; R_{HH}^{(3\omega)}$	$\chi_{\text{ISO}}^{(3)}$	(1)
BZT-36	0.0054	$R_{VV}^{(3\omega)}; R_{III}^{(3\omega)}$	$\chi_{\text{ISO}}^{(3)}$	1.0
<b>NEMATIC SAMPLE<sup>c</sup></b>				
PBZT	0.055	$R_{VV;\nu}^{(3\omega)}; R_{III;h}^{(3\omega)}$	$\chi_{xxxx}^{(3)}$	4.0
PBZT	0.055	$R_{III;\nu}^{(3\omega)}; R_{VV;h}^{(3\omega)}$	$\chi_{yyyy}^{(3)}$	0.56
PBZT	0.055	$R_{IIV;\nu}^{(3\omega)}; R_{VII;h}^{(3\omega)}$	$\chi_{yxxx}^{(3)}$	0.02
PBZT	0.055	$R_{VII;\nu}^{(3\omega)}; R_{IIV;h}^{(3\omega)}$	$\chi_{xvyv}^{(3)}$	<0.001

- a The components of  $\chi_{ijkl}^{(3)}$  are expressed in a Cartesian coordinate system with x along the optic axis and y in the sample plane.
- b Subject to a large uncertainty owing to strong absorbance at  $3\omega$
- c The assumptions made in the calculation of  $|\chi_{\text{EFF}}^{(3)}|$  are discussed in the text.

## 2. Studies on the Texture of Nematic Solutions of a Rodlike Polymer

### 2.1 Introduction

The unanticipated features of the NLO behavior nematic phase reported in the preceding sections motivated a careful study of the defect structure in nematic solutions of PBZT. As is well known,<sup>15-21</sup> the tendency for order is the source of complex behavior, with this tendency often being frustrated to some extent in polymer nematic fluids. For the rodlike chains of interest here, the order develops as the chain axes tend to become parallel to each other, with the average direction of the axes in an ordered region at position  $\mathbf{r}$  given by a unit vector  $\bar{\mathbf{n}}(\mathbf{r})$  called the director. The order results in anisotropy in, for example, optical and mechanical properties, and the frustration of the order gives rise to defect structures that can influence such behavior. The nature of these effects is discussed in the following, using data on nematic solutions of a rodlike polymer as examples. As discussed below, recent work suggests that undiluted thermotropic nematic polymeric fluids demonstrate similar behavior.

At equilibrium, the nematic field adopts a spatial configuration to minimize the total distortion free energy  $\mathcal{F}_d$ , including the effects of wall-induced alignments, etc. In a so-called *monodomain*,  $\bar{\mathbf{n}}(\mathbf{r})$  is everywhere the same, and the fluid is a uniform, defect-free preparation.<sup>15-17,20</sup> With nematic solutions of high molecular weight rodlike chains, the local orientation fluctuations are somewhat suppressed, diminishing the scattering of light, and giving the monodomain the appearance of a normal isotropic fluid when viewed with natural (unpolarized) light without the use of a polarization analyzer.<sup>3</sup> By comparison, orientation fluctuations are larger for monodomains of small molecule nematics, giving them a turbid appearance.<sup>15</sup> When viewed between crossed polars, a monodomain is observed to exhibit a sharp extinction for light polarized either along or orthogonal to the optic axis (e.g., the chain axis for most rodlike molecules), and may also exhibit dichroism.

**2.2 Order in Monodomains of PBZT Nematic Solutions** The preparation of monodomains of nematic solutions of PBZT between parallel glass plates in the slab geometry has been described in the preceding elsewhere. Briefly, the nematic solution is extruded into a rectangular channel to initiate the process. Immediately after filling, the nematic material is turbid, and exhibits the characteristics of a *mottled* texture, elaborated below. Owing to the aromatic planes in the chain backbone, PBZT will tend to align with its axes along the field direction of an external magnetic field, and a stable monodomain will form in the filled channel after a few hours in an external magnetic field aligned along the former flow direction (e.g., a few hours in a 7T field).<sup>3,7</sup> The birefringence  $\Delta n$  of a monodomain may be determined by conoscopic microscopy or related methods,<sup>7,22</sup> all based on the transmission of light through a birefringent material, relating  $\Delta n$  to the retardation  $\delta$  of the phase of the transmitted light rays, with  $\delta = d_{\text{opt}}\Delta n/\lambda$ , where  $d_{\text{opt}}$  is the optical path length and  $\lambda$  the wavelength of the incident light in vacuo.<sup>12</sup> For a nematic material,  $\Delta n$  is related to the order parameter  $S$  for the uniaxial sample:<sup>7</sup>

$$\Delta n = \Delta n_0 S s(S) \varphi \quad (12)$$

$$S = \frac{1}{2} \{3\langle \bar{\mathbf{u}} \cdot \bar{\mathbf{n}} \rangle^2 - 1\} \quad (13)$$

where  $\langle \dots \rangle$  indicates an ensemble average,  $\bar{\mathbf{u}}$  is a unit vector along a rodlike chain,  $\varphi$  is the solute volume fraction,  $\Delta n_0$  is the value  $\Delta n$  for a fully aligned bulk material,  $S$  is expected



to be a function of  $\phi$ , and  $s(S) \approx 1$ .<sup>7</sup> The order parameter is zero for an isotropic fluid, tends to unity as parallel alignment among the chains increases in a nematic phase, and is expected to be about 0.6 for the onset of the nematic phase.<sup>15</sup> Studies on monodomains of solutions of PBZT have given  $S \approx 0.96$  for the concentration range  $1.1 \leq \phi/\phi_{NI} \leq 2$  at  $T = 25^\circ\text{C}$ , for compositions with a clearing temperatures above  $75^\circ\text{C}$ .<sup>7</sup> This independence of  $S$  from  $\phi$  is somewhat unexpected, and is presently the subject of further study; the observed behavior may reflect the sample preparation in a magnetic field, and the stabilizing effect of the surface. The order parameter is expected to decrease with increasing temperature. An example of the transmission of an incident beam between parallel and crossed polars for a sample with a clearing temperature of  $110^\circ\text{C}$  is shown in Fig. 13. Since the polarization of the incident light was at  $\pi/4$  to the principal optic axis of the nematic, the transmitted intensities  $I_{||}$  and  $I_{\perp}$  between crossed and parallel polars, respectively, are given by<sup>12</sup>

$$I_{\perp} = K I_0 \sin^2(\pi\delta) \quad (14)$$

$$I_{||} = K I_0 \{1 - \sin^2(\pi\delta)\} \quad (15)$$

where  $I_0$  is the intensity of incident light with wavelength  $\lambda$ , and  $K$  is a factor ( $K \leq 1$ ) to account for attenuation of the light by scattering and absorption. Conoscopic microscopy showed that  $\Delta n$  decreased with increasing temperature. Since  $\delta \approx 26$  for the sample for which the data in Fig. 13 were obtained, the six oscillations observed indicate that  $\Delta n$ , and hence  $S$ , decrease by about twenty three percent over the  $70^\circ\text{C}$  interval studied. The effect is reversible over this temperature range. The gradual decrease of  $K$  with increasing temperature may reflect losses due to increased scattering as the order decreases.

Additional behavior that obtains for temperatures closer to the clearing temperature is discussed below. The alignment of chains near the surface of a glass plate may be determined with nematic solutions of PBZT by the use of light with a wavelength that is absorbed within a short distance (i.e., 99% absorption within  $1 \mu\text{m}$ ), and causes anisotropic fluorescence emission, with maximum emission in a direction along the chain axis.<sup>3</sup>

Examples of the ratio  $I_{||}/I_{\perp}$  of the fluorescence intensities  $I_{||}$  and  $I_{\perp}$  along and perpendicular to the flow direction, respectively, are given in Fig. 13 as a function of temperature. The alignment near the surface is seen to decrease slowly with increasing temperature, consistent with the decreasing order parameter.

**2.3 Point Defects in Otherwise Aligned Nematic Solutions of PBZT** Additional features appear with nematic solutions of PBZT as the temperature approaches the clearing temperature  $T_{NI}$ . For example, for the data given in Fig. 13, the conoscopic interference figures are lost, and the rate of decrease of the anisotropy of the fluorescence emission from the surface layers increases with increasing temperature for  $T$  about  $30^\circ\text{C}$  below  $T_{NI}$ . The order parameter is about 0.75 when the interference figures in conoscopy are lost. Point defects developed near either bounding surface as the temperature reached about  $30^\circ\text{C}$  below  $T_{NI}$ , propagating to the interior of the sample as the temperature was further lowered. At the earliest stage, the defects disappeared if the temperature was slowly reduced. When viewed between crossed polars with either the polarizer (P) or the analyzer (A) aligned with  $\bar{n}$ , the defects appear as a dark cross along P and A, with bright lobes at  $\pi/4$ , etc. Rotation of the crossed polarizer/analyzer with respect to  $\bar{n}$  does not result in a corresponding rotation of the dark interference cross, but rather, a more complex behavior, showing that the interference cross is not produced by a radially symmetric director field distortion. When viewed without an analyzer, with P perpendicular to  $\bar{n}$ , the defects

appears as rings with the interior brighter than the surroundings, and when viewed without an analyzer, with  $P$  parallel to  $\bar{n}$ , the defect appears as a ring with the interior slightly darker than the surroundings. The latter behavior is a focusing or defocusing effect with  $P$  perpendicular or parallel to  $\bar{n}$ , respectively. The director field is assumed to form a *boojum*, a bipolar droplet structure with two point defects at opposite poles<sup>17-21</sup>; the director field is postulated to adopt the symmetry of an ellipsoid of revolution, with its long axis along the undistorted director. Owing to the birefringence of PBZT, the average refractive index in the interior of the boojum is larger or smaller than that of the surroundings for  $P$  perpendicular or parallel to  $\bar{n}$ , respectively, giving the focusing and defocusing effects. The origin of the boojum structure is unclear. A network of point-defects has been studied in nematic fluids exposed to a thermal gradient,<sup>23</sup> but the effect observed here appears to have a different origin. The defects observed here seem to be positioned more or less at random (though appearing first near either surface), and their density or distribution is not affected by the deliberate imposition of a thermal gradient. The structures observed here may represent regions with lower order parameter  $S$  than the surroundings, perhaps regions with average lower chain length than that of the bulk sample. Similar effects have been reported elsewhere in phase separation in nematic systems.<sup>24,25</sup> The sample is heterodisperse in chain length, and might be expected to segregate with chain length, though such effects have been difficult to study,<sup>5</sup> perhaps owing to the high viscosity of the polymeric nematic. With increasing time, the number and size of the defects increases, and the material becomes filled with overlapping ring-like structures, and transmits light between crossed polars for any orientation of the polars, see Fig. 14.

The anisotropy near the surface as monitored by  $I_{||}/I_{\perp}$  is observed to decrease continuously as the temperature approaches  $T_{NI}$ . The sample becomes relatively bright between crossed polars about 10°C below  $T_{NI}$ , and becomes biphasic about 5°C below  $T_{NI}$ . Remarkably,  $I_{||}/I_{\perp}$  does not reduce to unity as the intensity transmitted between crossed polars vanishes, suggesting that an aligned surface layer persists to temperatures well above  $T_{NI}$ . Indeed, on cooling,  $I_{||}/I_{\perp}$  returns to its original value, showing that the surface layer acts as a template for alignment of the nematic.

**2.4 The Defect Structure During the Evolution of a Monodomain** Although the preceding describes a monodomain prepared under the influence of an external magnetic field, a monodomain will also form slowly over a period of many days even in the absence of an external magnetic field, apparently driven by surface alignment induced during the process of filling the cell.<sup>3,20,26</sup> Examples of the ratio  $I_{||}/I_{\perp}$  of the fluorescence intensities  $I_{||}$  and  $I_{\perp}$  along and perpendicular to the flow direction, respectively, are given in Fig. 15 for samples on annealing following extrusion into a parallel cell 400  $\mu\text{m}$  thick. The anisotropy near the surface detected by the fluorescence emission is small, but not zero, immediately after the flow is stopped, and increases to an intermediate plateau after about 1 hr. The increase to the final high level of anisotropy characteristic of the monodomain, and the uniformity necessary to form conoscopic interference figures was not observed until more than 70 days after the cell was filled, demonstrating the torpid approach to equilibrium. Optical effects observed in the approach to the equilibrium monodomain texture are discussed below.

In some cases, a smooth nonuniform director field may be observed, with spatial gradients in  $\bar{n}(\mathbf{r})$  everywhere weak, giving the nematic the featureless appearance of a normal isotropic fluid when viewed with natural (unpolarized) light without the use of a polarization analyzer.<sup>26</sup> When viewed between crossed polars, such a preparation does

not exhibit a sharp extinction over the entire sample area for light polarized along the optic axis (e.g., the chain axis for most rodlike molecules), and may not develop a deep extinction at all in most regions. This behavior is caused by distortions with weak spatial gradients, and is to be expected if the molecules near the surface do not have an overall global alignment. A monodomain preparation is characterized by a strong, global alignment of the chains near the boundary surfaces in a slab sample, whereas a smooth nonuniform director field is characterized by spatial fluctuations in the chain axis direction, and a resulting weak anisotropy of the fluorescence emission when averaged over macroscopic dimensions. Preparations such as these motivate the use of a generalized representation of the order parameter. It seems likely that the order parameter within a small enough region will be the same as it would be in a monodomain preparation.<sup>15,27-30</sup> Nevertheless, when averaged over the sample, the order parameter may appear to be low. It is convenient to consider a local order parameter  $S(\mathbf{r})$  defined over a volume  $V_s$  as large as possible, but small enough that the value of  $S(\mathbf{r})$  does not depend appreciably on  $V_s$ . Then,  $S(\mathbf{r})$  is expected to be about equal to  $S$  for a monodomain. For the smooth texture,  $V_s$  is relatively large, but has dimensions smaller than those of the macroscopic slab.

A solution of PBZT quenched rapidly from the isotropic into the nematic phase, or a sample recently subjected to rapid deformation will adopt a *mottled* appearance characterized by turbidity in natural light, and no anisotropy to the transmission between crossed polars when averaged over macroscopic dimensions.<sup>20,26</sup> The appearance between crossed polars will be of strong spatial fluctuations in the transmission, giving the impression of domains.<sup>27</sup> In this case,  $V_s$  is reduced to a volume with dimensions in the range of microns,<sup>27</sup> but presumably,  $S(\mathbf{r})$  within such regions is still about equal to  $S$  for the corresponding monodomain at the same composition and temperature, and  $\bar{\mathbf{n}}(\mathbf{r})$  is everywhere continuous, though possibly exhibiting locally strong gradients.

On annealing, the texture coarsens ( $V_s$  increases), with the appearance of *line defects* after a certain time (e.g., several hours in preparations of PBZT). Prior to the appearance of relatively sharp line defect features, the sample exhibits very diffuse features, which tend to focus or defocus light, owing to the birefringent character of the material, as discussed above in relation to the ellipsoidal defects observed on heating a monodomain. These may be visualized either using polarized light with or without an analyzer, and give the impression of hillocks and valleys in the two-dimensional projection observed in the optical microscope. If placed at this stage in an external magnetic field aligned along the extrusion direction, a texture is obtained in which the otherwise well-aligned bulk sample is filled with ellipsoidal shaped defects, see Fig. 6. Similar effects have been reported in other systems.<sup>31</sup> These may vary in size, but usually maintain a common ratio of major to minor axes for a given material. The axial ratio is probably fixed by a ratio of two of the Frank curvature elasticities. The defects appear to nearly planar, with their planes in the plane of the slab, and dichroism indicates that the director in the interior of the defect is perpendicular to that in the exterior, i.e., orthogonal to the applied magnetic field. Interference fringes appear parallel to the ellipsoidal defect loop when viewed between crossed polars, Fig. 16. Although these are enhanced using monochromatic radiation, they are also observed in white light, suggesting that they occur due to effects confined to a thin plane in the sample. Their appearance suggests that the loops are 1/2 twist defects, with the twist occurring over a short distance close to the plane of the defect, rather than over the entire sample thickness as usually assumed in theoretical representations.<sup>32-34</sup> Frequently, a sharper line defect is observed emanating from the ellipsoidal feature, see Fig. 16 (see below). These defects will persist for an extended period, with smaller defects ( $\approx 10 \mu\text{m}$  major axis or smaller) persisting for several

months or longer. Smaller defects tend to slowly migrate to one end of the tube and disappear if the sample is held in an external magnetic field aligned along  $\bar{n}$ ; presumably they move in the direction of lowest order in the developing monodomain. The proposed 1/2-twist-loop corresponds to a molecular orientation in the interior of the loop that is orthogonal to that in the bulk of the sample. This could occur if a region in the partially annealed nematic were trapped in that orientation on imposition of the field, and unable to reorient on the time scale of the reorientation of other regions with a stronger interaction with the external magnetic field. The chains in the trapped region could reduce their unfavorable interaction with the external magnetic field by rotation of the planes of the repeat unit into the plane of the slab, but that rotational state probably relaxes rapidly on removal of the external field, leaving only the orientation of the molecular axis in the interior of the twist-loop orthogonal that in the bulk. Large, interconnected loops may be reduced to similar ellipsoidal defects in an external magnetic field, with the planar ellipsoidal feature accompanied by sharp loops emanating from one or both of the ends of the ellipsoid; these may be the remnant of loops connected to the principal loop that survived as the ellipsoidal defect.

With additional annealing time in the absence of an external magnetic field, the diffuse features mentioned above sharpen into more line-like defects, initially strongly entwined and filling the sample. In the final stage of the evolution of a monodomain of a nematic solution of PBZT from a mottled texture under the action of an aligned surface, loop defects are observed only near (but not usually at) either boundary surface in a slab geometry between glass plates (slab thicknesses of 100-500  $\mu\text{m}$  have been used). At this stage, the nematic in most of the slab is free of texture, and is strongly birefringent and dichroic in white light, with maximum absorption along extrusion axis, and extinction along and perpendicular to that axis, though it will usually not yet present well-formed conoscopic interference figures. In the simplest case, the defects may appear as simple loops, often elongated, but more complex shapes are also common, see below. When viewed between crossed polars in monochromatic radiation at  $\pm \pi/4$  to the extinction direction, the sample reveals a complex pattern of mostly aperiodic broad fringes superposed on the loop defects, see below. Adjacent bright and dark fringes correspond to a change in the retardation  $\delta$  by 1/2 for light propagating orthogonal to the slab. Conoscopic interference figures (usually distorted) begin to appear when the separation between fringes is larger than the diameter of the field of view in conoscopy.

The typical appearance of the simple loop defects observed with nematic solutions of PBZT is summarized schematically in Fig. 17. Some of the principal features may be observed in polarized light without the aid of an analyzer, indicating that they arise from scattering and/or refraction. Dichroism observed with white light does not reveal any twist to the orientations in the interior and exterior of the loop (unlike the twist-loops prepared in a magnetic field discussed above). This could mean either that there is no twist, that there is a twist that is a multiple of  $\pi$ , or that very slow twisting occurs from one surface to the other, giving the light a polarization controlled by the polarizability of the nematic near the surface from which the light emerges, and obscuring any internal twist.<sup>22</sup> When viewed in white light, the loop defects exhibit a complex optical pattern: a black loop observed with P either parallel or perpendicular to  $\bar{n}$  (the director in the bulk nematic), and a bright loop-like image, the position of which shifts with respect to the black loop as P is varied from parallel to perpendicular to  $\bar{n}$  (the position of the black loop tends to be invariant). The contrast of the loop structure is minimal with P placed  $\pm \pi/4$  to  $\bar{n}$ , and strong for other angles, including angles only slightly removed from  $\pm \pi/4$ , see Fig. 17; the color tends to modulate along the loop with P placed  $\pm \pi/4$  to  $\bar{n}$ . These

features are more sharply revealed with monochromatic radiation. As shown in Fig. 17, interference patterns are observed near the defect with P placed  $\pm \pi/4$  to  $\bar{n}$  using monochromatic radiation, and the intensity alternates from dark to bright around the loop. In addition, the background is observed to be distorted through the appearance of broad interference fringes, but these do not suggest a large difference in the retardation on the interior and exterior of the loop. The loop is embedded in a director field that is too misaligned to exhibit symmetric conoscopic interference figures in the nearby region. These features are consistent in a general way with the properties calculated<sup>29-32</sup> for a twist loop with  $s = 1/2$  located in a plane close a wall if it is assumed that the twist occurs over a distance large compared to the wavelength of the light used to study the texture (the calculations are limited to the case with  $\bar{n}(\mathbf{r})$  in the plane of the slab, which is not a reasonable constraint with the materials studied here). The distortion of the local director will result in rotation of the plane of polarization of the propagating rays and diffract them in complex ways, leading to the appearance of the black loop along the locus of the twist defect when viewed in parallel polars with P parallel or perpendicular to  $\bar{n}$  owing to scattering within the core, and a focused bright image arising from refraction and rotation of plane of polarization of light viewed between crossed polars with P parallel or perpendicular to  $\bar{n}$ .<sup>32</sup> If placed in a magnetic field aligned along  $\bar{n}$ , the loops first become distorted, elongated along the field, and then are reduced to an elliptically shape, with most of the twist confined to a nearly planar region marked by an elliptically shaped line defect.

Similar optical observations on line defects in nematic solutions of a thermotropic copolyesteramide have been discussed in terms of twist disclination defects in a biaxial nematic structure.<sup>35</sup> Although PBZT could certainly exhibit biaxial behavior, it may not be necessary to invoke this in interpreting the optical observations.

An example of a complex loop shape and its relaxation is shown in Fig. 18 as a function of time during the annealing; although the defect forms a continuous loop, it was too large to be photographed in one piece until well into the annealing process. For convenience of contrast, the bright image observed between crossed polars is shown in Fig. 18. The black core was always close to the bright image. Schematic drawings of the loop are provided to aid the reader. In the earliest photograph shown (Fig. 18a), the large loop is connected to a small loop at one point, and near the right side it executes a helical twist, crossing over itself. That conclusion cannot be made on the basis of Fig. 18a, but can be deduced on the basis of the subsequent photographs. Thus, the images show that the loop simplifies by removing the helical twist along its contour to become more planar, continually diminishing in size. Further, the loop-like piece placed across the larger loop is observed to shrink, with one side crossing over (under) the larger loop in the process. A schematic drawing of the loop is provided to aid the reader. The loop-defect eventually disappeared completely, becoming elongated in along the optic axis of the nematic in the process.

As discussed in the preceding, with continued annealing, the line defects will disappear as the texture coarsens to a monodomain. For example, a line defect such as that shown in Fig. 19 will continuously decrease in length with increasing time in the late stages of the annealing. Thus, in a scaling analysis, the radius  $r$  of a free twist loop is expected to decrease with annealing time as<sup>36-38</sup>

$$r(t) \propto (t_0 - t)^{1/2} \quad (16)$$

where  $t_0$  is the time at which the loop vanishes—the analysis assumes that the collapse is

controlled by a single viscosity and a single Frank elasticity. Data on circular loop defects in a small molecule nematogen were observed to follow this prediction, with the loop disappearing within a few seconds ( $t_0 < 10$  s).<sup>37,38</sup> As illustrated in the preceding, twist-loop defects often exhibit a complex, noncircular shape in solutions of PBZT, and the time to disappearance is long ( $t_0 \approx 10^6$  s). Nevertheless, with time, the loops usually tend to become more circular, with the maximal extension of the loop decreasing at a faster rate than its minimal dimension to achieve this shape, e.g., see Fig. 19. A plot of the average  $\langle D(t) \rangle$  of the maximum and minimal extensions of a closed loop during annealing to the disappearance of the defect is shown in Fig. 20. The decay does not appear to follow a square-root time dependence, with  $\langle D(t) \rangle$  exhibiting proportionality to  $t_0 - t$  instead. This behavior is in contrast to that reported for small molecule nematogens,<sup>37,38</sup> and may be caused by the proximity of the twist loops studied here to a surface; in general, the distance of the loops from a surface is smaller than their size. The alignment at the surface may be implicated in the linear relaxation of the loop size.

In a related treatment, the density  $\rho_{\text{lin}}$  of the lines per unit volume in the defect full nematic at earlier times in the annealing is predicted to follow the evolution equation<sup>38</sup>

$$\frac{d\rho_{\text{lin}}}{dt} \propto -\rho_{\text{lin}}^2 \quad (17)$$

Reasonable agreement with this prediction has been reported for small molecule nematogens,<sup>38</sup> but the situation may be more complex with polymeric nematics owing to the disparity among the Frank curvature elasticities, etc.

## 2.5 Conclusions

The preceding describes features of texture formation and distortion of the director field in an external magnetic field for nematic solutions of a rodlike polymer. Many of these features appear to be qualitatively similar to behavior reported for small molecule nematogens, and for recently reported behavior on thermotropic polymer nematics.<sup>39</sup> Currently available theoretical treatments appear to provide some guidance in understanding the observed behavior, but the description remains incomplete, especially with regard to shear flow.

With respect to the apparently defect-free monodomain used for the NLO experiments in the preceding chapter, the results here show that the director field must be essentially uniaxial in order to observe the conoscopic interference figures; distortions around line defects destroy the phase coherence required to form such figures. Further, the bipolar structures (*boojums*) observed on warming to within 20°C of the clearing temperature do not have the properties to give the unexpected NLO behavior. Consequently, the trilayer model proposed to describe that behavior remains the most plausible explanation available given the symmetry of the nematic phase.

scattering photometer described elsewhere<sup>2</sup> was used, with incident light with wavelength 647.5 nm from an krypton-ion laser.

Electronic absorption spectra were obtained using a Hewlett-Packard Spectrometer (model 8451A), equipped with a photo-diode array detector to permit measurement of a spectrum within 5 s. Samples were placed in a sealed cell and cooled by immersion in an isopropanol bath. After being held at a low temperature for the desired time, the cell was transferred to the spectrometer, and spectra were measured as the cell slowly warmed ( $\approx 2^\circ\text{C}/\text{m}$ ) to room temperature; residual isopropanol on the cell surface served to suppress fogging of the cell face by moisture condensation.

The differential refractometer on a Waters Size Exclusion Chromatograph was used to determine the refractive index increment  $\partial n/\partial c$ , bypassing all columns, so that samples were fed directly into the refractometer cell. Standardized volumes (20  $\mu\text{L}$ ) of solutions of polystyrene with known concentration were injected into the refractometer to determine the proportionality constant  $k = \Delta n/\Delta V_{\text{instr}}$ , where  $\Delta V_{\text{instr}}$  is the integrated instrument response under the elution peak, and  $\Delta n$  is calculated from the concentration and  $\partial n/\partial c$  of the polystyrene solution ( $\partial n/\partial c = 0.198 \text{ mL/g}$  in THF).<sup>58</sup> In subsequent determinations of  $\partial n/\partial c$  for solutions of PDTP,  $\Delta n$  was calculated from measurements of  $\Delta V_{\text{instr}}$  as  $\Delta n = k\Delta V_{\text{instr}}$  for solutions of known  $c$  and standard injection volume.

**3.2.2 Data Analysis** Light scattering results are analyzed according to the model for anisotropic scatterers.<sup>2,59-66</sup> This model provides equations for the dependence of vertical and horizontal components of light scattered with vertically polarized incident light, denoted  $R_{VV}(q,c)$  and  $R_{HV}(q,c)$ , respectively, on the modulus  $q = (4\pi n_s/\lambda) \sin(\vartheta/2)$  of scattering angle vector, where  $n_s$  is the refractive index of the sample,  $\lambda$  is the wavelength of light, and  $\vartheta$  is the angle between the incident and scattered beams. The polarized scattering  $R_{VV}(0,c)$  extrapolated to zero scattering angle provides information on the molecular weight  $M$  and the second virial coefficient  $A_2$ :

$$\left(\frac{Kc}{R_{VV}(0,c)}\right)^{1/2} = \left(\frac{1}{M(1+4\delta^2/5)}\right)^{1/2} \left\{1 + \left(\frac{1-\delta^2/10}{1+4\delta^2/5}\right)A_2Mc + \dots\right\} \quad (18)$$

where  $K = (2\pi^2/N_A\lambda^4)[n_0(dn/dc)]^2$ ,  $n_0$  is the solvent refractive index,  $N_A$  is Avogadro's number and  $\delta$  the molecular anisotropy of the chain. The latter is a function of the chain conformation and the intrinsic anisotropy  $\delta_0$  of the scattering elements making up the chain, see below.

When extrapolated to infinite dilution (denoted by a super zero), the angular dependence of the scattering provides a measure of the root-mean-square radius of gyration  $R_G$ .<sup>62-65</sup>

$$\left(\frac{Kc}{R_{VV}(q,c)}\right)^0 = \frac{1}{M(1+4\delta^2/5)} \left\{1 + \frac{1}{3}(R_{G,V}q)^2 + \dots\right\} \quad (19)$$

with  $R_{G,V}^2 = J(\delta)R_G^2$ , where

$$J(\delta) = \frac{j(\delta)}{1+4\delta^2/5} = \frac{1-4f_1\delta/5+4(f_2\delta)^2/7}{1+4\delta^2/5} \quad (20)$$

26

### 3. Association of a Poly(*n*-alkyl thiophene) in Dilute Solution

#### 3.1 Introduction

Polythiophenes are of interest for potential novel optical and electronic behavior owing to the electronic delocalization in the thiophene rings; rodlike conformations have been proposed as a source of extended delocalization, with resultant enhanced electronic and optical behavior.<sup>40</sup> In this study, static and dynamic light scattering measurements were undertaken on samples of poly(*n*-dodecyl thiophene), PDTP, to evaluate its conformation over a range of temperature, and to learn whether a reversible thermochromic effect is associated with any conformational change. In the thermochromic effect the color of dilute (or concentrated) solutions changes reversibly over a narrow range of temperature.<sup>40-42</sup> Samples of a PDTP provided by R. D. McCullough, Carnegie Mellon University, were used in the study. This material is prepared by a novel synthesis that provides a high specificity of head-to-tail configuration of the repeat units (>95% H-T addition).<sup>42</sup> In older polymerizations the head-to-tail configuration is mixed with substantial fractions of head-to-head and tail-to-tail configurations. The regularity of the head-to-tail addition is expected to improve packing in the solid state, and is implicated in enhanced electronic conduction<sup>42</sup> A suitable sample might also exhibit enhanced NLO behavior.

Thermochromism has been observed in a number of polymers, and has been studied by a variety of methods. Although the thermochromism is in the end related to the rotational states of a chain, the question remains as to whether any rotational transition to result in thermochromism is driven by intermolecular interactions, or is intramolecular in origin, e.g., by a coil to helix transition. Thus, intermolecular have been cited in chromic transitions in polydiacetylene<sup>43, 44, 45, 48, 49</sup> and polysilanes<sup>46</sup> and a heterocyclic polymer<sup>47</sup>, but in other work, the same effects are attributed to intramolecular effects in polydiacetylene<sup>52, 53, 54, 55, 56</sup> and polysilane<sup>51, 57</sup>. It will be found that the behavior observed here with PDTP is intermolecular in origin, driving a conformational transition that produces the thermochromism.

#### 3.2 Experimental

**3.2.1 Methods** Reagent grade chloroform and tetrahydrofuran (THF) were dried over CaH<sub>2</sub>, distilled over CaH<sub>2</sub> under vacuum, and stored over CaH<sub>2</sub> in the dark until use. Other solvents used were reagent grade, used as received. Polymers were evacuated ( $10^{-3}$ – $10^{-4}$  mm Hg) for several days at 60°C. Solutions were prepared by weighing the appropriate amount of polymer and about two-thirds of the desired solvent(s) into a centrifuge tube with a screw top cap (Teflon™ gasket), containing a Teflon™ coated stirring bar. After several days, the solution was gently agitated by occasional swirling. After the solution was apparently uniform, the remainder of the desired solvent was added, and the solution was stirred slowly with the stirring bar for an additional 1 to 2 weeks. Chloroform solutions were held at 25°C, but solutions in THF were heated to 50°C for two hours to facilitate dissolution.

Static and dynamic light scattering experiments were carried out using instruments described elsewhere.<sup>2</sup> Solutions in chloroform were filtered into light scattering cells through 0.45 micron Teflon™ filters, degassed and sealed on a vacuum line. Cells were centrifuged for 24 hours at 7000 rpm in a swinging bucket rotor. A light



THIS  
PAGE  
IS  
MISSING  
IN  
ORIGINAL  
DOCUMENT

27

Dynamic light scattering measurements were carried out to give the intensity autocorrelation function  $g^{(2)}(\tau; q, c)$  as a function of scattering angle  $q$  and correlation time  $\tau$ .<sup>64,65</sup> With a cumulant analysis,<sup>65</sup>

$$\ln [g^{(2)}(\tau; q, c) - 1]^{1/2} = -K^{(1)}(q, c) \tau + \frac{1}{2!} K^{(2)}(q, c) \tau^2 + \dots \quad (29)$$

where  $K^{(1)}(q, c)$  is the first cumulant, etc.

For the polarized scattering, the first cumulant is used to compute the mutual diffusion coefficient  $D_M(c)$  in the limit of small  $q$ :

$$\lim_{\tau \rightarrow 0} K_{VV}^{(1)}(q, c) = D_M(c) q^2 \quad (30)$$

Data on  $D_M(c)$  are often linear in  $c$  for low  $c$ :<sup>64,65</sup>

$$D_M(c) = D_T \{1 + (k_1 A_2 M - k_2 [\eta])c + \dots\} \quad (31)$$

where  $D_T$  is the translational diffusion constant and  $k_1$  and  $k_2$  are constants of order unity. It is convenient to define a hydrodynamic scaling length  $a_{LS}(c)$  by the expression<sup>65,66</sup>

$$a_{LS}(c) = \frac{kT}{6\pi\eta_s D_M(c)} \quad (32)$$

with  $\eta_s$  the solvent viscosity;  $a_{LS}(c)$  reduces to the hydrodynamic radius  $R_H = kT/6\pi\eta_s D_T$  at infinite dilution. For samples heterodisperse an appropriate average must be used for the derived parameters, e.g.,<sup>64,65</sup>

$$R_{H,LS} = M_w / \sum w_v M_v (R_H^{-1})_v \quad (33)$$

For depolarized scattering, the first cumulant is related to rotational dynamics, as well as the translational dynamics that dominate the polarized scattering. Thus, at infinite dilution,<sup>65</sup>

$$\lim_{\tau \rightarrow 0} K_{HV}^{(1)}(q, c) = 6D_R + D_T q^2 \quad (34)$$

In general, the concentration dependence of the depolarized scattering will be small.

### 3.3 Results

The electronic absorption spectra for a sample of PDTP in chloroform over a range of temperatures is given in Fig. 20. A reversible thermochromic effect is seen, with an isobestic point for  $\lambda \approx 465$  nm. The spectra may be considered to be the sum of two components, with relative concentrations that vary smoothly with temperature.

The refractometry measurements gave  $\partial n/\partial c = 0.124 \text{ mL/g}$  for PDTP in THF, the solvent used on the SEC. Use of the Dale–Gladstone approximation  $\partial n/\partial c \approx (n_p - n_s)/\rho$  gives  $\partial n/\partial c = 0.083 \pm 0.004$  in chloroform for the density  $\rho$  of PDTP equal to  $1.0 \pm 0.1 \text{ g/mL}$ .

Several thermal histories were utilized in the study, both to characterize the solution under conditions for the thermochromic effect, and in an attempt to obtain a state free of association. Five different histories may be distinguished, differing in the thermal history following dethawing to room temperature from the rapidly frozen state used in the degassing:

History	T <sub>1</sub> (°C)	T <sub>2</sub> (°C)	T <sub>3</sub> (°C)	T <sub>4</sub> (°C)	Measurement Temperature
A	25	...	...	...	25
B	25	65	...	...	25
C	25	T <sub>q1</sub> < 0	65	...	25
D	25	T <sub>q1</sub> < 0	65	T <sub>q2</sub> < 0	T <sub>q2</sub> < 0
E	25	T <sub>q1</sub> < 0	65	T <sub>q2</sub> < 0	65
F	25	T <sub>q1</sub> < 0	65	T <sub>q2</sub> < 0	25

As shown in Fig. 21, the functions  $Kc/R_{Vv}(q,c)$  versus  $\sin^2(\vartheta/2)$  generally were not linear and not parallel over the concentration range studied for samples with history A. The data at the lowest concentration studied, 0.5 g/L (history B), show typical behavior for a solution with a small fraction of a large aggregated species mixed with unassociated, or very weakly associated chains.<sup>47,66</sup> The data for  $q$  greater than some value  $q_m$  corresponding to linear behavior at the higher angles ( $\sin^2(\vartheta/2) > 0.5$ ) may be analyzed to give apparent values  $M_{app}$  and  $(R_{G,v}^2)_{app}$  of the molecular weight and root-mean-square radius of gyration, respectively, on the assumption that the large species contain a negligible fraction of the mass:

$$M_{app} = \{Kc/R_{Vv}(0,c)\}^{-1} \approx \frac{M_w}{1 + 2A_{2LS}M_w} \quad (35)$$

$$(R_{G,v}^2)_{app} = 3\{Kc/R_{Vv}(0,c)\}^{-1} \left( \frac{\partial Kc/R_{Vv}(q,c)}{\partial q^2} \right) \approx \frac{R_{GLS}^2}{1 + 2A_{2LS}M_w} \quad (36)$$

Based on the higher angle data,  $M_{app} \approx 95,000$  and  $(R_{G,v}^2)_{app} \approx 18 \text{ nm}$  for the solution with  $c = 0.5 \text{ g/L}$ . By contrast, for the data with  $c = 1.97 \text{ g/L}$ , as shown in Fig. 21, appreciable depolarized scattering was observed for this system, revealing the presence of orientational order in the scattering species. The polarized scattering gave  $M_{app} \approx 4.5 \times 10^6$  and  $(R_{G,v}^2)_{app} \approx 56 \text{ nm}$ , and the depolarized scattering gives  $(R_{G,v}^2)_{app} \approx 67 \text{ nm}$ . The depolarized scattering was sufficiently intense to permit dynamic scattering, with the result given in Fig 22. As may be seen, the first cumulant is linear in  $q^2$ , with a positive value at zero scattering angle. Analysis with Eq. 34 gives  $D_R \approx 150 \text{ s}^{-1}$  and  $D_T \approx 8.55 \times 10^{-8} \text{ cm}^2/\text{s}$ .

As shown in Fig. 23, the scattering behavior is markedly dependent on temperature, with heating to 65°C tending to loosen the structure observed on cooling to 25°C (history C). Further, as shown by the data on the sample with  $c = 3.0 \text{ g/L}$  in Fig. 23, annealing at a low temperature for a prolonged period changes the structure with increased association, even on heating to 65°C (history E) for the polarized scattering, with the results  $M_{app} \approx 10^6$  and  $(R_{G,v}^2)_{app} \approx 170 \text{ nm}$ ; the depolarized scattering was weak. Polarized

dynamic scattering was studied for this solution gave the results in Fig. 22, with  $a_{LS}(c) = 33$  nm.

The solution with  $c = 3.0$  g/L was studied in more detail with thermal history D. As shown in Figs. 24 and 25, both the polarized and depolarized scattering changed slowly on annealing at  $-16.5^\circ\text{C}$ , with measurement at  $-16.5^\circ\text{C}$ . The change of the depolarized scattering at  $45^\circ$  scattering angle is compared with the change in the transmission  $T(t)$  for  $\lambda = 647.5$  nm as a function of time at the same temperature in Fig. 26. Values of  $M_{app}$  and  $(R_{G,V})_{app}$  are given in Fig. 27 along with data on the ratio  $[R_{H,V}(0,c)/c]^0/[R_{V,V}(0,c)/c]^0$  of the reduced intensities at zero scattering angle and the ratio  $(R_{G,V}^2)_{LS}/(M_V)_{LS}$ .

### 3.4 Discussion

The light scattering data on dilute solutions of PDTP exhibit association under all conditions studied. The results suggest an ordered, asymmetric supramolecular structure. The data on the solution with  $c = 1.97$  g/L was studied in more detail with thermal history A are of particular interest since both polarized and depolarized scattering measurements were possible. Following a procedure used elsewhere,<sup>70</sup> the values of  $D_R$  and  $D_T$  were interpreted by use of an ellipsoidal model, with major and minor axes  $L$  and  $\rho L$ , respectively, using the relations<sup>70</sup>

$$D_T = \frac{kT}{6\pi\eta_s L} G(\rho) \quad (37)$$

$$D_R = \frac{9}{8} \frac{D_T}{L^2} \left( \frac{(2 - \rho^2)G(\rho) - 1}{G(\rho)(1 - \rho^4)} \right) \quad (38)$$

$$G(\rho) = \ln \left( \frac{1 + (1 - \rho^2)^{1/2}}{\rho(1 - \rho^2)^{1/2}} \right) \quad (39)$$

The data on  $D_R$  and  $D_T$  give  $L \approx 50$  nm and  $\rho \approx 0.5$ , revealing a supramolecular structure, that is more prolate ellipsoidal than rodlike in this case.

The reversible thermochromism is associated with the supramolecular structure revealed by the light scattering data. The absorption peak at longer wavelength in Fig. 20 is attributed to a  $\pi-\pi^*$  electron transition.<sup>40</sup> Extended chain conformers are presumed to favor the longer wavelength absorption, consistent with the observation of ordered, extended supramolecular structure observed in the light scattering study under conditions favoring the long wavelength absorption. The data in Figs. 26 and 27 show that the attainment of the full thermochromic transition and the formation of the supramolecular structure tend to occur over a prolonged period, with the order increasing continuously (e.g., increasing depolarized scatter, with a tendency for  $(R_{G,V})_{app}$  and  $(R_{G,H})_{app}$  to decrease sharply, and then stabilize, whereas  $M_{app}$  increases continuously). The data in Fig. 27 show that on  $R_{G,LS}^2/M_w$  decreases continuously as the anisotropic scattering increases. With the ellipsoidal model used above,

$$R_{G,LS}^2 = \frac{L^2}{4} \frac{1 + 2\rho^2}{3} \quad (40)$$

the supramolecular structure changes shape with increasing time, becoming more elongated, with decreasing  $R_{\text{GLS}}^2/M_w$ .

The scattering profile observed for the solution with 3.0 g/L with history C exhibits an unusual upward curvature, suggesting either a sphere or a disc shaped symmetry. The parameter obtained for a spherical shape lead to a monomer concentration in the aggregate that is less than the average solution concentration. Consequently, the shape is considered to be disc-like. As shown in Fig. 27, this shape further contracts, with increasing order, on annealing at a low temperature.

The slow change in absorption at the laser wavelength (647.5 nm) over a period of 30 hours following a quench to  $-16.5^\circ\text{C}$  suggests an intermolecular mechanism, i.e. a phase separation mechanism is involved. The slow behavior essentially rules out a single chain coil-to-rod transition mechanism, since it is unlikely for a single chain event to occur over such a long period of time. Moreover, the single chain coil-to-rod transition is expected to cause a large increase in the radius of gyration, contrary to our findings of marked decrease in  $(R_{\text{G,V}})_{\text{app}}$  after being quenched to  $-16.5^\circ\text{C}$ .

The behavior can be explained using the concept embodied in a Flory phase diagram for rod-like molecules.<sup>47</sup> Although the solutions studied here were dilute, the local concentration is high in an aggregate. As the temperature is decreased, the polymer-solvent interaction parameter  $\chi$  increases. The solution corresponding to the polymer concentration in the aggregates could enter the biphasic gap and microphase separated into disordered and ordered regions. A similar behavior could obtain as solvent is lost in film casting. The formation of ordered regions makes the aggregates more compact and the segments more oriented. The large initial decrease of  $(R_{\text{G,V}})_{\text{app}}$  is consistent with the collapse of aggregates to form ordered segments in close proximity. Phase separation can be a slow process, giving the slow response observed.

The ordered phase may be the precursors of the crystalline state found by X-ray diffraction studies on films with relatively high conductivity.<sup>41</sup> The X-ray studies reveal that the thiophene rings from neighboring chains tend to stack parallel to each other with virtually uniform stacking distance of 3.8 Å. It is also found that long alkyl side chains interdigitate and form a ordered packing. It is speculated that intermolecular  $\pi$ -stacking enhance the electron transfer between chains, therefore improve conductivity; films cast from solution with more a ordered structure may result in higher conductivity or enhanced nonlinear optical behavior.

### 3.5 Conclusion

The light scattering characterization of dilute solutions of poly(*n*-dodecyl thiophene) has shown that a reversible thermochromic effect in is associated with considerable intermolecular supramolecular structure. It is proposed that the change in temperature occasions a phase transition in the moderately concentrated domains of the supramolecular aggregates, to drive the chain to an extended conformation, with the attendant change in the electronic absorption spectra. The supramolecular structure may intervene in normal film casting solution processing, with effects on the electronic and optical properties of the cast film.

#### 4. References

1. Berry, G. C., and Eisaman, P. R., *J. Polym. Sci., Polym. Phys. Ed.* **1974**, *12*,:2253 .
2. Lee, C. C., Chu, S. G., and Berry, G. C., *J. Polym. Sci., Polym. Phys. Ed.* **1983**, *21*:1573 .
3. Srinivasarao, M., and Berry, G. C., *J. Rheology* **1991**, *35*:379.
4. Onsager, L., *Ann. N. Y. Acad. Sci.* **1949**, *51*:627.
5. Flory, P. J., *Adv. Polym. Sci.* **1984**, *59*:1.
6. Mattoussi, H., Srinivasarao, M., Kaatz, P. G., and Berry, G. C., in *Optical and Electronic Properties of Polymers*, Ed. by J. M. Torkelson and J. A. Emerson, Matl. Res. Soc. Symp. Proceed. Vol. **214** (1991).
7. Mattoussi, H., Srinivasarao, M., Kaatz, P. G., and Berry, G. C., *Macromolecules* **1992**, *25*:2860.
8. Chemla, D., and Kupecek, P., *Rev. Phys. Appl. (Fr)* **1971**, *6*:31.
9. Kajzar, F., and Messier, J., *Phys. Rev. A*, **1985**, *32*:2353.
10. Kurtz, S. K., in *Quantum Electronics*, Ed. by H. Rabin and C. L. Tang, Vol. **1**, Part A, Academic Press, N. Y. (1975), Chapt. 3 and references therein.
11. Kaatz, P. G., Ph.D. Dissertation, Carnegie Mellon University (1991).
12. Born, M., and Wolfe, E., *Principles of Optics*, Pergamon Press, 6th Edition, Oxford, (U.K.) (1985).
13. Butcher P. N., and Cotter, D., *The Elements of Nonlinear Optics* Cambridge University Press, Cambridge, 1990.
14. Reinhardt, B. A., *Trends Polym. Sci.* **1993**, *1*: 4 .
15. de Gennes, P. G. *The Physics of Liquid Crystals*, Clarendon, Oxford, U. K., **1974**.
16. Chandrasekhar, S. *Liquid Crystals*, Cambridge Press, Oxford, U. K., **1977**.
17. Kléman, M. *Points, Lines and Walls*, Wiley & Sons, New York, **1983**.
18. Chandrasekhar, S., Ranganath *Adv. Physcis* **1986** *35*: 507.
19. Leslie, F. M. *Adv. Liq. Cryst.* **1979** *4*: 1.
20. Berry, G. C. *Mol. Cryst. Liq. Cryst.* **1988** *165*: 333.
21. Kléman, M. *Liq. Cryst.* **1989** *5*: 399.
22. Mauguin, Ch. *Bull. Soc. Fr. Crist.* **1911** *34*: 71.
23. Pieranski, P., Dubois-Violette, E., Guyon, E. *Phys. Rev. Lett.* **1973** *30*: 736.
24. Casagrande, C., Fabre, P., Guedeau, M. A., Veyssie, M. *Europhysics Lett.* **1987** *3*: 73.
25. Casagrande, C., Veyssie, M., Knobler, C. M. *Phys. Rev. Lett.* **1987** *58*: 2079.
26. Berry, G. C. *J. Rheol.* **1991** *35*: 943.
27. Asada, T. in *Polymer Liquid Crystals*, Ciferri, A., Krigbaum, W. R., and Meyer, R. B., Eds., Academic Press, New York, **1982**, Chapter 9.
28. Marrucci, G., Maffettone, P. L. *J. Rheol.* **1990** *34*: 1231.
29. Larson, R. G., Doi, M. *J. Rheol.* **1991** *35*: 539.
30. Marrucci, G., Greco, F. *Adv. Chem. Phys.* **1993** *86*: 331.
31. Filas, R. W. *J. Physique* **1978** *39*: 49.
32. Nehring, J. *Phys. Rev. A* **1973** *7*: 1737.
33. Meyer, R. B. *Phil. Mag.* **1973** *23*: 405.
34. Kilian, A. *Mol. Cryst. Liq. Cryst. Lett.* **1992** *8*: 91.
35. De'Neve, T., Kléman, M., Navard, P. *J. Phys. II France* **1992** *2*: 187.
36. Geurst, J. A., Spruijt, A. M. J., Gerritsma, C. J. *J. Physique* **1975** *36*: 653.
37. Chuang, I., Turok, N., Yurke, B. *Phys. Rev. Lett.* **1991** *66*: 2472.
38. Chuang, I., Yurke, B., Pargellis, A. N., Turok, N. *Phys. Rev. E* **1993** *47*: 3343.
39. De'Neve, T., Navard, P., Kléman, M. *J. Rheol.* **1993** *37*: 515.
40. Patil, A.O., Heeger, A.J., Wudl, F., *Chem. Rev.*, **1988**, *88*: 183.
41. Skotheim, T.A., Ed., *Handbook of Conducting Polymers*, Marcel Dekker, New York, **1986**.
42. McCullough, R.D., Lowe, R.D., *J. Chem. Soc. Chem. Comm.*, **1992**, 70.
43. Xu, R., Chu, B., *Macromolecules*, **1989**, *22*: 4523.
44. Li, Y., Chu, B., *Macromolecules*, **1991**, *24*: 4115.
45. Taylor, M.A., Odell, J.A., Batchelder, D.N., Campbell, A.J., *Polymer*, **1990**, *31*: 1116.
46. Shulka, P. Cotts, P.M., Miller, R.D., Russell, T.P., Smith, B.A., Wallraff, G.M., Bailer, M., Thiagarajan, P., *Macromolecules*, **1991**, *24*: 5606.
47. Wei-Berk, C. and Berry, G.C., *J. Polym. Sci., Part B: Polym. Phys.*, **1990** *28*:1873.

48. Wenz, G., Wegner, G., *Makromol. Chem. Rapid Comm.*, **1982**, 3: 231.
49. Wenz, G., Muller, M.A., Schmidt, M., Wegner, G., *Macromolecules*, **1984**, 17: 837.
50. Baughman, R.H., Bredas, J.L., Chance, R.R., Elsenbaumer, R.L., Shacklette, L.W., *Chem. Rev.*, **1982** 82: 209.
51. Rabolt, J.F., Hofer, D. Miller, R.D., Fickes, G.M., Wenz, *Macromolecules*, **1986**, 19: 611.
52. Patel, G.N., Walsh, E.K., *J. Polym. Sci., Polym. Lett. Ed.*, **1979**, 17: 203.
53. Patel, G.N., Chance, R.R., Witt, J.D., *J. Chem. Phys.*, **1979**, 70: 4387.
54. Lim, K.C., Fincher, C.R., Heeger, A.J., *Phys. Rev. Lett.*, **1983**, 50: 1934.
55. Lim, K.C., Sinclair, M., Casalnuovo, S.A., Fincher, C.R., Wudl, F., Heeger, A.J., *Mol. Cryst. Liq. Cryst.* **1984**, 105: 329.
56. Lim, K.C., Heeger, A.J., *J. Chem. Phys.*, **1983** 82: 522.
57. Harrah, L.A., Ziegler, J.H., *J. Polym. Sci., Polym. Lett. Ed.*, **1985**, 23: 209.
58. Brandrup, J., et al, Ed., *Polymer Handbook*, Third Ed., John Wiley, New York, **1989**.
59. Wong, C.-P., Ohnuma, H., Berry, G.C., *J. Polym. Sci.: Polym. Symp.*, **1978**, 65: 173
60. Metzger, P., Cotts, D.B., Berry, G.C., *J. Polym. Sci., Polym. Phys. Ed.*, **1983**, 21: 1255.
61. Berry, G.C. in *Contemporary Topics in Polymer Science*, E.M. Pearce, J.R. Schaefgen, Eds, Plenum Press, New York, 1977, p. 55.
62. Yamakawa, H. *Modern Theory of Polymer Solutions*, Harper and Row, New York, 1971.
63. Berry, G.C. *J. Polym. Sci.: Polym. Symp.*, **65**, 143 (1978).
64. Berry, G.C., in *Encyclopedia of Polymer Science and Engineering*, Vol. 8, H. Mark et al Ed., John Wiley and Sons, Inc., 1987, p. 721.
65. Berry, G.C. *Adv. Polymer Sci.*, **1994**, 114:233.
66. Furukawa, R., Berry, G.C., *Pure Appl. Chem.*, **57**, 913 (1985)
67. Cassasa, E.F., Berry, G.C., in *Comprehensive Polymer Science*, Vol. 2, G. Allen Ed., Pergamon Press, New York, 1988, Chapt. 3.
68. Berry, G.C. *J. Polym. Sci., Part B: Polym. Phys.*, **26**, 1137 (1988).
69. Berry, G.C., in *Encyclopedia of Materials Science and Engineering*, M.B. Bever Ed., Pergamon Press, Oxford, 1986, p. 3759.
70. Einaga, Y., Berry, G.C., in *Microdomains in Polymer Solutions*, Ed. P. Dubin, Plenum Publ. Co., New York, 1985, Chapt. 11.

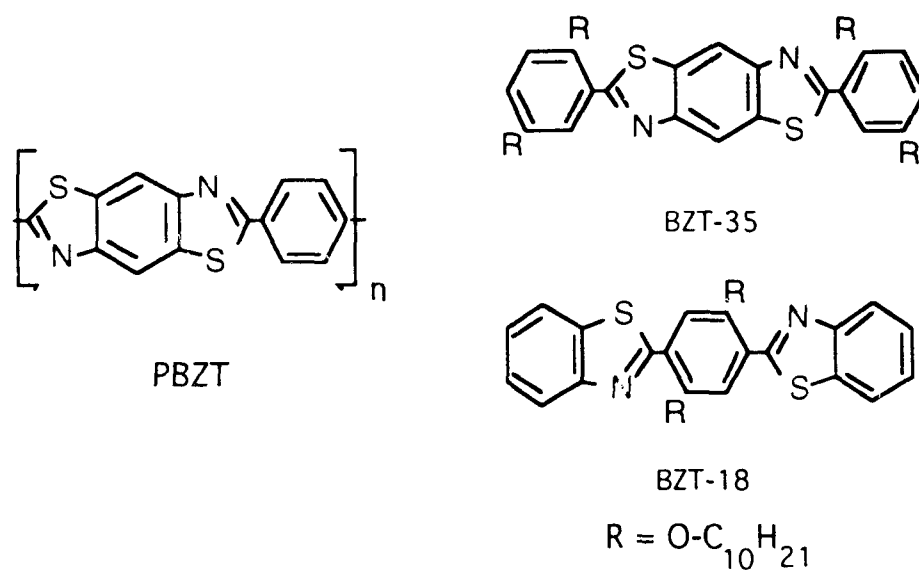


Figure 1. Structural formulae for molecules used in NLO measurements.

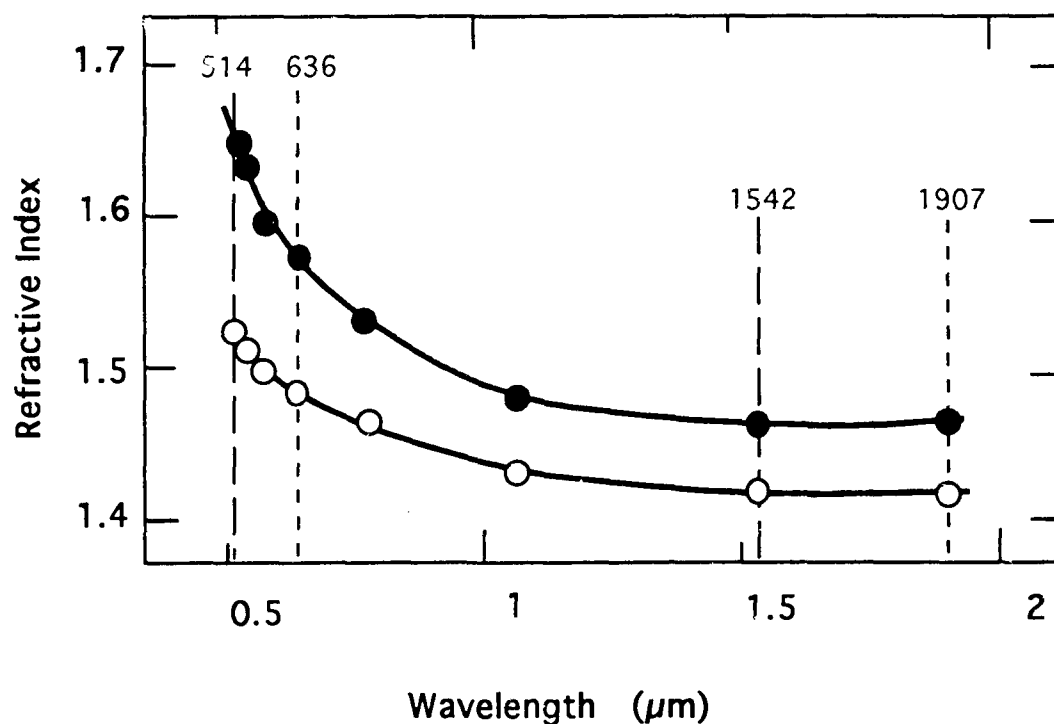


Figure 2. The extraordinary ( $n_E$ ) and ordinary ( $n_O$ ) refractive indices versus wavelength for a nematic solution of PBZT ( $\phi = 0.055$ ). The short and long dashed vertical lines show the fundamental and the THG wavelengths for fundamental wavelengths of 1.907 and 1.542  $\mu\text{m}$ , respectively.



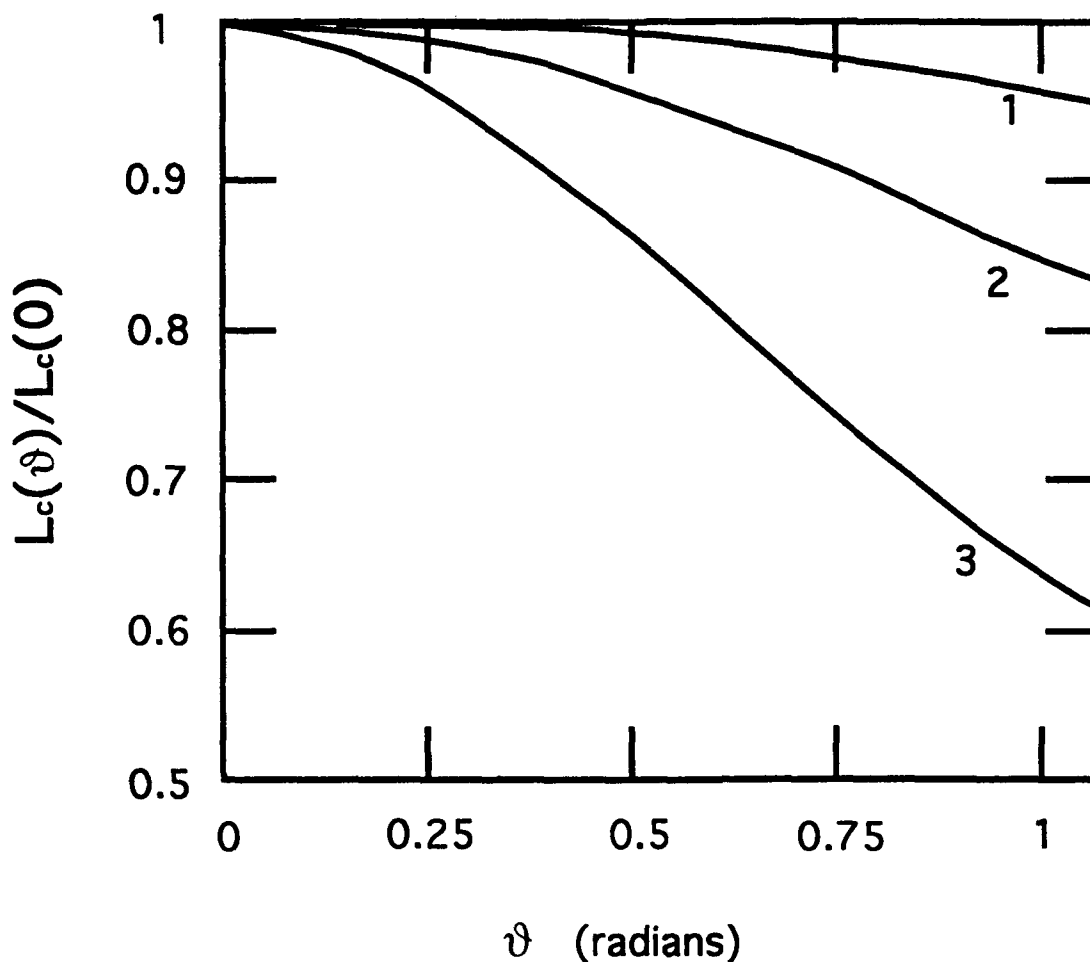


Figure 3. The reduced coherence length  $L_c(\vartheta)/L_c(0)$  versus the rotation angle  $\vartheta$  for a nematic solution of PBZT in MSA ( $\varphi = 0.055$ ; see Table 1). Curves 1 and 3 give  $[L_c(\vartheta)/L_c(0)]_{\text{HH:h}}$  and  $[L_c(\vartheta)/L_c(0)]_{\text{VH:h}}$ , respectively, and curve 2 represents  $[L_c(\vartheta)/L_c(0)]_{\text{qμ:v}}$  for the remainder of the geometrical arrangements discussed in the text (e.g.,  $[L_c(\vartheta)/L_c(0)]_{\text{HV:v}}$ , etc.); small distinctions among these for larger  $\vartheta$  are not shown in the interests of clarity.

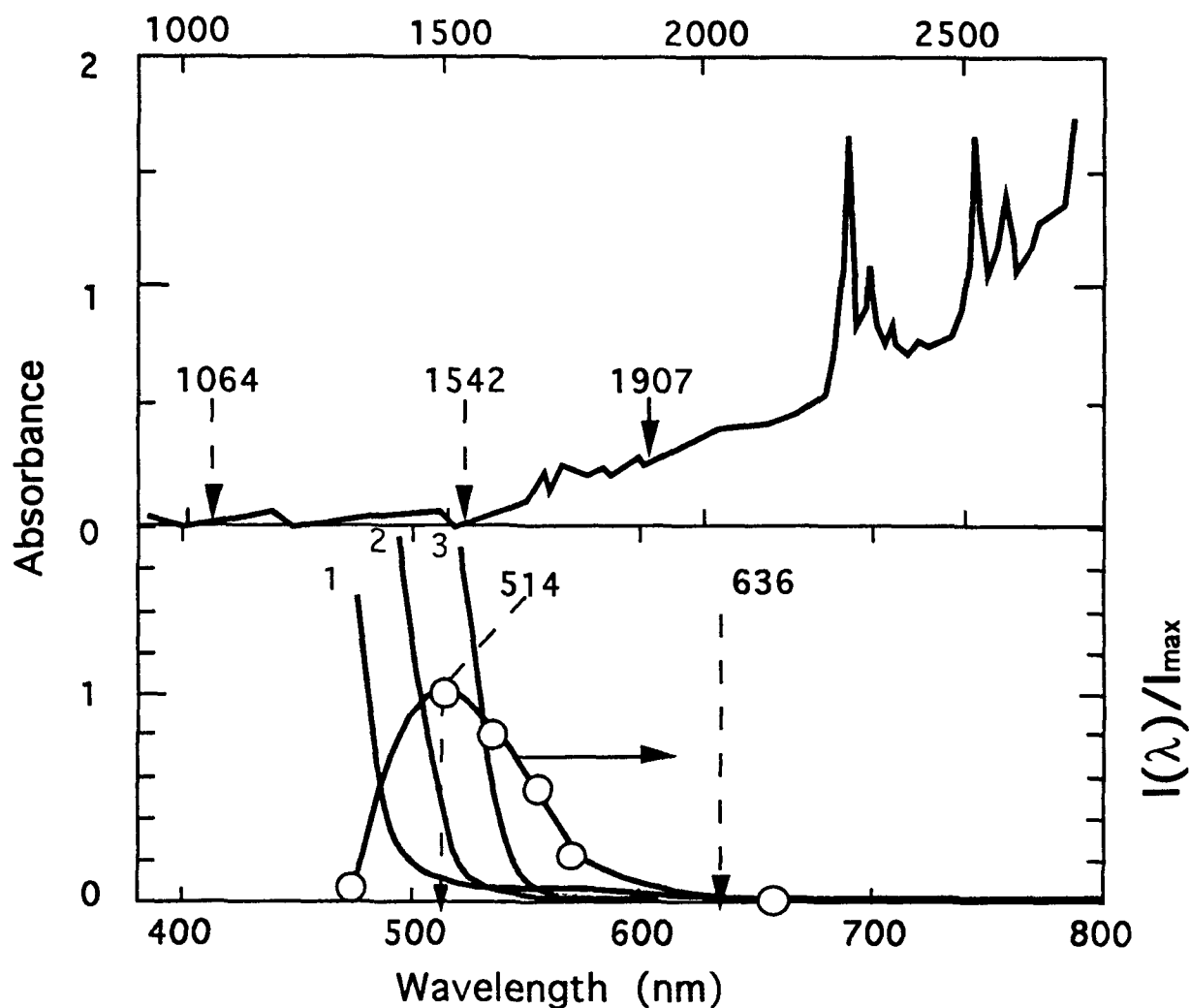


Figure 4. Upper: Absorbance versus wavelength for methane sulfonic acid solutions of PBZT ( $\varphi = 0.021$ ) in the near infra-red spectral region, for  $350 \mu\text{m}$  pathlength; the arrows show the wavelengths  $\lambda_{\omega}$  for fundamental intensities discussed in the text.

Lower: Absorbance versus wavelength for methane sulfonic acid solutions of PBZT ( $\varphi = 0.021$ ), 1; BZT-36 ( $\varphi = 0.0054$ ), 2; and BZT-18 ( $\varphi = 0.004$ ), 3; and the normalized fluorescence emission  $I(\lambda)/I_{\text{max}}$  versus wavelength for methane sulfonic acid solutions of PBZT ( $\varphi = 0.021$ ), the circles give the data, with a smooth curve to aid the reader. All for  $350 \mu\text{m}$  pathlength; the arrows show the wavelengths  $\lambda_{3\omega}$  for THG intensities discussed in the text.

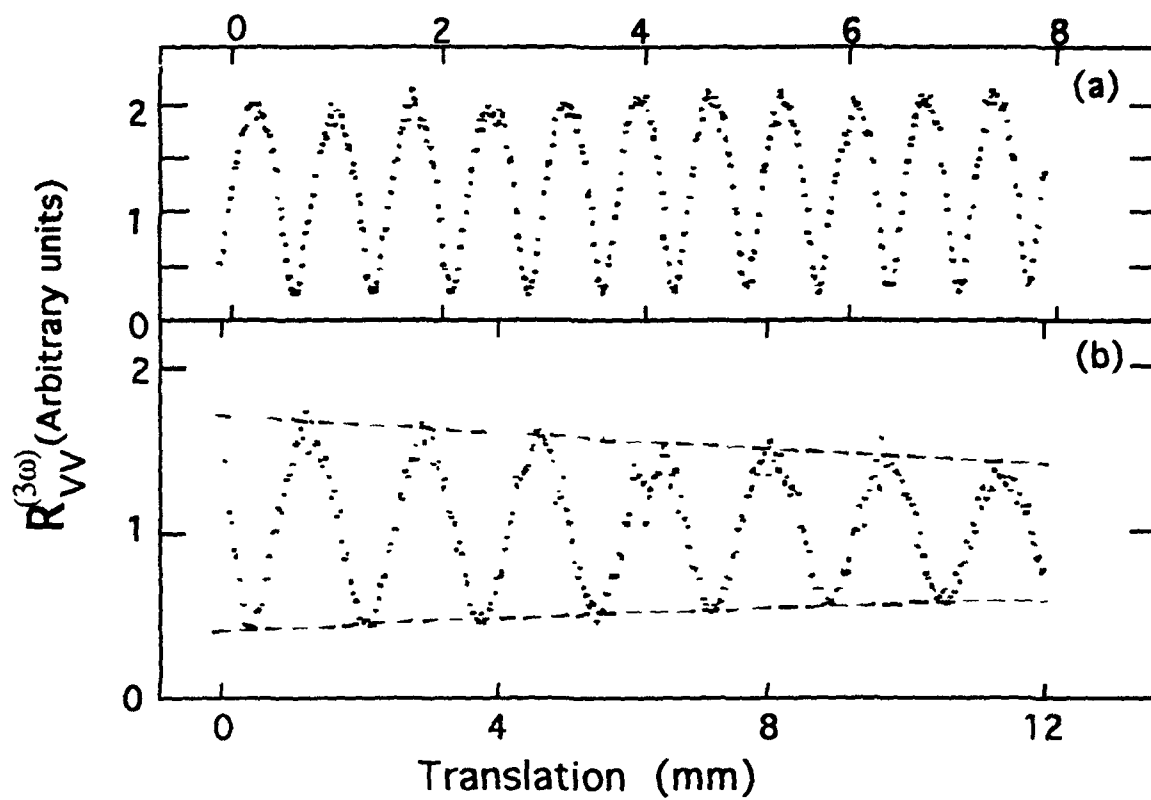


Figure 5. The third-harmonic response for an isotropic solution of PBZT ( $\varphi = 0.021$ ):  $R_{VV}^{(3\omega)}(0,L)$  versus the translation in a wedge-shaped cell ( $0.95^\circ$ ) for  $\lambda_\omega$  equal to  $1.542 \mu\text{m}$ , (a), and  $1.907 \mu\text{m}$ , (b).

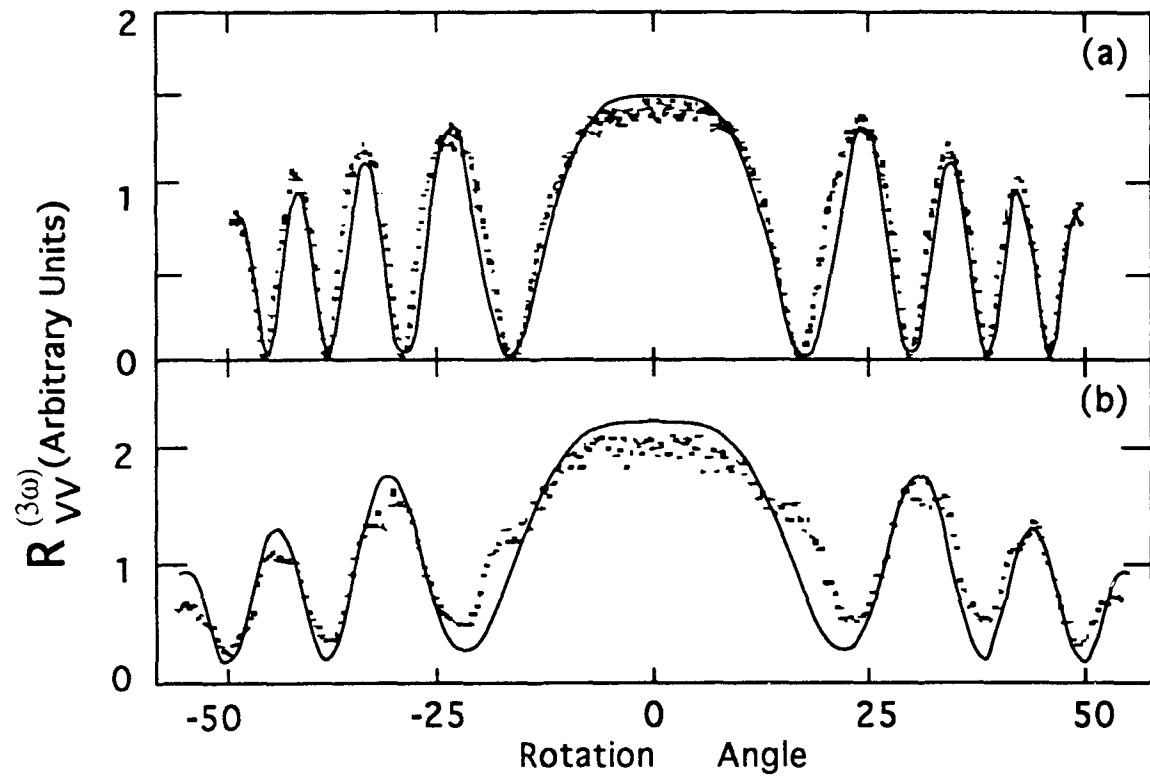


Figure 6. The third-harmonic response for an isotropic solution of PBZT ( $\phi = 0.021$ ):  $R_{VV}^{(3\omega)}(\vartheta, L)$  versus  $\vartheta$  in a rotating-slab cell ( $L = 350 \mu\text{m}$ ) for  $\lambda_{\omega}$  equal to  $1.542 \mu\text{m}$ , (a), and  $1.907 \mu\text{m}$ , (b). The solid lines were calculated as discussed in the text, using arbitrary  $L/L_c(0)$  to obtain a fit.

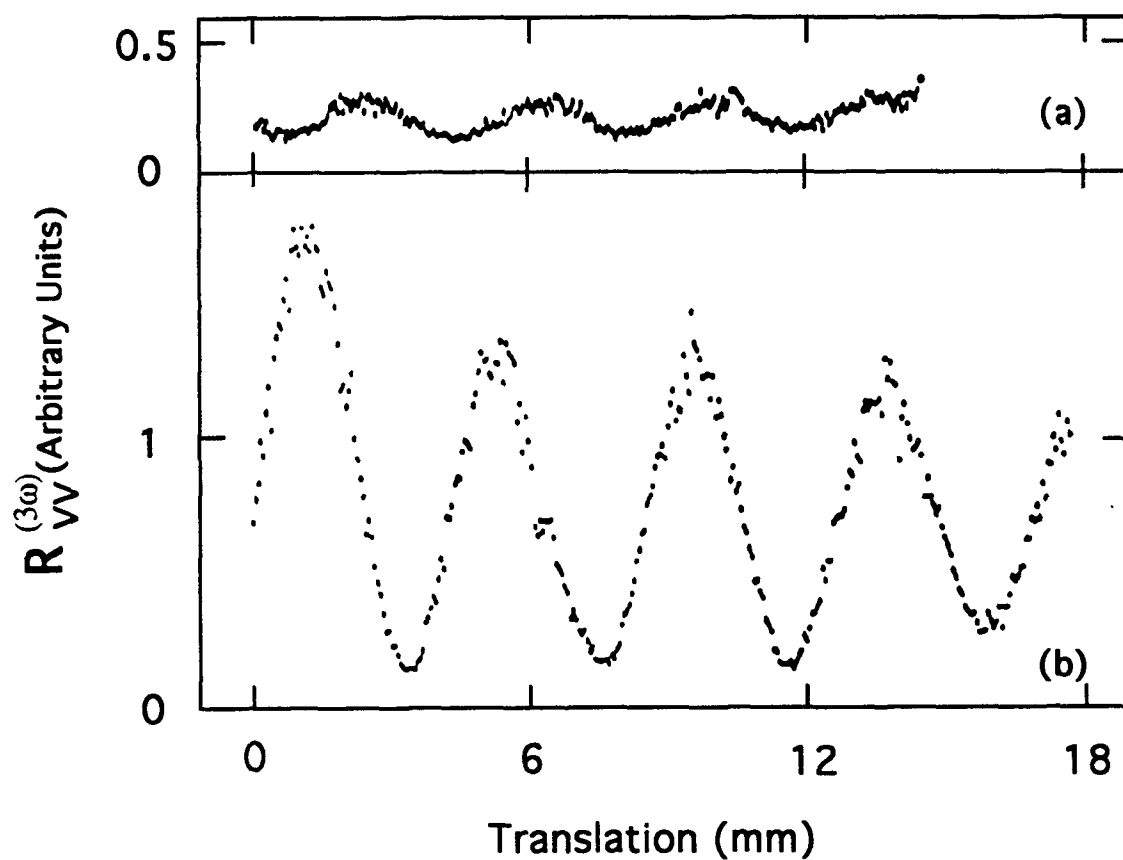


Figure 7. The third-harmonic response  $R_{VV}^{(3\omega)}(0,L)$  versus the translation in a wedge-shaped cell (0.5 deg) for solutions of (a) BZT-18 ( $\varphi = 0.004$ ) and (b) BZT-36 ( $\varphi = 0.0054$ ,  $\lambda_\omega = 1.542 \mu\text{m}$ ).

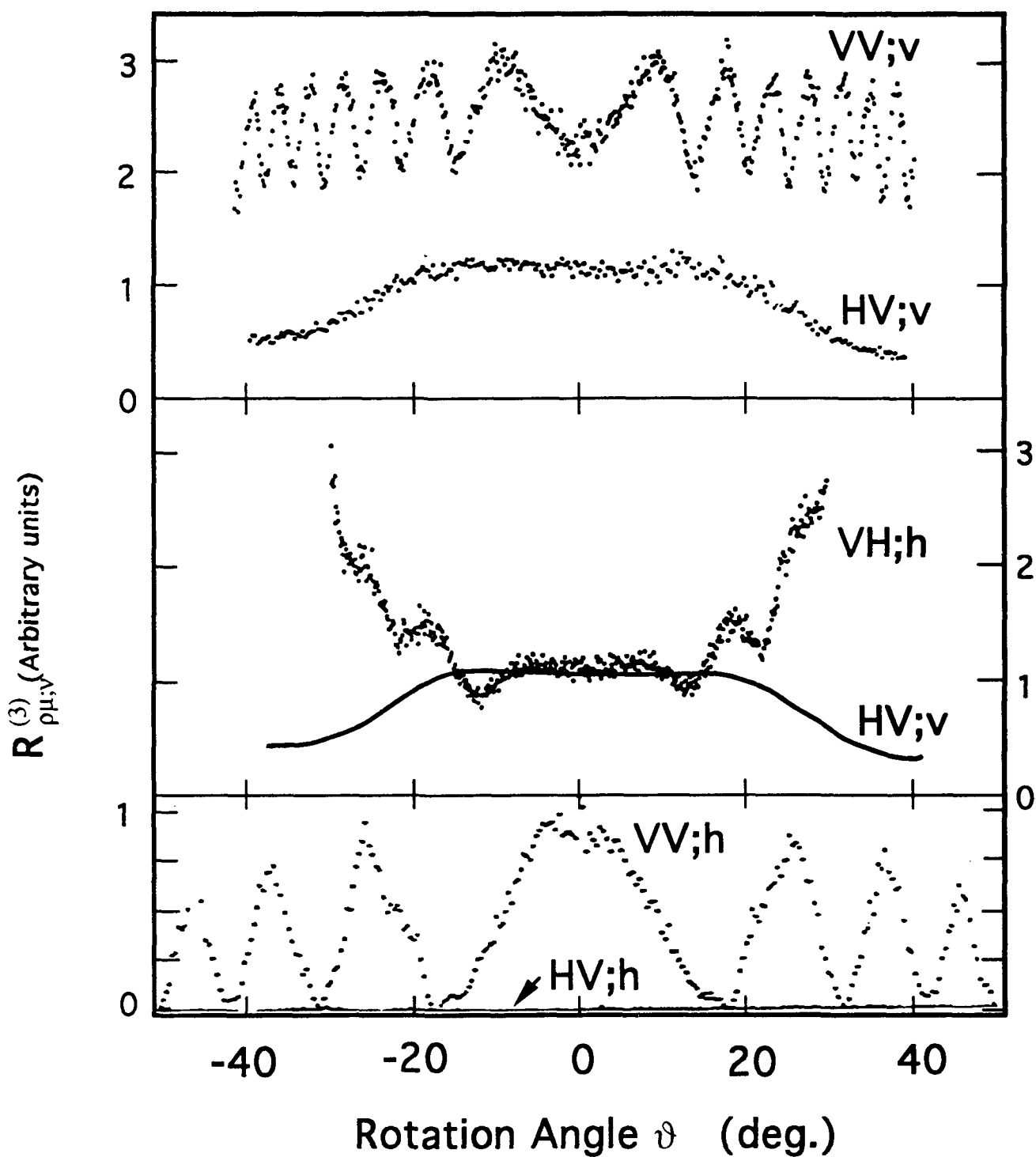


Figure 8. The third-harmonic response  $R_{\rho\mu;v}^{(3\omega)}(\vartheta, L)$  for a nematic solution of PBZT in a rotating-slab cell for the indicated orientations of the polarizations of the fundamental ( $\mu$ ) and THG waves ( $\rho$ ), and the director ( $v$ ) ( $\varphi = 0.055$ ,  $L = 350 \mu\text{m}$ ,  $\lambda_\omega = 1.542 \mu\text{m}$ ).

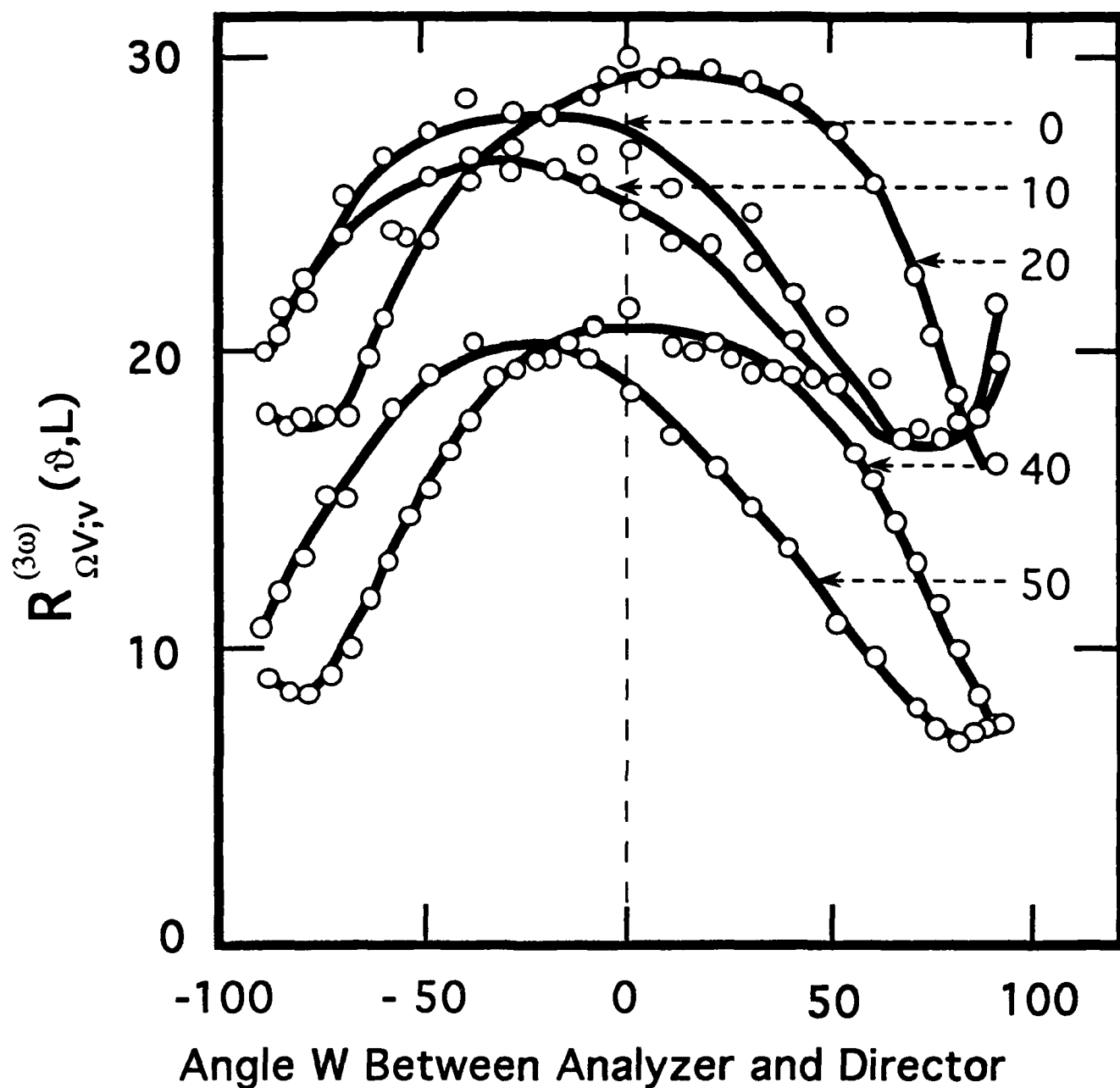


Figure 9. Relative third-harmonic generation response  $R_{\Omega V;v}^{(3\omega)}(\vartheta, L)$  for a nematic solution of PBZT in methane sulfonic acid as a function of the angle  $\Omega$  between the director and the analyzer, for several values of  $\vartheta$  ( $\varphi = 0.055$ ,  $L = 350 \mu\text{m}$ ,  $\lambda_\omega = 1.542 \mu\text{m}$ ).

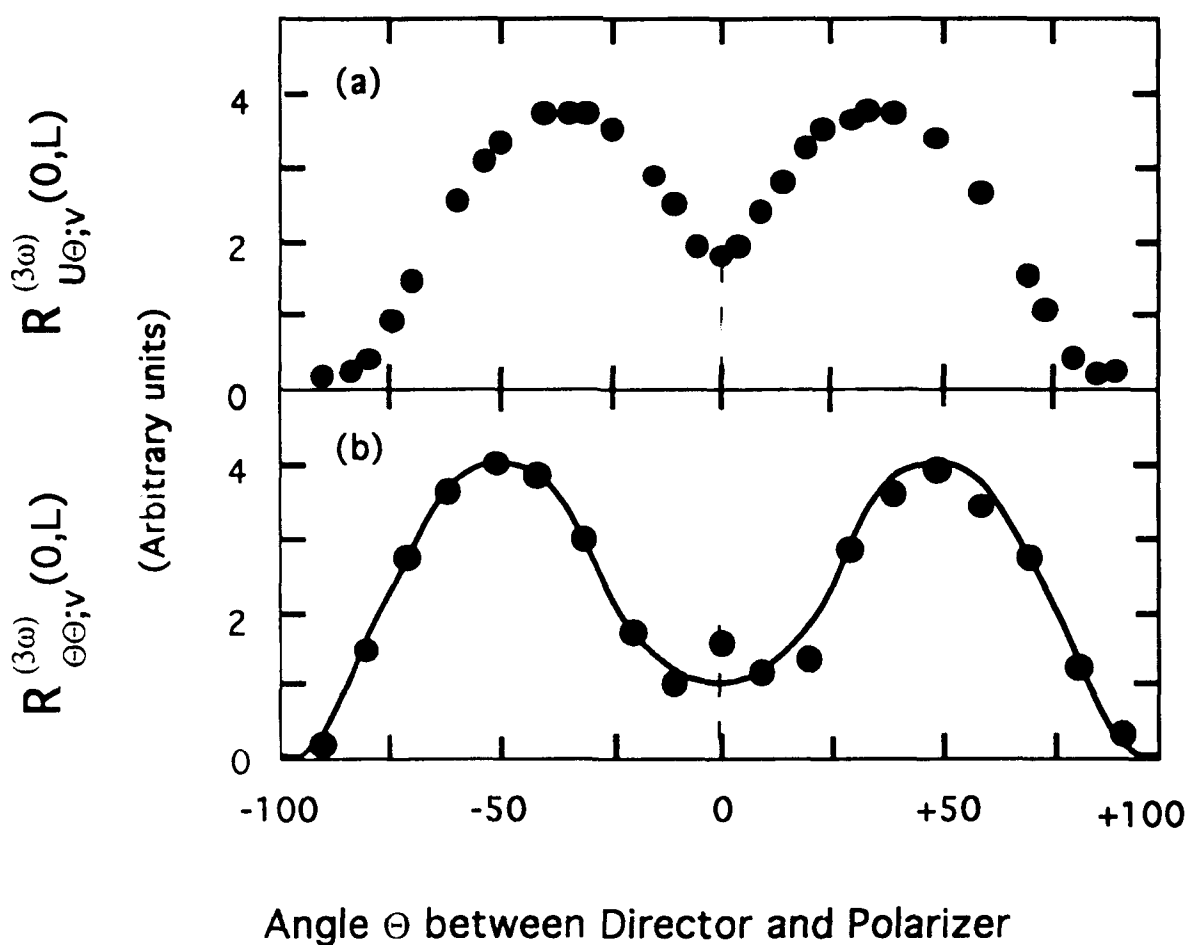


Figure 10. Relative third-harmonic generation responses  $R_{U\Theta;v}^{(3\omega)}(0,L)$  and  $R_{\Theta\Theta;v}^{(3\omega)}(0,L)$  for a nematic solution of PBZT in methane sulfonic acid as a function of the angle  $\Theta$  between the polarization of the incident wave and the vertical direction ( $\phi = 0.055$ ,  $L = 350 \mu\text{m}$ ,  $\lambda_\omega = 1.542 \mu\text{m}$ ). The upper and lower panels give  $R_{U\Theta;v}^{(3\omega)}(0,L)$  and  $R_{\Theta\Theta;v}^{(3\omega)}(0,L)$ , respectively, with no analyzer  $R_{I\Theta;v}^{(3\omega)}(0,L)$ , and with the analyzer parallel to the polarization of the incident waves for  $R_{\Theta\Theta;v}^{(3\omega)}(0,L)$ .



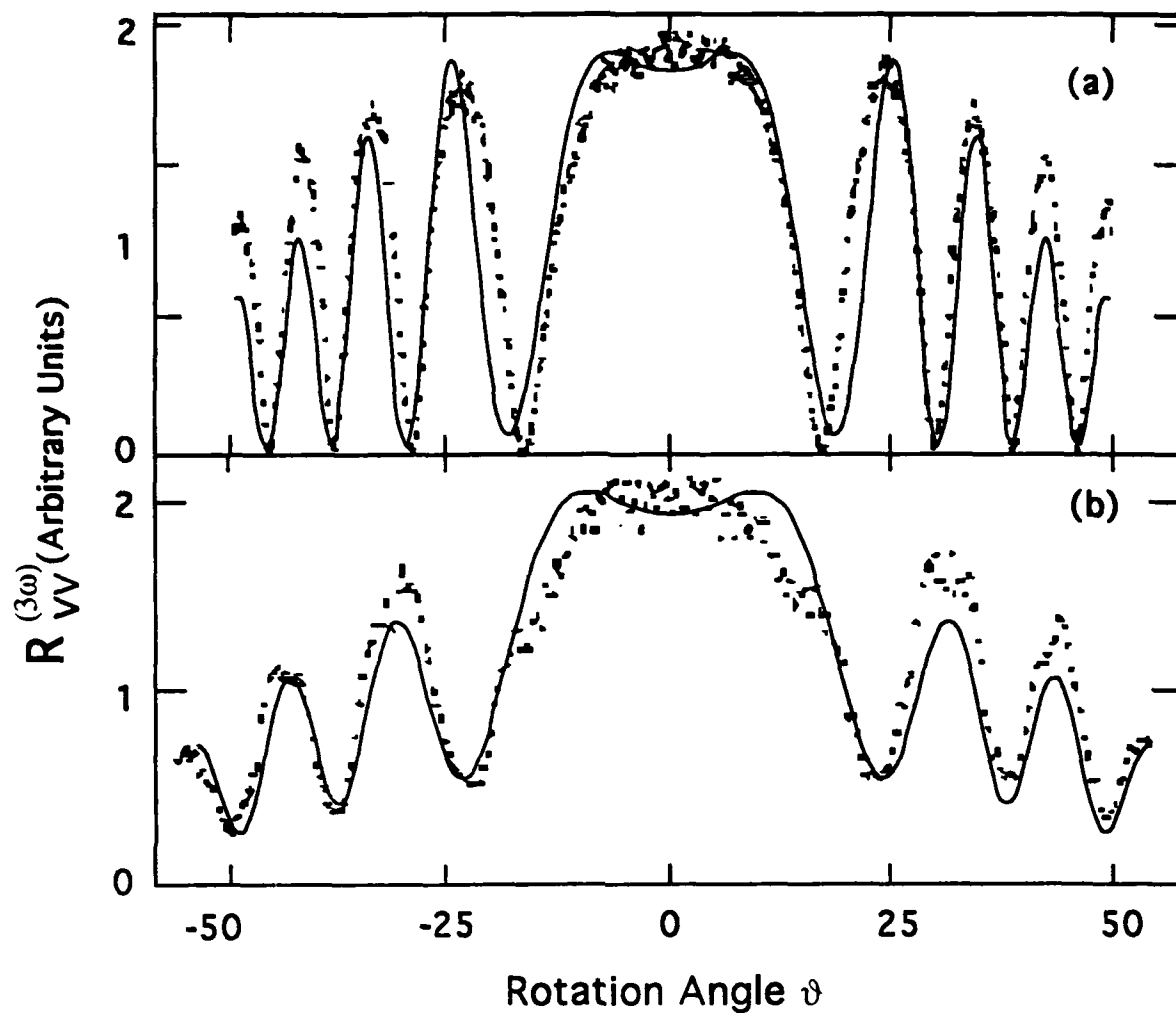


Figure 11 Comparison of observed MFP with calculations for an isotropic solution of PBZT (see Fig. 6 caption) using Eqn. 8 for a trilayer system and surface layers of  $36\text{ }\mu\text{m}$  ( $L = 350\text{ }\mu\text{m}$ ), see the text, for  $\lambda_\omega$  equal to  $1.542\text{ }\mu\text{m}$ , (a), and  $1.907\text{ }\mu\text{m}$ , (b).

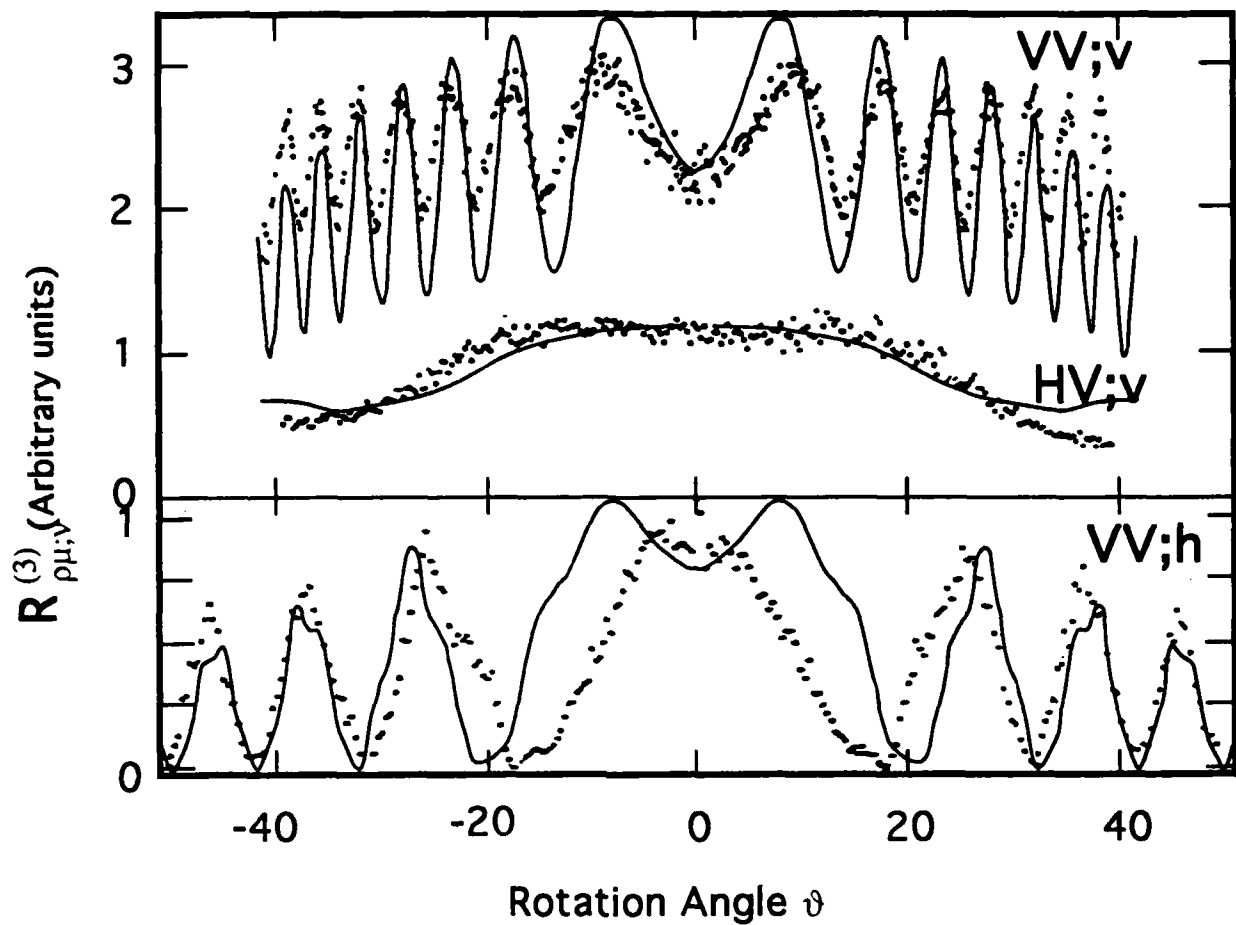


Figure 12 Comparison of observed MFP with calculations for a nematic solution of PBZT (see Fig. 9 caption) using Eqn. 8 for a trilayer system and surface layers of  $36 \mu\text{m}$ , see the text ( $\lambda_{30}^{(3\omega)} = 1.542 \mu\text{m}$ ,  $L = 350 \mu\text{m}$ ): upper,  $R_{VV;v}^{(3\omega)}(\vartheta, L)$ ; middle,  $R_{HV;v}^{(3\omega)}(\vartheta, L)$ ; lower,  $R_{VV;h}^{(3\omega)}(\vartheta, L)$ .

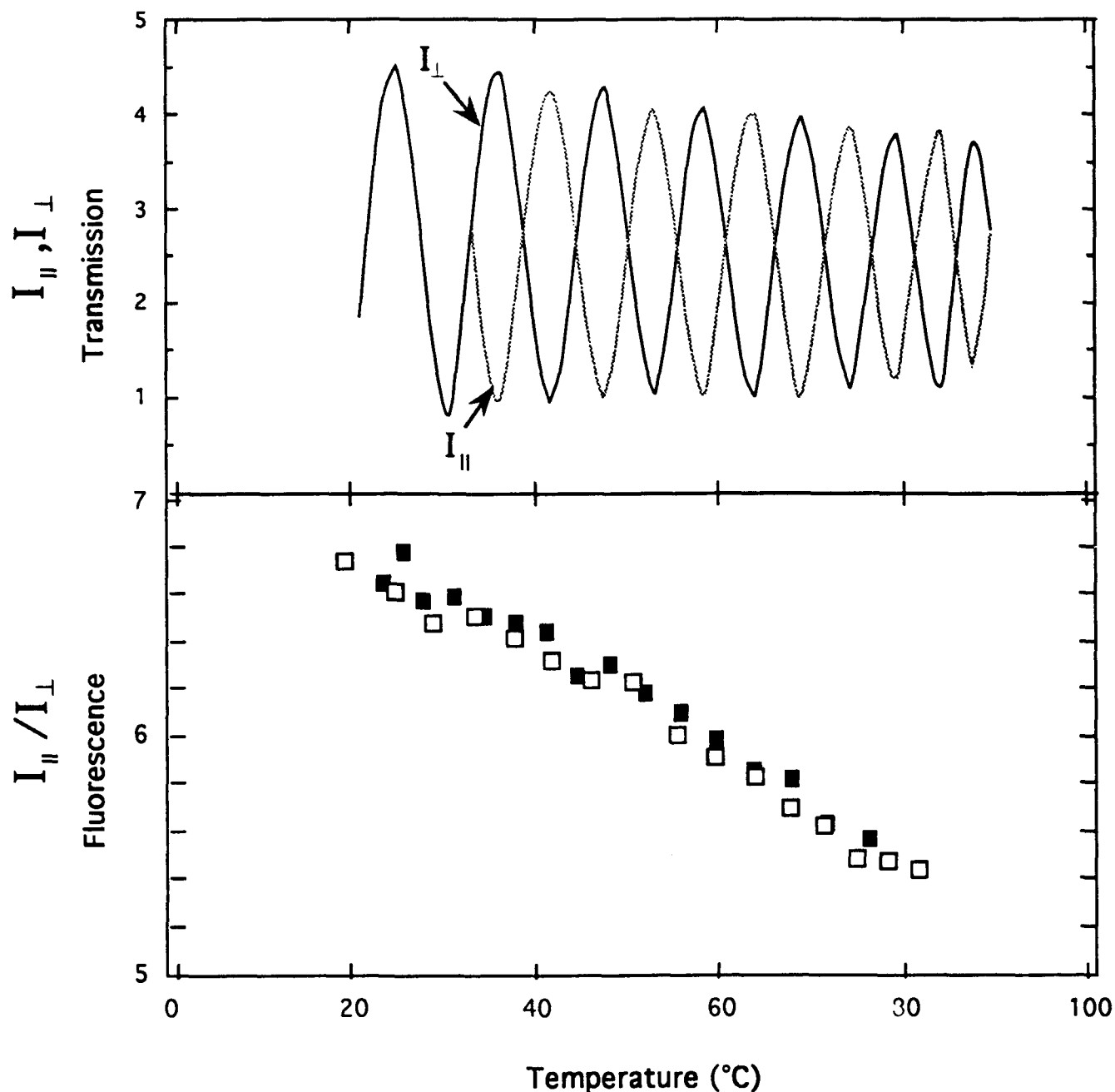


Figure 13 Optical effects observed on changing the temperature of a monodomain nematic solution of a rodlike polymer (PBZT in methane sulfonic acid;  $\phi = 0.049$ ,  $L_w = 140$  nm).  
 Upper: The transmission between crossed and parallel polars ( $\lambda = 632.8$  nm).  
 Lower: The ratio of the fluorescence emission intensities  $I_{\parallel}$  and  $I_{\perp}$ , for light polarized parallel and perpendicular to the director, respectively (Incident light absorbed within  $\approx 1 \mu\text{m}$ ). The open and filled circles give data for increasing and decreasing temperature, respectively.

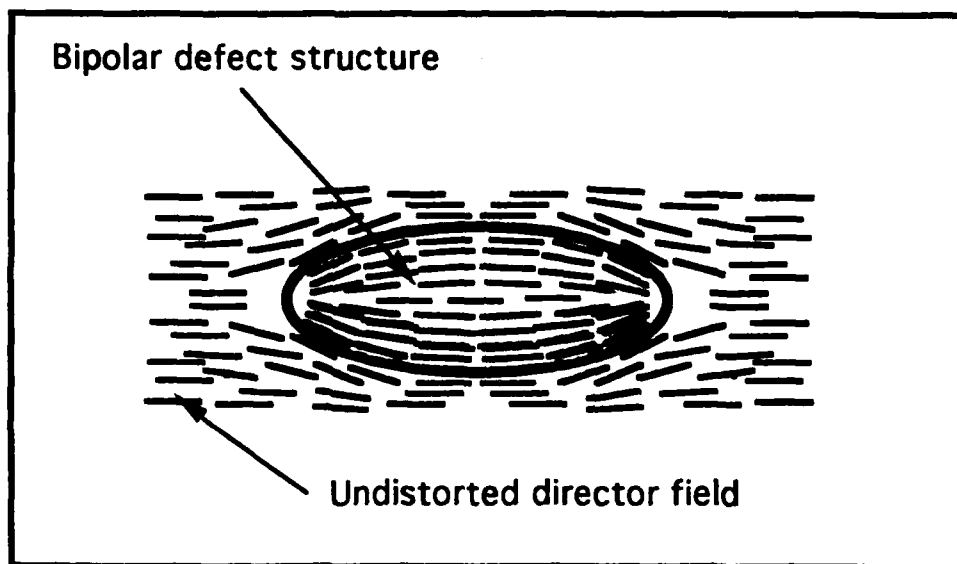


Figure 14 Schematic diagram of a bipolar defect structure observed during heating a nematic solution of PBZT below the clearing temperature.

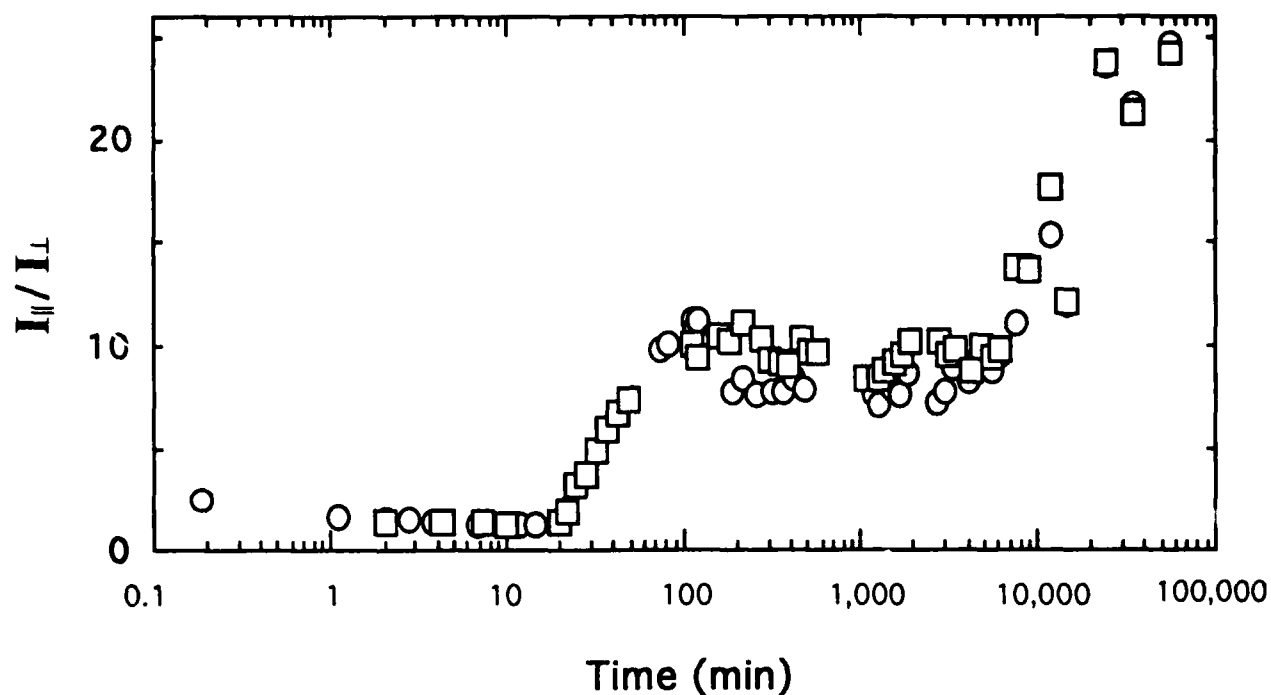
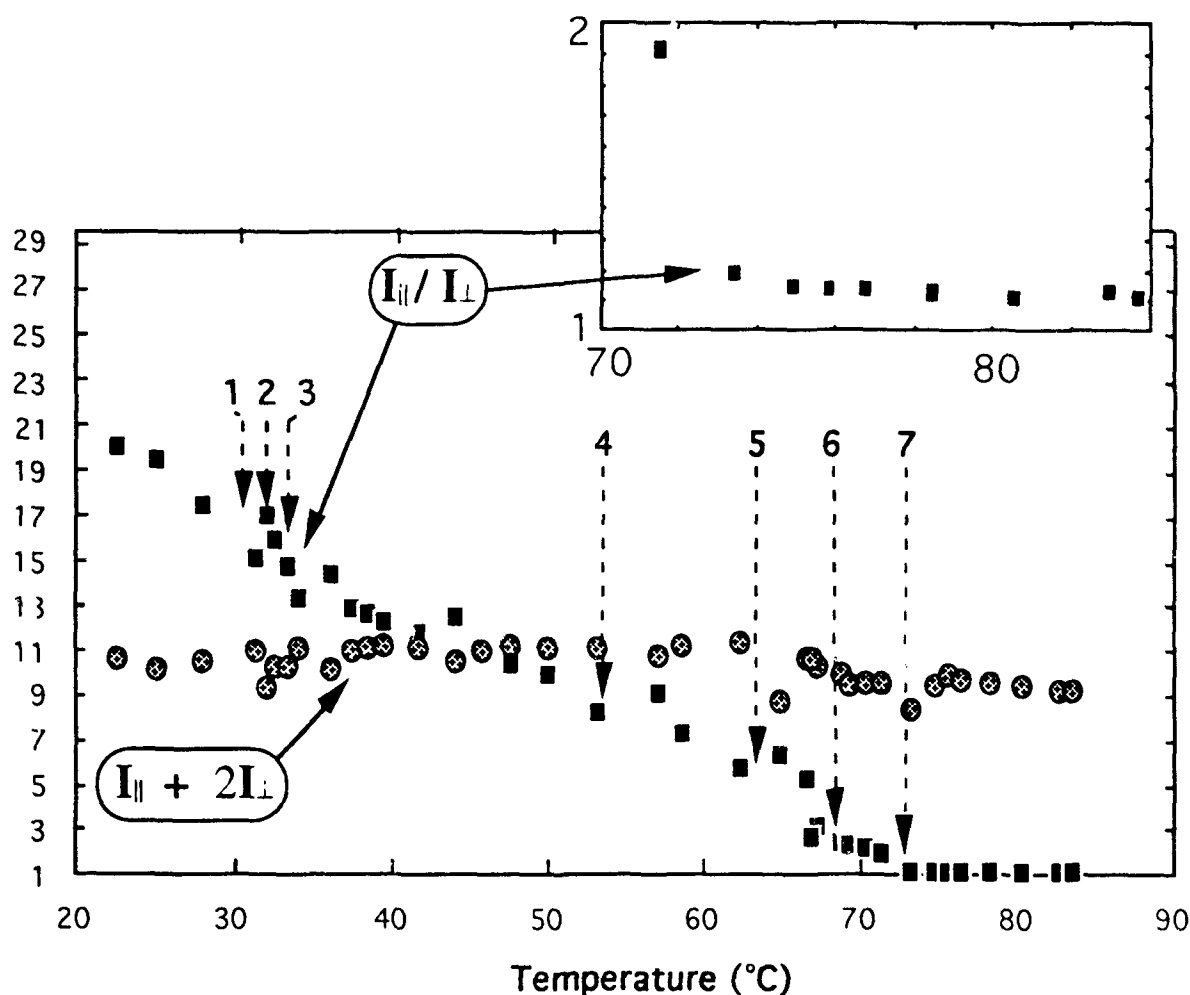
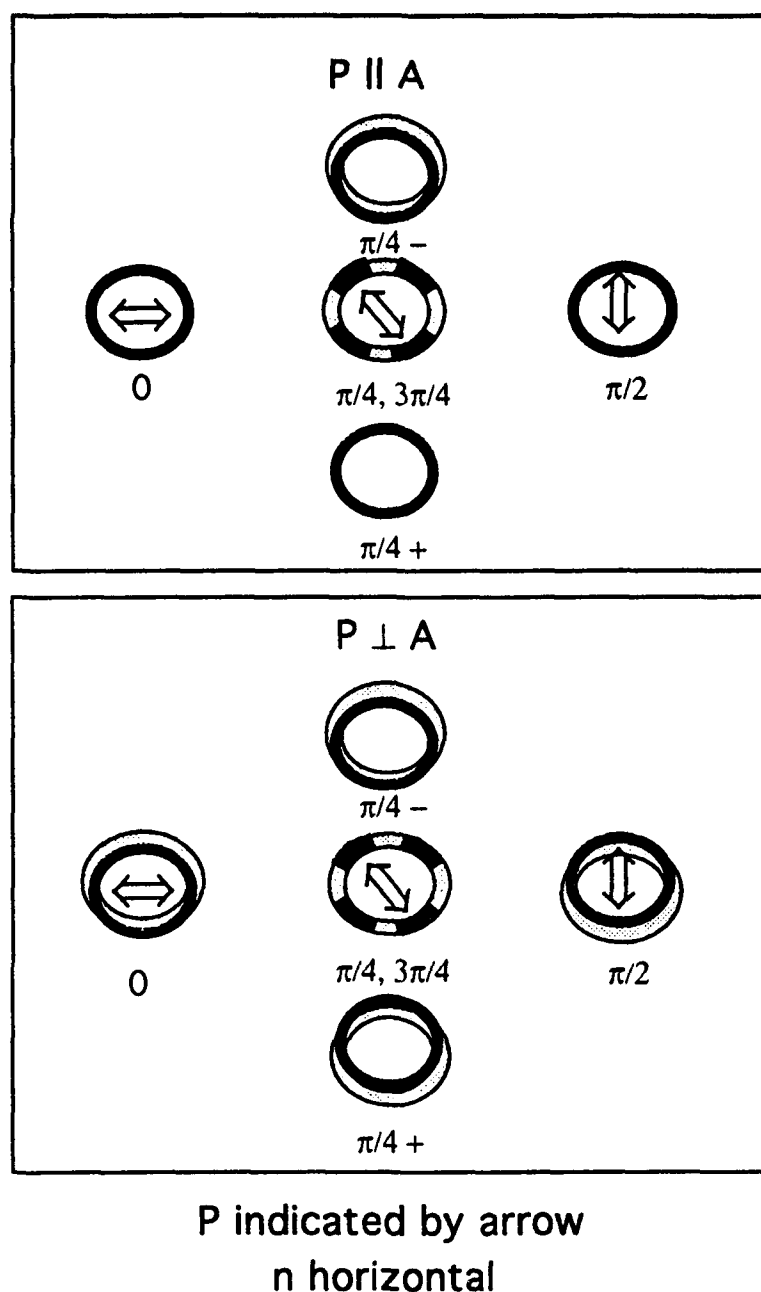


Figure 15 Fluorescence emission anisotropy during annealing of a sample to form a monodomain after extrusion into a tube with a rectangular channel ( $400\mu\text{m} \times 8\text{mm}$ );  $\phi = 0.043$ ,  $L_w = 120\text{ nm}$ . The ratio of the fluorescence emission intensities  $I_{\parallel}$  and  $I_{\perp}$  for light polarized parallel and perpendicular to the director, respectively (Incident light absorbed within  $\approx 1\mu\text{m}$ ). The squares and circles give data for filling rates of  $0.032$  and  $2.4\text{ mm}^3/\text{s}$ , respectively.



- 1 Point Defects appear in Crossed Polar Illumination
- 2 Conoscopic Images Disappear; Defects Multiply in Number and Begin to Overlap
- 3 Small "Circular Images Appear"; Birefringence Beginning to Lose Orientation
- 4 Large "Rim-Like" Images Form and Merge
- 5 Bright Between Crossed Polars
- 6 Biphasic
- 7 Fully Isotropic in the Bulk

Figure 16 Optical effects observed on changing the temperature of a monodomain nematic solution of a rodlike polymer (PBZT in methanesulfonic acid;  $\phi = 0.033$ ,  $L_w = 155$  nm).  
 Squares: The temperature dependence of the ratio  $I_{\parallel}/I_{\perp}$  of the fluorescence emission intensities  $I_{\parallel}$  and  $I_{\perp}$  for light polarized parallel and perpendicular to the director, respectively (Incident light absorbed within  $\approx 1$   $\mu\text{m}$ ).  
 Circles: The temperature dependence of the invariant of the fluorescence emission intensities.



**Figure 17** Schematic diagrams of the appearance of twist-loop defects in orthoscopic microscopy. The nematic director is horizontal in all cases, and the orientation of the polarizer  $P$  for the incident light is indicated by the arrows and/or the angles; the orientation of the analyzer  $A$  of the transmitted light is parallel or perpendicular to  $P$  in the upper and lower panels, respectively. The black and shaded loops appear dark and bright, respectively, with the image for  $P$  at  $\pi/4$  to the director being a loop alternating between dark and bright regions.

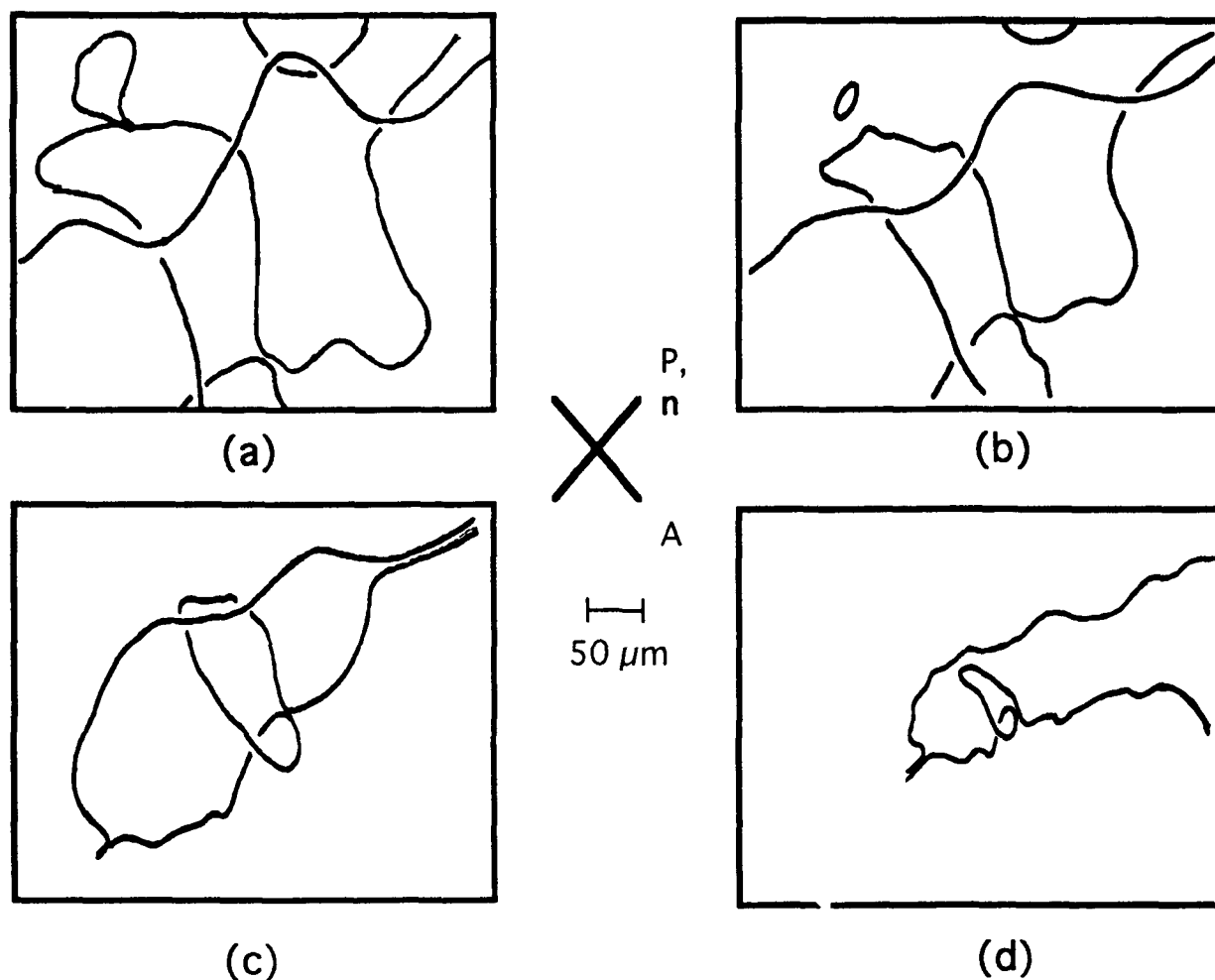


Figure 18 Example of the relaxation of a complex loop defect(s). Schematic representations of photomicrographs prepared between crossed polarizer and analyzer on the left, and schematic diagrams of the loop(s) on the right; cell thickness 300  $\mu\text{m}$ ,  $\phi = 0.063$ ,  $L_w = 135$  nm.

- a. The upper portion of a small loop, and a portion of a large loop that crosses over itself four times in the field of view (the loop continues at the upper left and lower right); a third loop appears to be in contact with the large loop (47.5 hr after filling).
- b. A remnant of the small loop, a small loop that has separated from the large loop, and the evolution of the large loop (71.5 hr after filling).
- c. Continued evolution of the large loop, with the two smaller loops having vanished (122.5 hr after filling).
- d. Continued evolution of the large loop (243.5 hr after filling).



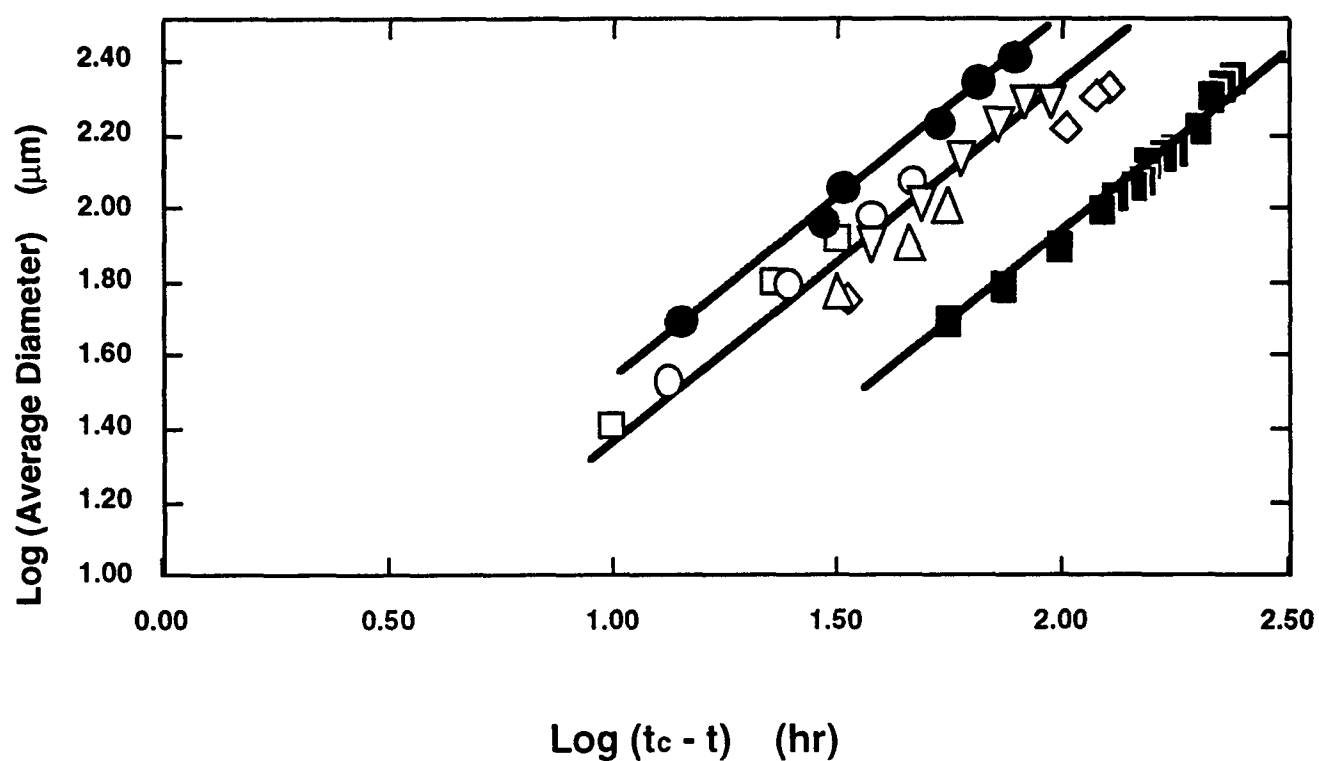


Figure 19 The average diameter of loops during collapse as a function of the time  $t_0 - t$  measured from the time  $t_0$  that the loop disappears. The data are for three samples:  $\phi = 0.050$ ,  $L_w = 155$  nm, open symbols (different loops designated by different symbols);  $\phi = 0.058$ ,  $L_w = 155$  nm, filled circles;  $\phi = 0.063$ ,  $L_w = 135$  nm, filled squares. The lines have unit slope.

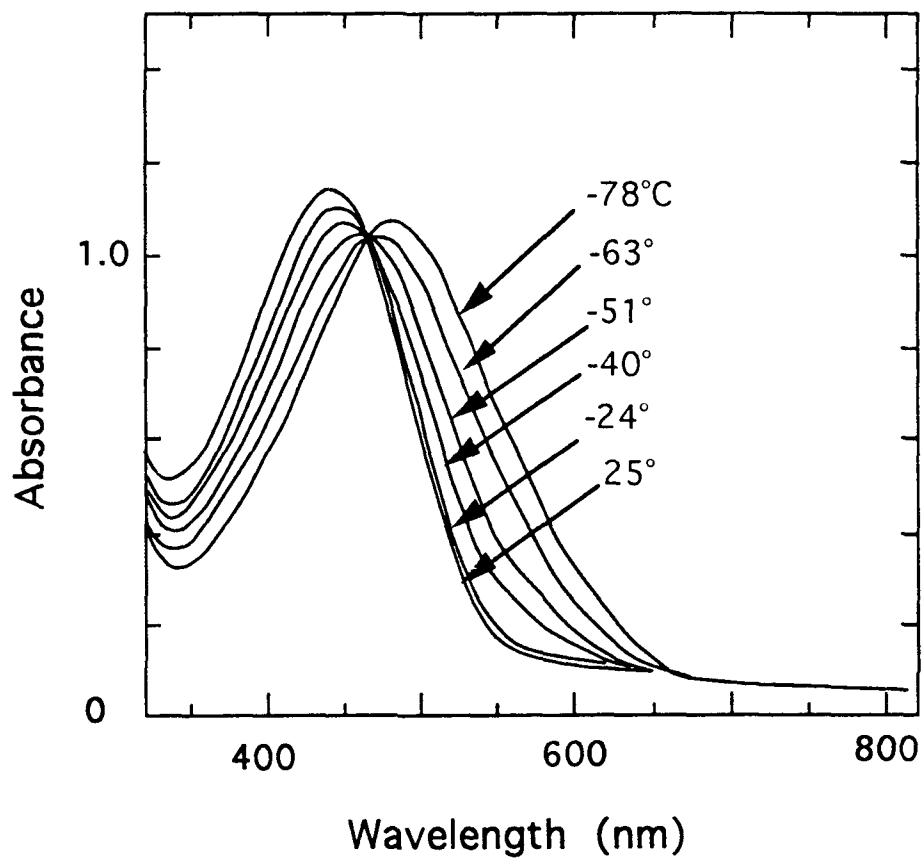


Figure 20 The effect of temperature on the absorbance of a dilute solution of poly(*n*-dodecylthiophene) in chloroform;  $c = 3.0$  g/L. The temperature is indicated on the figure; the cell was 0.2 cm thick.

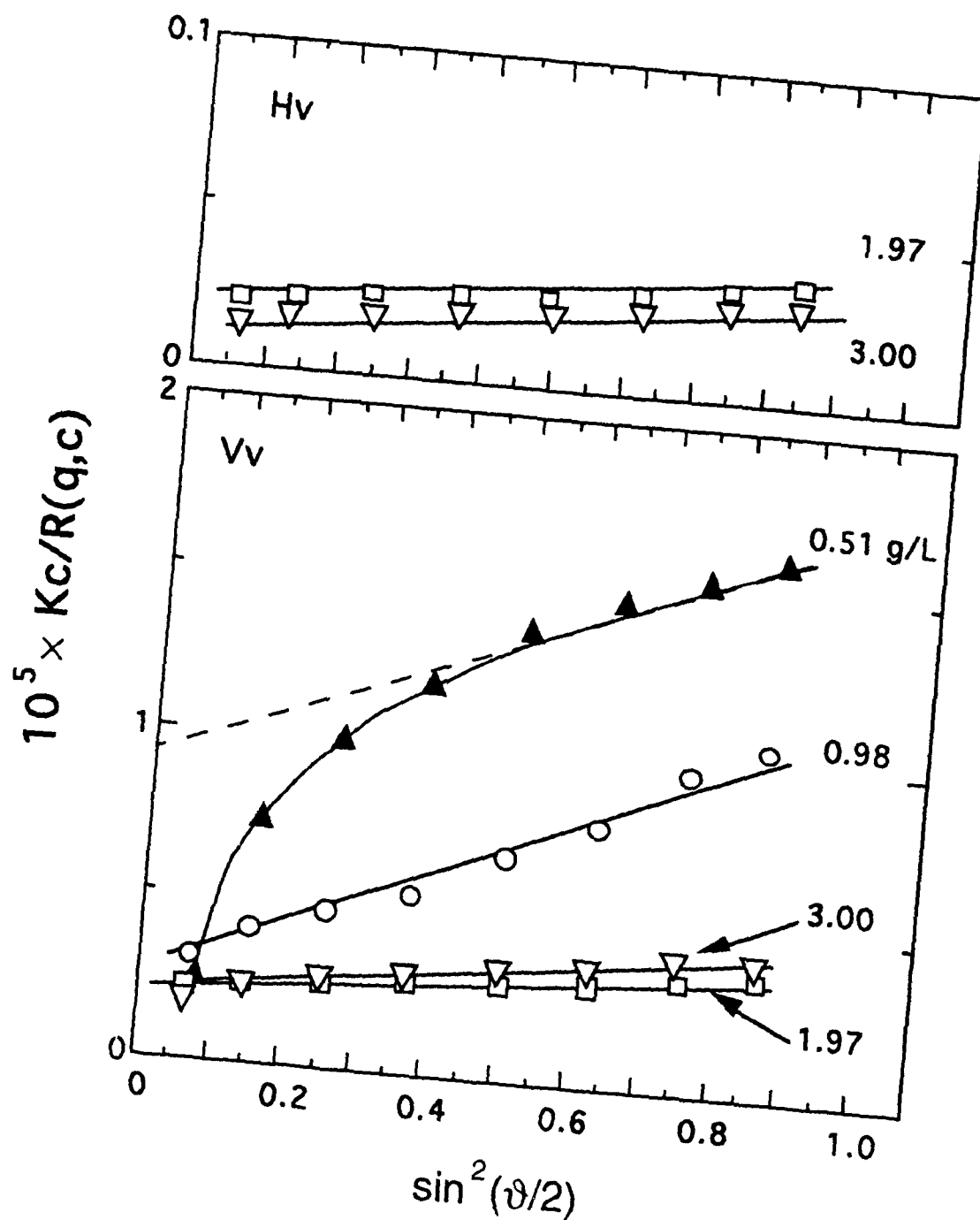


Figure 21 Static light scattering on dilute solutions of poly(*n*-dodecylthiophene) in chloroform; upper and lower panels are for the depolarized (Hv) and polarized scattering (Vv), respectively. The concentrations are indicated (g/L); the unfilled and filled symbols are for histories A and B, respectively.

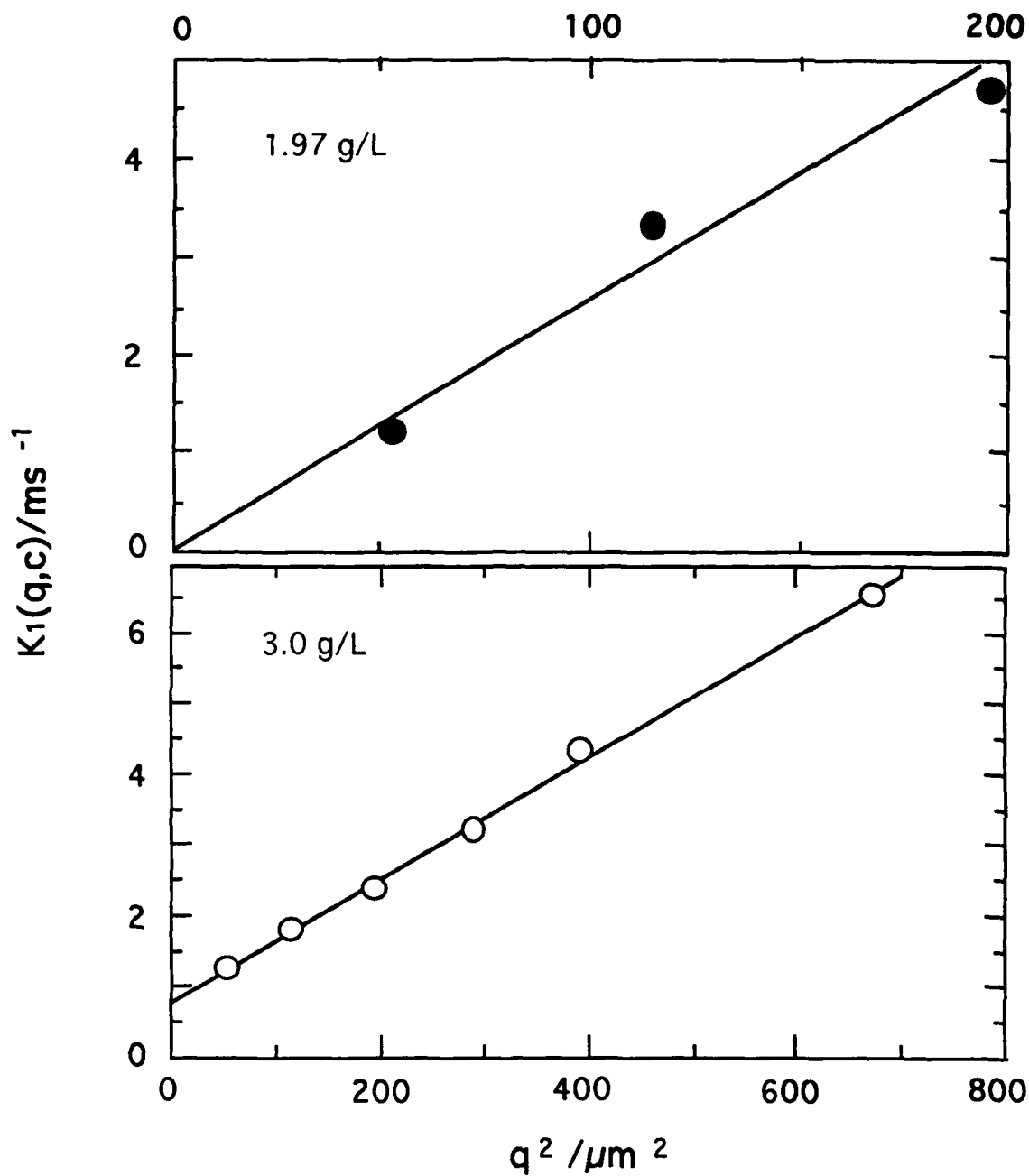


Figure 22 The first cumulant from dynamic light scattering on dilute solutions of poly(*n*-dodecylthiophene) in chloroform.  
 Upper: Polarized (Vv) scattering for a solution with  $c = 1.97 \text{ g/L}$ , history E;  
 Lower: Deolarized (Hv) scattering for a solution with  $c = 3.0 \text{ g/L}$ , history A.

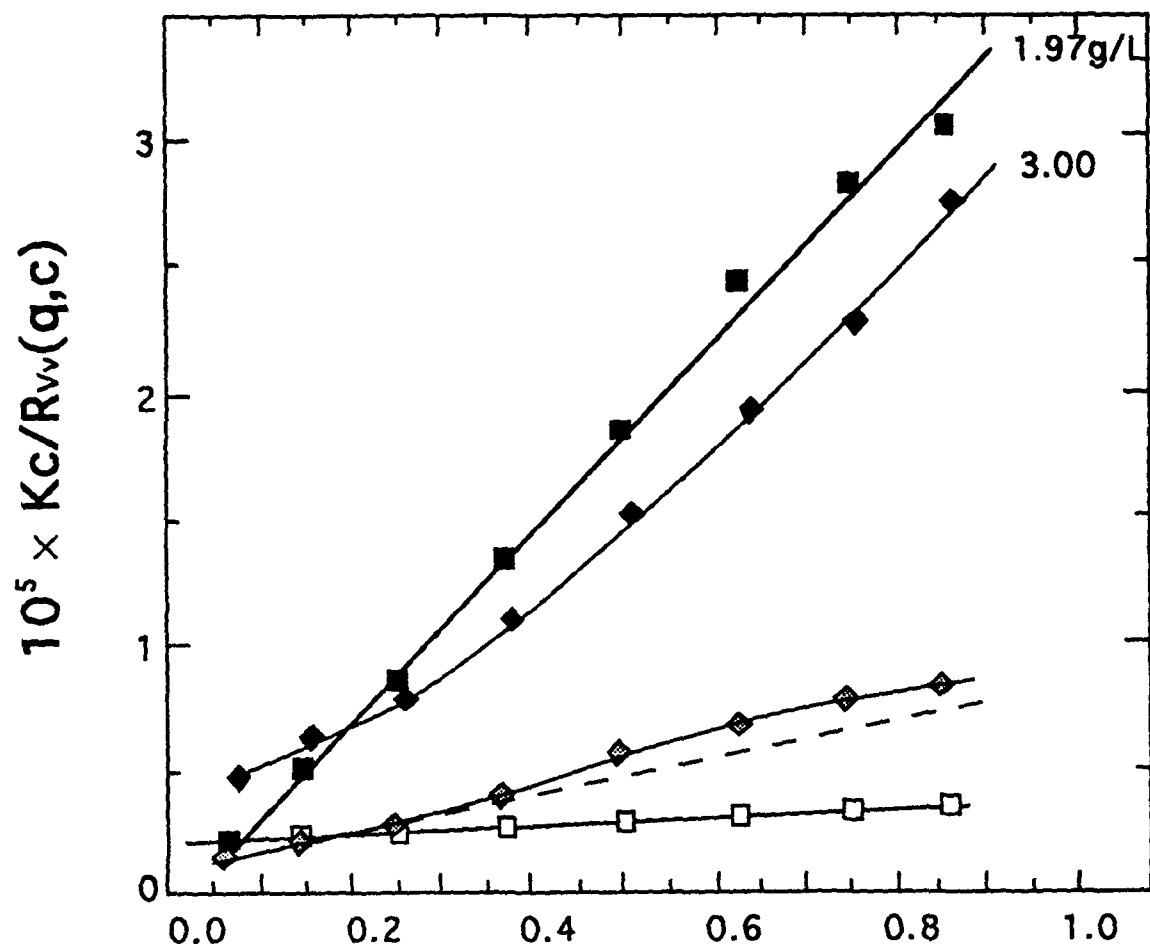


Figure 23 Static polarized (Vv) light scattering on dilute solutions of poly(*n*-dodecylthiophene) in chloroform. The concentrations are indicated (g/L); the unfilled and filled symbols are for histories A and C, respectively, and the shaded symbols are for history E.

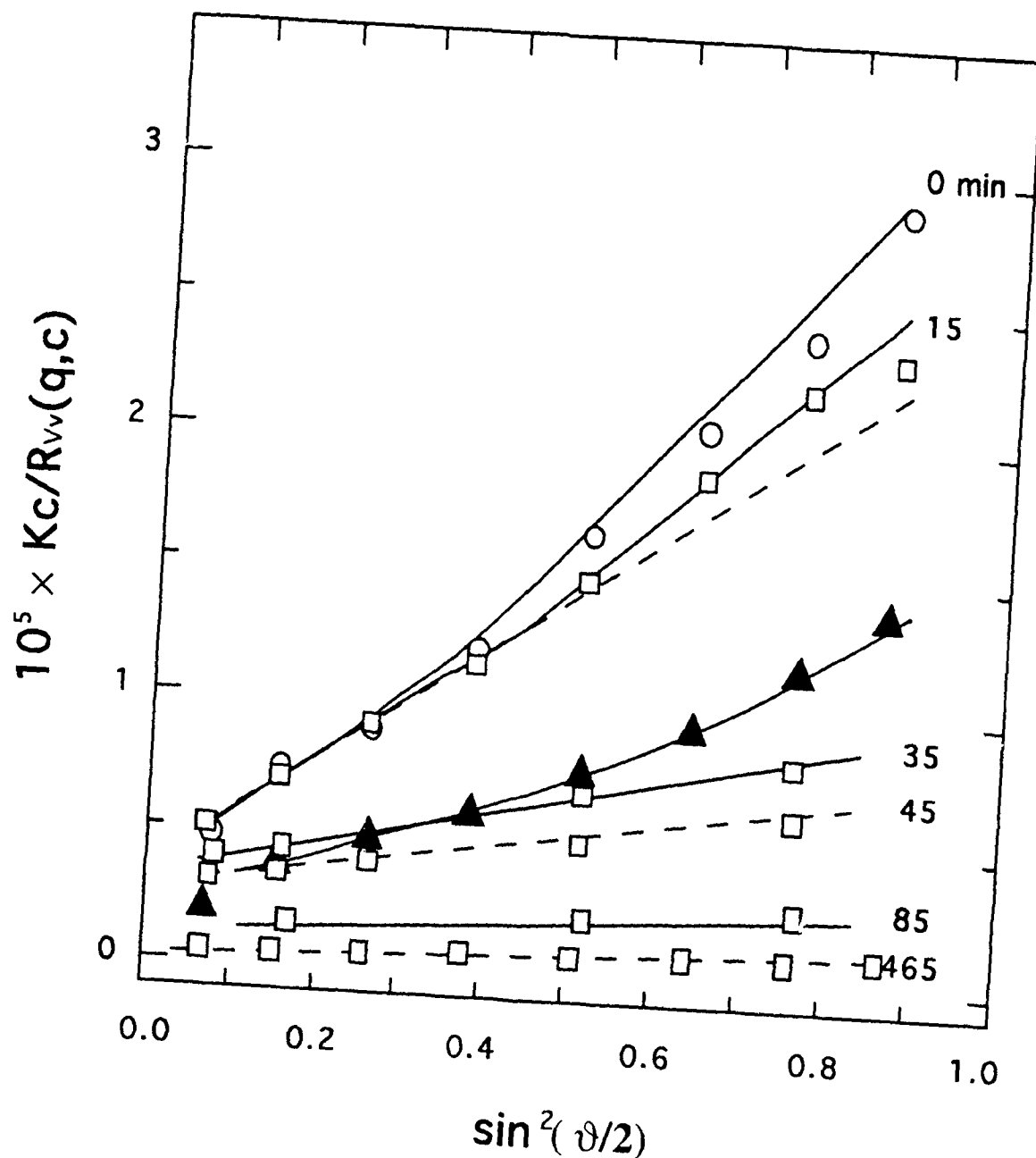


Figure 24 Static polarized (Vv) light scattering on dilute solutions of poly(*n*-dodecylthiophene) in chloroform;  $c = 3.0$  g/L. The concentrations are indicated (g/L); the unfilled circles and squares are for histories C and D, respectively, with the times at  $T_{q2} = -16.5^\circ\text{C}$  indicated (min), and the shaded symbols are for history F.

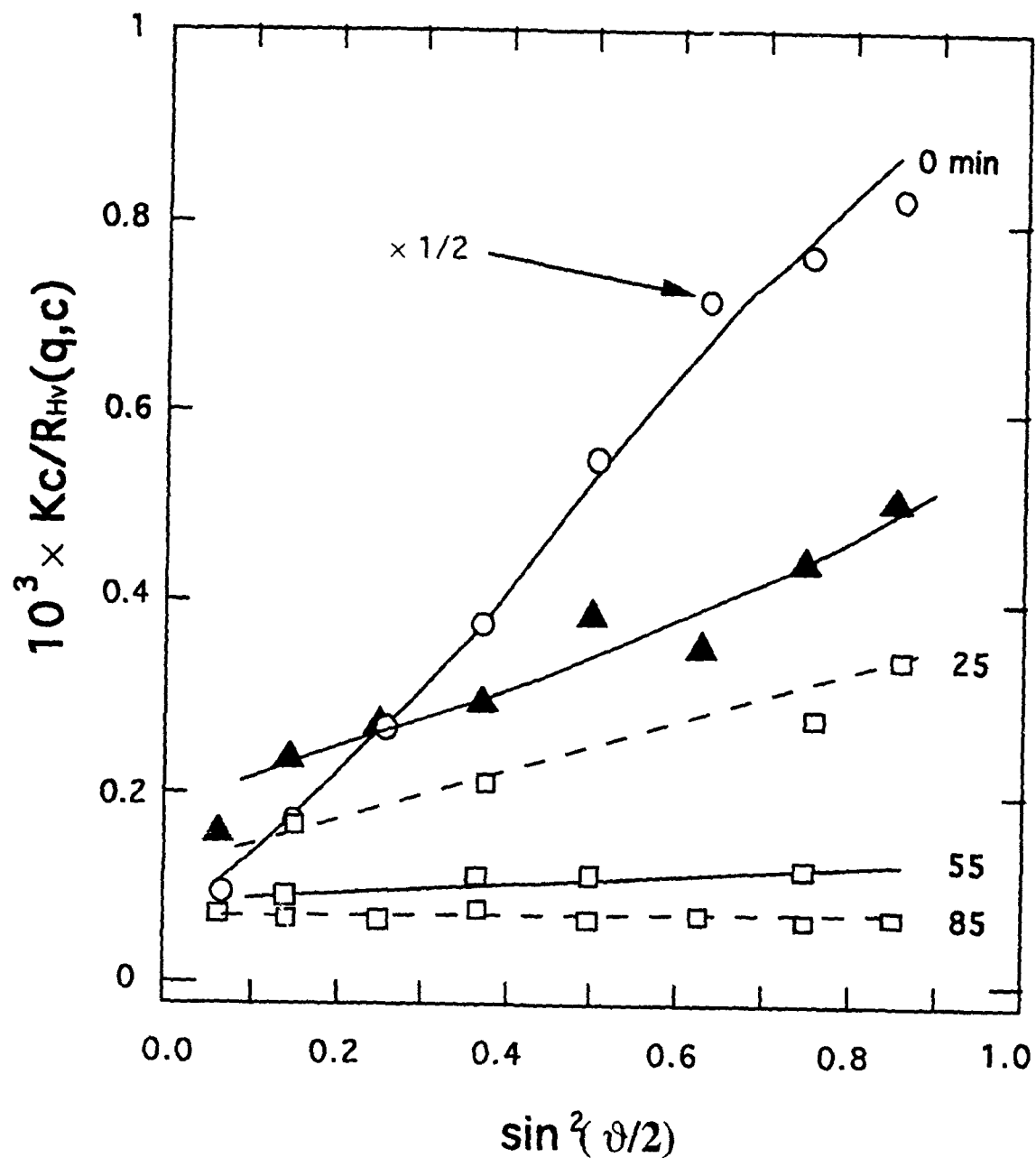


Figure 25 Static depolarized (Hv) light scattering on dilute solutions of poly(*n*-dodecylthiophene) in chloroform;  $c = 3.0$  g/L. The concentrations are indicated (g/L); the unfilled circles and squares are for histories C and D, respectively, with the times at  $T_{q2} = -16.5^\circ\text{C}$  indicated (min), and the shaded symbols are for history F.

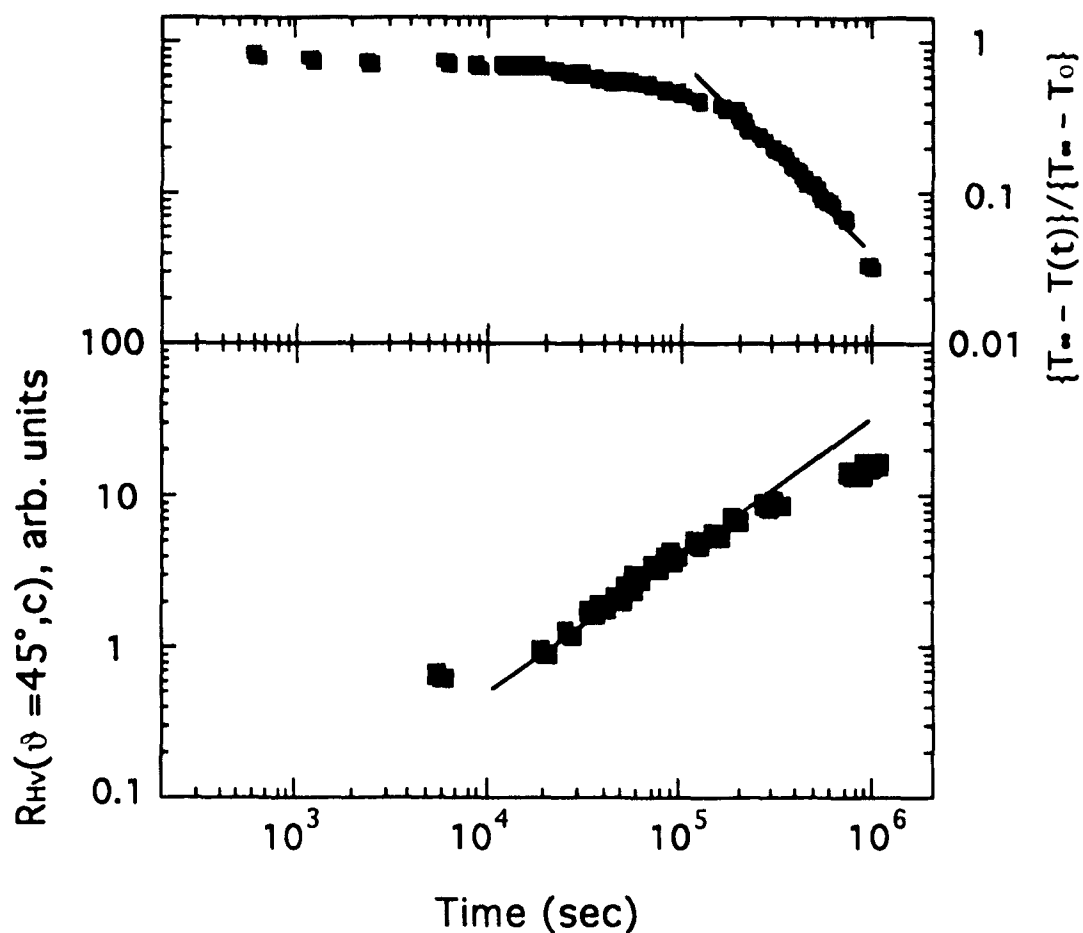


Figure 26 Bilogarithmic plots of the change of two parameters with time for a dilute solution of poly(*n*-dodecylthiophene) in chloroform for history D, with  $T_{q2} = -16.5^\circ\text{C}$ ;  $c = 3.0$  g/L.  
 Upper: A function of the transmission  $T(t)$  ( $\lambda = 647.5$  nm);  
 Lower: The depolarized scattering at  $45^\circ$  scattering angle.



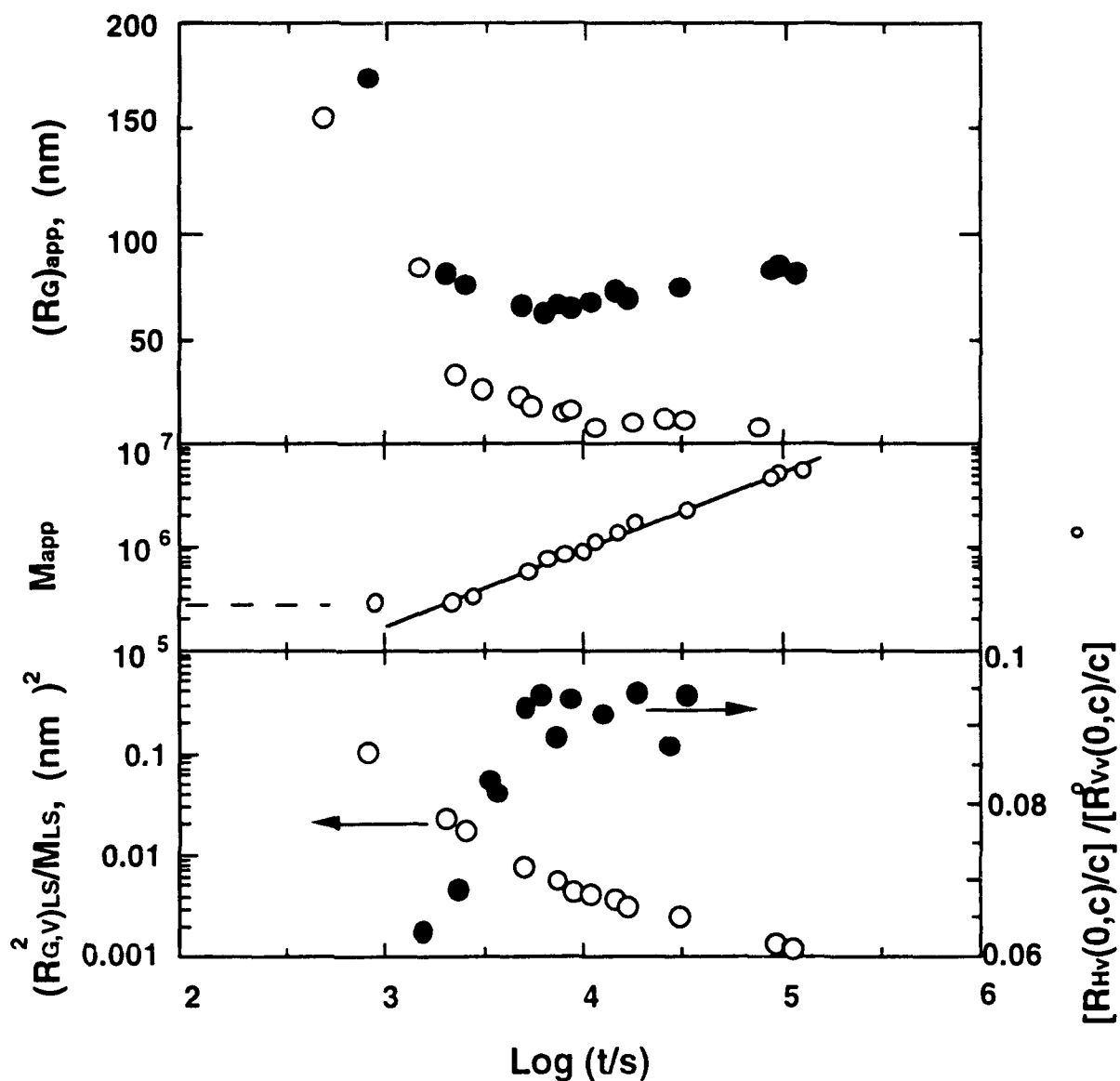


Figure 27 Bilogarithmic plots of the change of several parameters with time for a dilute solution of poly(*n*-dodecylthiophene) in chloroform for history D, with  $T_{q2} = -16.5^\circ\text{C}$ ;  $c = 3.0 \text{ g/L}$ .  
 Upper: The apparent radius of gyration, the filled and unfilled symbols are for the polarized (Vv) and depolarized (Hv) scattering, respectively;  
 Middle: The apparent molecular weight from the polarized (Vv) scattering;  
 Lower: The ratios  $(R_{G,v})_{LS}/(M_v)_{LS} \approx R_{G,LS}^2/M_w$  from the polarized (Vv) scattering (unfilled), and  $[R_{Hv}(0,c)/c]^0/[R_{Vv}(0,c)/c]^0$  of the reduced intensities at zero scattering angle of the depolarized (Hv) and polarized (Vv) scattering.